CHALMERS
UNIVERSITY OF TECHNOLOGY

Operational Transfer Path Analysis of High Frequency Noise in Electric Vehicles

Air-borne and Structure-borne Contributions from Electric Front and Rear Axle Drive Units

Master's thesis in Sound and Vibration

SHIVAM BAHUGUNA

DIVISION OF APPLIED ACOUSTICS
DEPARTMENT OF ARCHITECTURE AND CIVIL ENGINEERING

CHALMERS UNIVERSITY OF TECHNOLOGY
Gothenburg, Sweden 2021
www.chalmers.se

Master's thesis 2021

Operational Transfer Path Analysis of High Frequency Noise in Electric Vehicles

Air-borne and Structure-borne Contributions from Electric Front and Rear Axle Drive Units

SHIVAM BAHUGUNA

Department of Architecture and Civil Engineering
Division of Applied Acoustics
Chalmers University of Technology
Gothenburg, Sweden 2021

Operational Transfer Path Analysis of High Frequency Noise in Electric Vehicles

Air-borne and Structure-borne Contributions from Electric Front and Rear Axle Drive Units

SHIVAM BAHUGUNA

Supervisor: Amir Haji Hosseini[1] | Per Alenius[1]
Examiner: Wolfgang Kropp[2]

Master's Thesis 2021
Department of Architecture and Civil Engineering
Division of Applied Acoustics
Chalmers University of Technology
SE-412 96 Gothenburg
Telephone +46 31 772 1000

Typeset in LaTeX
Printed by Chalmers Reproservice
Gothenburg, Sweden 2021

[1]Personal Driving Experience Centre, Volvo Car Corporation
[2]Division of Applied Acoustics, Chalmers University of Technology

Operational Transfer Path Analysis of High Frequency Noise in Electric Vehicles
Air-borne and Structure-borne Contributions from Electric Front and Rear Axle Drive Units

SHIVAM BAHUGUNA
Division of Applied Acoustics
Department of Civil and Environmental Engineering
Chalmers University of Technology

Abstract

Transfer Path Analysis (TPA) has been a major NVH refinement framework utilized in the automotive industry for years. Traditionally, classical TPA has been used to conduct Source-Path-Receiver based investigations. However, its time-consuming nature and the inability to maintain complete vehicle boundary conditions limit its application to vehicle development stages. Over the recent years, shorter vehicle development cycles have led to the evolution of more practical TPA techniques. Operational TPA (OTPA) is one such efficient and time-saving method, which even ensures the maintenance of boundary conditions over the complete vehicle. However, OTPA results are extremely sensitive to instrumentation and hence, it demands greater care for the inclusion of all coherent transmission paths within the vehicle. OTPA has been proven to be an efficient troubleshooting tool over the conventional Internal Combustion Engine (ICE) vehicles. However, there still remains a vast scope for its implementation in modern electric vehicles due to the high frequency nature of their propulsion noise.

This Master Thesis deploys OTPA to study high frequency noise and vibration propagation from the electric propulsion units inside a prototype Battery Electric Vehicle (BEV). Upon a detailed inspection of the potential air-borne leakages and structure-borne transfer paths from the electric motor bays into the vehicle, measurements were conducted on a chassis dynamometer inside a semi-anechoic chamber. Next, individual path transmissibilities to the response, i.e., the Driver Ear Level (DEL), were estimated upon Cross-talk Cancellation (CTC) using Singular Value Decomposition (SVD) and Principle Component Analysis (PCA), and a detailed Path-Receiver based vehicle model was formulated. Moreover, the critical paths responsible for high frequency noise propagation inside the vehicle were detected. To conclude, validation studies were conducted in order to verify the estimated path contributions. The investigation also revealed some challenges in frequency distinction between the air-borne and structure-borne contributions.

Keywords:

Operational Transfer Path Analysis, Path Contribution, Cross-talk Cancellation, Singular Value Decomposition, Principle Component Analysis, Order Analysis, Air-borne, Structure-borne, Battery Electric Vehicle

Acknowledgements

This Master Thesis was completed at Volvo Car Corporation (VCC), Sweden, under a joint supervision from the Division of Applied Acoustics at Chalmers University of Technology, Sweden. The licences for all the data acquisition systems and post-processing softwares were provided by Müller-BBM VibroAkustik Systeme GmbH.

First and foremost, I would like to sincerely express my gratitude towards my examiner at Chalmers, Professor Wolfgang Kropp, whose constant guidance and encouragement highly motivated the research within the project. Special thanks to Magnus Knutsson and William Easterling from Volvo Cars for providing me the wonderful opportunity to join as a thesis worker at VCC. I would also like to thank my advisor at Volvo Cars, Per Alenius, for his invaluable suggestions and technical recommendations with regards to the project. Also, a big thanks to Martin Lohrmann at Müller-BBM VibroAkustik Systeme for not only taking the time for technical discussions but also for sharing his deep insights within the topic of OTPA.

My heartfelt thanks to my thesis supervisor, Amir Haji Hosseini at Volvo Cars, for always believing in me and for being a personal support throughout the course of this thesis work. His technical experience and expertise within the field of NVH not only aided the completion of the project but also made this thesis journey a rewarding experience. I would also like to thank all my classmates at Chalmers for making the masters degree course at Chalmers an exceptionally adventurous journey.

Most importantly, I thank my parents, my grandfather and my little sister for their unparalleled love, care and support.

Shivam Bahuguna
Shivam Bahuguna

Gothenburg, September 2021

Acronyms

NVH	Noise Vibration & Harshness
TPA	Transfer Path Analysis
SB	Structure-borne
AB	Air-borne
OTPA	Operational Transfer Path Analysis
SVD	Singular Value Decomposition
PCA	Principle Component Analysis
RMA	Response Modification Analysis
CTC	Cross-Talk Cancellation
MIMO	Multiple Input Multiple Output
CAD	Computer Aided Design
CAE	Computer Aided Engineering
DOF	Degree of Freedom
SNR	Signal-to-Noise Ratio
SPL	Sound Pressure Level
AWD	All Wheel Drive
FWD	Front Wheel Drive
RWD	Rear Wheel Drive
REGEN	Regenerative Braking
VCC	Volvo Car Corporation
EV	Electric Vehicle
BEV	Battery Electric Vehicle
PHEV	Plug-in Hybrid Electric Vehicle
EFAD	Electric Front Axle Drive
ERAD	Electric Rear Axle Drive
EPS	Electronic Power Steering
HVAC	Heating, Ventilation & Air Conditioning
BIW	Body In White
e-NVH	Electric Noise Vibration and Harshness
PMSM	Permanent Magnet Synchronous Motor
IHFA	Inverter High-voltage Front Axle
IEM	Inverter Electric rear axle drive Module
ELPOT	Electric Partial Open Throttle
ELWOT	Electric Wide Open Throttle
DC	Direct Current
AC	Alternating Current
SOC	State of Charge
OBD	On-Board Detection
ECU	Electronic Control Unit
EDU	Electric Drive Unit
FDU	Front Drive Unit
RDU	Rear Drive Unit

CAN	Controller Area Network
INCA	Integrated Calibration & Application Tool
DAQ	Data Acquisition
LAN	Local Area Network
HV	High Voltage
DEL	Driver Ear Level
PEL	Passenger Ear Level
ABS	Anti-lock Braking System
LH	Left-Hand Side
RH	Right-Hand Side
PBN	Pass-By Noise
ATF	Acoustic Transfer Function
VVS	Volume Velocity Source
NTF	Noise Transfer Function
CPS	Cross-Power Spectrum
PR	Prominence Ratio
TNR	Tone-to-Noise Ratio
ISVR	Institute of Sound and Vibration Research
CCP	Constant Current Power
ICP	Integrated Circuit Piezo-electric
IEPE	Integrated Electronic Piezo-Electric

Contents

List of Figures

List of Tables

1 Introduction

Root cause identification for most of the Noise, Vibration and Harshness (NVH) challenges can be performed using Transfer Path Analysis (TPA). Generally, TPA revolves around a Source-Path-Receiver based investigation and has been used in the automotive industry for not only classifying NVH issues to be either source-dominant or transfer path-dominant, but also to provide a clue about the vehicle being more sensitive to excitations from a particular source. TPA finds its applications not only during the early vehicle development phases but also during the post-production phase. The presented Master Thesis work illuminates upon the utilization of one of the TPA methods, namely, the Operational Transfer Path Analysis (OTPA) for studying high frequency noise propagation inside Battery Electric Vehicles (BEVs). Compared to other TPA techniques, OTPA proves to be a time-saving troubleshooting tool, which is one of the main reasons for its deployment within the presented work. A Path-Receiver based OTPA investigation has been conducted over a BEV prototype in order to highlight the critical air-borne leakages and structure-borne transfer paths associated with its propulsion system. The work presented in the report not only renders key insights with regards to NVH-related future developments over the particular test vehicle, but also enables an understanding of OTPA's advantages and disadvantages when analyzing high frequency concerns in Electric Vehicles (EVs).

1.1 Background

TPA has been used in the automotive research and development as one of the main refinement frameworks to troubleshoot challenging NVH issues. Classical TPA has been a traditional method for Source-Path-Receiver based investigations. However, its complex and time-consuming nature has motivated engineers to come up with alternative TPA approaches, such as in-situ TPA, OTPA, etc. Similar to Classical TPA, in-situ TPA provides a detailed Source-Path-Receiver model for the vehicle, while maintaining the boundary conditions between the source and the transfer path intact. However, in-situ TPA is still associated with additional complexity and time-consumption, due to the particularly large instrumentation involved and the challenges associated with acquiring Frequency Response Functions (FRFs) for complex architectures. An alternative approach is to utilize OTPA to estimate vehicular transmissibility functions using operational excitations alone, with the benefit of maintaining the boundary conditions of the complete vehicle unchanged. One major drawback with OTPA is the high sensitivity of results to the inputs, which implicates that the contributions from any neglected coherent path within the model shall lead to a mathematical compensation within the algorithm. Hence, additional care has to be taken to consider all coherent propagation paths within the OTPA model for correct estimation of individual path contributions. Diez-Ibarbia et al. presented a comparison between classical TPA and OTPA over EVs to highlight critical structure-borne path contributions from the engine and the suspension system. Results from both the methodologies were compared and it was concluded that both the methods revealed similar path ranking. However, while OTPA revealed quick qualitative insights about the source-path characteristics, classical TPA was observed to be a more quantitative method, albeit time-consuming and laborious [1].

Furthermore, NVH issues are historically categorized as structure-borne at lower frequencies and air-borne at higher frequencies [2]. Over the years, this distinction in frequency domain has been proven for conventional Internal Combustion Engine (ICE) vehicles. Nonetheless, this is not fully understood for EVs due to their wider frequency range of operation. In addition to the main transfer paths, high frequency noise can also travel through parasitic paths, such as ground cables, High Voltage (HV) cables, etc. Skilled NVH engineers often have good knowledge about the most critical paths. However, parasitic paths are often left unexplored.

1.2 Scope

The presented work aims at utilizing OTPA to provide better understanding of high frequency noise propagation in EVs, including propagation through parasitic paths. As the first step, literature review was conducted in order to understand the OTPA methodology and the available research over the extent of TPA applications in BEVs. This was followed by an extensive investigation of the propulsion system interface with the interior cabin using available CAD models in order to identify all the suspected paths. Further, air-borne transmissibility measurements were conducted in order to highlight sensitive leakages from the electric motor bays inside the vehicle. The work was then continued by the instrumentation of all the suspected air-borne leakages and structure-borne transfer paths within the vehicle. Experimental data was then acquired in multiple distinct vehicle load cases on a chassis dynamometer inside a semi-anechoic chamber. Post measurements, data was analyzed to set up an OTPA model for the complete vehicle and path ranking was performed for critical propulsion orders. Ultimately, verification studies were conducted in order to validate the OTPA model, and the scope as well as the limits of utilization of OTPA method in BEVs were defined.

1.3 Motivation

Global transition towards automotive electrification has brought new challenges along with itself. In contrast to the silent character associated with an EV sound perception, absence of low frequency background noise leads to a decrement in the masking noise levels and hence, an increment in the high frequency noise prominence inside the vehicle. This results in enhanced annoyance levels for the driver and passengers in EVs. Significant research has been conducted over conventional ICE vehicles with regards to the effect of combustion, intake or exhaust phenomena over vehicle's NVH attributes. However, relatively newer architectures developed to accommodate electric components within a BEV need to be further studied in depth in order to develop better insights on various possible air-borne leakages and structure-borne transfer paths from the electric motor bays inside an EV. Freeman et al. presented the design challenges in implementing a complete conversion of a conventional ICE vehicle fleet into a pure EV with the NVH aspects into prime focus [3]. Further, noise at higher frequency is inherently known to be directive, and high frequency vibration is often associated with increased mobility along the parasitic paths. Hence, a necessity for better characterization of electric noise propagation inside BEVs, especially at higher frequencies, has aroused.

The challenges associated with the e-NVH characterization of a BEV proved to be the major motivation towards the initiation of the presented Master Thesis. The practical and time-saving nature of OTPA as a methodology was convincing enough for it to be selected as the trouble-shooting tool within the project. Furthermore, while OTPA as a methodology has been studied well over the conventional ICE vehicles, there is a huge scope for its implementation in BEVs where its merits and de-merits as a trouble-shooting tool are still to be confirmed. Hence, the presented Master Thesis stands out in terms of its utilization and verification of OTPA over a BEV not only for the electric noise path localization, but also for the air-borne and structure-borne classification of noise propagation inside BEVs.

1.4 Project Deliverables

The prime objective of the presented Master Thesis was formulation and validation of an OTPA-based methodology for studying e-machine and transmission noise in EVs. Upon finalization of vehicle's OTPA model, localization of critical air-borne leakages and structure-borne transmission paths within the test vehicle was intended, with the focus on propulsion noise. An attempt to generate a library of critical path contributions towards the interior noise levels in the prototype vehicle was endeavoured for any future development activities. Further, an effort to validate the possibility of using OTPA to provide a distinction in frequency domain with regards to the air-borne and structure-borne contributions within EVs was made. To conclude, a validation study was performed for the verification of the OTPA methodology implemented within the thesis work.

1.5 Volvo Car Corporation

Volvo Car Corporation (VCC) is a Swedish automotive manufacturing company, renowned for its global presence in the premium car segment. Volvo was founded by Assar Gabrielsson and Gustav Larson as a subsidiary company to the Swedish ball bearing manufacturing company, AB SKF. Eventually, the company shifted its focus towards automotive manufacturing and the first mass-production factory was set up in Torslanda, Gothenburg in 1927. After being a part of AB Volvo till 1999, the company was sold to Ford Motor Company and was incorporated as a part of Ford's Premier Automotive Group (PAG), along with Jaguar, Aston Martin and Land Rover. Since 2010, VCC is owned by Zhejiang Geely Holding Group. Guided by the purpose to provide freedom to move in a personal, sustainable and safe way, VCC aims to switch to an all-electric fleet by 2030.

This Master Thesis was carried out under an academic collaboration between the Division of Applied Acoustics at Chalmers University of Technology and the Personal Driving Experience Centre at VCC. The tests within the thesis work were conducted in VCC's NVH facility at the Torslanda headquarter.

1.6 Report Structure

The report begins with a theoretical discussion about the TPA methods currently used in the automotive industry in Chapter 2. In addition to a detailed description of OTPA method and algorithm, a brief discussion over classical and in-situ TPA methods has also been presented in order to compare different TPA methodologies. Further, an explanation about a few essential concepts necessary to understand the approach and the results within the report has been provided.

The methodological steps followed within the project have been demonstrated in Chapter 3. Details about the CAD study conducted for selection of structure-borne vibration transfer paths and the acoustic transmissibility measurements performed for the finalization of air-borne noise leakages inside the vehicle have been presented in depth. Chapter 4 presents the measurement setup considered within the OTPA framework.

The preliminary NVH data for the subject test vehicle and the adopted OTPA strategy has been discussed in Chapter 5. The results acquired within the project, along with the other project deliverables have been illustrated in Chapter 6. Chapter 7 presents the validation studies conducted in order to verify the OTPA methodology implemented within the project. Finally, the conclusions drawn from the Master Thesis have been presented in Chapter 8 and a few recommendations over possible future work have been emphasized upon in Chapter 9.

2
Theory

Transfer Path Analysis (TPA) aims to develop a Source-Path-Receiver model of the system and upon accurate implementation, helps engineers to obtain pivotal insights about the system behaviour. NVH attributes can be linked to either the source, the transfer path, or both. In an automotive system, the source generally refers to a combustion engine, an electric motor, cooling fan, tires, etc., wherein either a rotary or reciprocating (imbalance) excitation force is generated. This excitation then transmits to the receiver position via different transfer paths, which usually refer to engine mounts, suspension links, vehicle body, etc. Structural dynamic attributes of the transfer paths, such as dynamic stiffness, damping, resonance frequencies and mode shapes significantly affect the propagation of source excitation along the transfer paths. Alternatively, it can be said that the source couples with the transfer paths in order to produce response at the receiver positions inside the vehicle, which can either be the vibration at the steering wheel, floor or the seat of a car, or the Sound Pressure Level (SPL) at the Driver Ear Level (DEL) inside the vehicle. TPA highlights the NVH issues to be either source-dominant or transfer path-dominant and hence, steers NVH engineers towards an efficient NVH mitigation strategy. Scheuren and Lohrmann summarized the history and advancements in the field of TPA, discussing source quantification methods as well as direct transmissibility estimations using OTPA [4].

Today, various TPA variants are being employed in the automotive industry, not only during the vehicle development stage but also after the start of production for troubleshooting and Pass-By Noise (PBN) clearances. Janssens et al. discussed various TPA techniques applicable for PBN source contribution analysis over both the conventional ICE vehicles and the modern EVs [5]. TPA has even proved its merit in non-automotive sectors, such as industrial NVH, building acoustics, ground vibration propagation, etc. This chapter aims at developing a fundamental understanding of the TPA methods used in the automotive industry, along with their benefits and limitations. Further, a detailed study about the OTPA method and its algorithm has been presented. Prior to the discussion over TPA methods, an effort to explain some essential concepts has been made.

2.1 Essential Concepts

This section introduces the NVH fundamentals essential to understand the workflow, results and conclusions as discussed within the presented thesis report.

2.1.1 High Frequency Prominence in EVs

The transition towards electrification in the automotive industry has resulted in new NVH challenges related to the EVs. Upon comparison with the conventional ICE vehicles, higher operational frequency content and the absence of adequate masking noise result in an enhanced prominence of high frequency tonal noise characteristics inside an EV. Wang et al. discussed the critical NVH issues related to electric motor-whine character in EVs [6]. Further, high frequency noise propagation is associated with its own complications, such as increased noise directivity and higher mobility across the vehicle. Figure 2.1a illustrates the typical noise characteristics inside an EV. Reduced low frequency noise levels can be observed in comparison to ICE vehicles, in addition to the dominance of tonal characteristics, which can be seen as frequency sweeps with an increase in RPM. These tones are called 'Orders' [7]. Orders can be observed to amplify upon their interaction with resonances at certain RPM ranges. Theoretical relation between frequency, RPM and order is:

$$Frequency \times 60 = Order \times RPM \tag{2.1}$$

Upon comparing the interior noise levels inside an EV with the near field noise around the e-machine and the vibrational velocity over the e-machine housing, it can be observed that the tonal character is present both in the form of vibration, as well as noise around the source. Hence, it becomes extremely important to analyze both the structure-borne and air-borne transfer paths for high frequency noise propagation inside an EV.

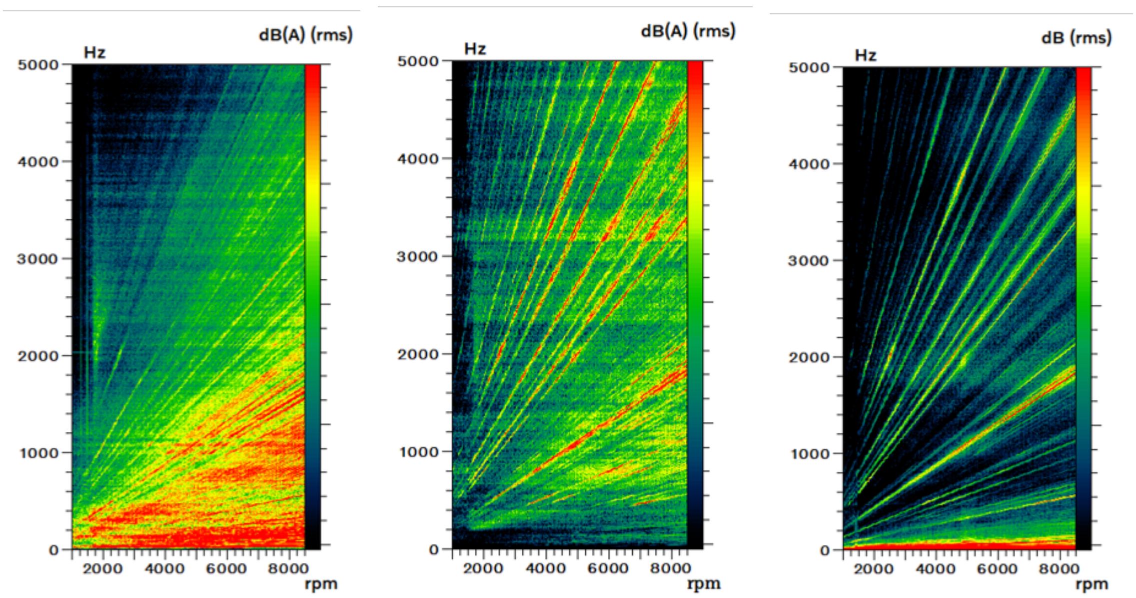

(a) Interior noise **(b)** Near-field noise **(c)** Source vibrations

Figure 2.1: A comparison of interior noise at the DEL with the near field noise and vibration on the e-machine. Plots compare the APS levels in the test vehicle for a wide open throttle load case.

2.1.2 NVH Propagation in Automotives

Noise and vibration propagation in vehicles, or in general, can either be structure-borne or air-borne. Structure-borne propagation refers to the propagation of vibration from the source systems, i.e., engines, electric motors, etc., via mounting structures into the vehicle body, as shown in Figure 2.2a. Air-borne propagation refers to the direct radiation of sound energy from the source systems inside the vehicle. This refers to an incidence of acoustic energy over the cabin panels and noise radiation inside the vehicle. Further, leakage of the radiated acoustic energy from the source systems via certain acoustic leakage paths within the vehicle can also be referred to as air-borne. Figure 2.2b illustrates the air-borne propagation from the front engine bay inside the vehicle. It is to be noted that within the scope of the presented work, the term 'air-borne transfer path' strictly refers to the acoustic leakages across the vehicle, since the main interest during the study revolved around the acoustic transfer paths and not just the radiated noise from the source. Instrumentation size was also a challenge which led to the adoption of such a strategy.

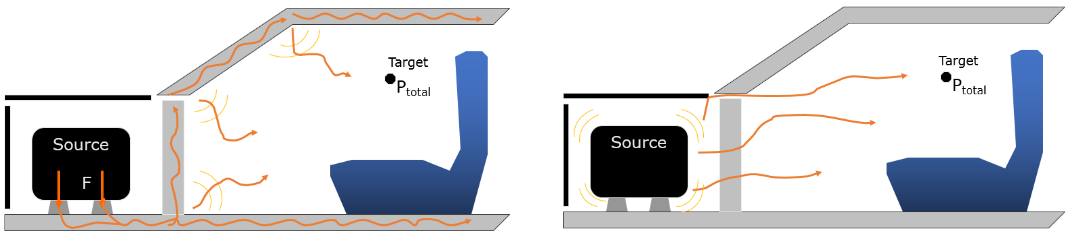

(a) Structure-borne propagation **(b)** Air-borne propagation

Figure 2.2: An illustration of noise propagation from the source system to response position inside a vehicle. [2].

2.2 Transfer Path Analysis

Transfer Path Analysis (TPA) enables a prediction of response levels at the receiver positions by defining a detailed Source-Path-Receiver model for a vehicle upon the estimation of source loads and body transfer functions. Upon multiplying the source load with the transfer path sensitivities in frequency domain (alternatively convolution in time domain), individual contributions from each path towards the response can be estimated. Synthesis refers to the summation of the individual path contributions in order to predict the overall response levels. In general, the estimation of transfer functions incorporates modal measurements using the shaker or modal hammer excitation to estimate the Velocity Transfer Functions (VTF) and the Noise Transfer Functions (NTFs), or the Volume Velocity Source (VVS) excitation to estimate the Acoustic Transfer Functions (ATFs). NTFs/VTFs and ATFs are measured from the source positions to the receiver positions inside the vehicle and hence, the modal characteristics of the complete vehicular transfer paths are captured. With regards to the source load estimation, some of the methods utilized in the industry are Direct Force Method, Mount Stiffness Method, Classical Matrix Inversion method, In-situ Matrix Inversion method, etc.

The Direct Force method utilizes force transducers at the source mountings to measure the transmitted interface force through each mounting. Intuitively, this method does not find much application in the automotive industry since an instrumentation of a force transducer at the mounting significantly changes the dynamics of the mount structure. The Mount Stiffness method is based upon the Hooke's Law and utilizes the difference in displacement magnitudes between the active and passive sides of the source mountings. However, the uncertainty in the dynamic stiffness levels of the non-linear soft mount bushes, especially at higher frequencies, is one major limitation associated with this method [2].

Classical TPA utilizes the Matrix Inversion (MI) method in order to estimate the transmitted interface forces across each mount. It incorporates a combination of operational measurements in source-path coupled state and modal measurements in source de-coupled state. Firstly, operational measurements are conducted in vehicle's original state with the source attached to the path, and the acceleration data acquired on the passive points of each mount position, known as 'Indicators'. Then, the source is removed from the vehicle and the Frequency Response Functions (FRFs) are estimated from the mounting position to each indicator. Ultimately, the accelerance functions estimated from the FRF measurements are inverted and multiplied with the operational acceleration values at the indicator positions in order to estimate the interface forces, according to the formula specified below:

$$\Big[F_s(\omega)\Big] = \Big[H_{is}(\omega)\Big]^{-1} \cdot \Big[\ddot{x}(\omega)\Big] \tag{2.2}$$

where $F_s(\omega)$ is the estimated source matrix, $H_{is}(\omega)$ is the accelerance matrix at the indicator positions with respect to a unit force input at the source-path interface, and $\ddot{x}(\omega)$ is the acceleration matrix obtained during operational measurements over the indicator positions. The Classical TPA method has been in use for years. However, multiple measurements to estimate the load and the transfer matrices often make this method extremely time-consuming. Moreover, the de-coupling of the transfer paths from the source leads to a change in their modal characteristics, which could result in anomalies at certain frequencies.

It is worth noticing that the interface forces measured using the Classical TPA method are specific for the transfer paths over which they are measured. The In-situ TPA method is similar to the Classical TPA method with regards to its use of MI algorithm upon measuring the operational and FRF data at the indicator positions. However, in contrast to the classical method, the in-situ method incorporates measurement of FRFs while the source is coupled to the transfer paths. The forces, hence estimated, are referred to 'Blocked Forces', and are invariant in nature, which refers to their independency from the transfer paths. However, in-situ measurements are often not feasible due to the inability to access certain mount positions in order to perform modal hammer or shaker based FRF measurements in assembled state. Nevertheless, the in-situ blocked force TPA method ensures the maintenance of complete vehicle boundary conditions by incorporating measurements in a source-path coupled state and hence, eliminates the prime drawback associated with the Classical TPA method.

The TPA techniques, as discussed so far, are used within a detailed Source-Path-Receiver based investigative approach. However, a common limitation with all the four discussed methods is their extremely time-consuming nature, which is largely associated with the FRF measurements for the transfer path estimation. Nevertheless, such dedicated measurements are definitely worthwhile to be conducted in the early vehicle development stages.

2.3 Operational Transfer Path Analysis

Another approach is to set up a Path-Receiver based model at the complete vehicle level using the operational excitations alone. Operational TPA (OTPA) is one such technique. Instead of relying upon the traditional modal methods, OTPA utilizes the actual excitation signals in order to estimate the transmissibility functions from each path position to the response position, resulting in the estimation of more realistic transmissibility functions in dynamic state, unlike FRFs which are inherently static in nature. OTPA deploys the modern signal processing algorithm of Singular Value Decomposition (SVD) in order to reduce the cross-talk among the individual contributions from the considered transfer paths. Next, Principle Component Analysis (PCA) is deployed in order to enhance the Signal-To-Noise Ratio (SNR) by eliminating the noise content within the acquired operational dataset. OTPA's efficiency and time-saving nature have made it stand out as an important troubleshooting tool during the post-production phases across OEMs. Lohrmann et al. discussed the OTPA measurement setup over a vintage Volkswagen Wartburg 311, and highlighted intake and exhaust as the major contributors towards the in-cabin sound pressure levels [8]. Ström illustrated the use of OTPA to estimate the relative ranking for different air-borne and structure-borne propagation paths through the secondary suspension of a train bogie [9]. Zhang et al. illustrated the use of OTPA in highlighting structure-borne contributions at the driver's seat through the four cabin mounts [10]. Ozaki and Sakamato presented a classification of interior sound within Honda Accord during vehicle acceleration condition into air-borne and structure-borne contributions by implementing OTPA [11]. However, being inherently a mathematical regression model (with the response levels being the dependent variables and the individual path excitations being the independent variables), OTPA well and truly demands special attention with regards to its implementation.

OTPA-estimated path contributions are extremely sensitive to vehicle instrumentation, which means that neglecting a path within the OTPA model will result in erroneous contribution results from other paths as well. This is true specifically for coherent paths. However, an exclusion of an incoherent path, such as paths related to road noise propagation, etc., will not lead to an issue with other coherent contributions. However, this will mean that the synthesized data might not match the operational levels, which will render the complete OTPA model doubtful. Hence, care has to be taken in order to include all the transfer paths within the model, in order to ensure the estimation of the correct individual contributions and the overall synthesis. Toome discussed the significance of correct number of reference sensors and their accurate placement during the measurement towards ensuring a good SNR and accurate contribution results using OTPA, especially when dealing with air-borne sources. He further emphasised upon consideration of lower and higher number of reference sensors at lower and higher frequencies respectively to ensure better CTC at lower frequencies [12]. It is important to note that OTPA results are extremely dependent over the vehicle assembly state, in a sense that any change with regards to vehicle build (source or transfer path change) shall ultimately lead to a change in the individual path contributions towards the response. Hence, the OTPA-estimated transmissibilities are strictly applicable to be utilized only for troubleshooting purposes for a particular assembly state upon which the analysis has been conducted. Fernández et al. presented OTPA's application for air-borne and structure-borne noise distinction from the tires of a Volkswagen Golf 5, along with a dedicated discussion over the formulation of OTPA models. A need for differentiated and incoherent system excitations as an input to the OTPA model was emphasized upon, and various quality checks for the OTPA model validation were summarized [13].

2.3.1 Cross-Talk Cancellation

Cross-talk refers to unwanted transfer of signals between the measurement channels. Noise and vibration transfer from e-machines into the body is inherently coherent, which means that the transmissibilities from each of the transfer paths to the response position are practically coupled to each other with the cross-talk. Hence, OTPA incorporates Cross-Talk Cancellation (CTC) in order to reduce the cross-talk among the considered transfer paths. CTC enables the determination of transmissibility functions upon the consideration of all the reference and response positions, and hence accounts for the cross-talk among the considered transfer paths. This is essential not only to estimate relatively accurate path contributions from each of the reference positions to the response position, but also to minimize the overestimation of the synthesized response. CTC deploys Singular Value Decomposition (SVD) and Principle Component Analysis (PCA) over the reference position dataset for transmissibility estimation. Roots of CTC-based OTPA method can be linked to the classical Multiple Input Multiple Output (MIMO) method. Bendat discussed the possibility for the system identification using a MIMO approach back in 1976 [14]. Ossipov et al. later highlighted the similarity between OTPA and MIMO methodologies and presented OTPA algorithm as a least-squares estimate, but with an incorporation of SVD and PCA in order to estimate incoherent path contributions [15].

Assuming [X] to be the operational data matrix for 'm' reference positions over 'r' distinct measurement blocks, and [Y] be the response matrix over 'n' response positions, the transmissibility matrix, [H], can be estimated as:

$$\Big[Y\Big] = \Big[X\Big] \cdot \Big[H\Big] \tag{2.3}$$

with [X] being a [r × m] matrix, [Y] being [r × n] matrix and [H] being [m × n] matrix. In a case where [X] is a square matrix, i.e., r = m, [H] can be estimated as:

$$\Big[H\Big] = \Big[X\Big]^{-1} \cdot \Big[Y\Big] \tag{2.4}$$

However, this is not true in most of the cases, for which the pseudo-inverse least-square method can be used as explained below:

$$\Big[H\Big] = \Big(\Big[X\Big]^{T} \cdot \Big[X\Big]\Big)^{-1} \cdot \Big[X\Big]^{T} \cdot \Big[Y\Big] = \Big[X\Big]^{+} \cdot \Big[Y\Big] \tag{2.5}$$

where $[X]^+$ is known as a pseudo-inverse solution for the inverted [X] matrix. However, the estimation of [H] matrix using this method is extremely prone to errors in cases where the operational signals in the [X] matrix are highly coherent and are contaminated with noise signals. Since this is a typical case with excitations in EVs, estimation of [H] matrix using pseudo-inverse least-square method is not recommended.

OTPA deploys CTC based upon SVD and PCA algorithms in order to estimate $[X]^+$ upon accounting for the cross-talk. SVD decomposes the operational dataset ([X] matrix) into individually orthogonal components, which are called the singular values or the Principle Components (PCs). Basically, it refers to a transformation into an orthogonal space of linear independent principal components, similar to an eigenvalue analysis. In a scenario where SVD is deployed over a motion dataset acquired on a vehicle, PCs can be loosely interpreted as mode shapes. The PCs estimated using the most coherent components from [X] become the major singular values of the dataset. Ultimately, [X] matrix can be represented in its SVD form as:

$$\Big[X\Big] = \Big[U\Big] \cdot \Big[\Sigma\Big] \cdot \Big[V\Big]^{T} \tag{2.6}$$

where [U] is an [r × m] unitary and column-orthogonal matrix, [Σ] is an [m × m] diagonal (square) matrix with the singular values along the diagonals, and [V] is an [m × m] unitary column-orthogonal matrix. The pseudo-inverse solution for $[X]^+$, and [H] can hence be found as:

$$\Big[X\Big]^{+} = \Big[V\Big] \cdot \Big[\Sigma\Big]^{-1} \cdot \Big[U\Big]^{T} \tag{2.7}$$

$$\Big[H\Big] = \Big[V\Big] \cdot \Big[\Sigma\Big]^{-1} \cdot \Big[U\Big]^{T} \cdot \Big[Y\Big] \tag{2.8}$$

The [H] estimation using SVD, hence, accounts for cross-talk in the form of PC estimation, which are inherently orthogonal, or incoherent. However, in order to reduce the noise content from the estimated pseudo-inverse solution using SVD, PCA is used to estimate the PC score, [Z] for each of the estimated singular value, as shown below:

$$\left[Z\right] = \left[U\right] \cdot \left[\Sigma\right] \tag{2.9}$$

Upon discarding the singular values (PCs) with the PC score lower than a set threshold, noise cancellation can be achieved, and the noise-cancelled [H] matrix can be estimated using the modified pseudo-inverse solution, with the lower PCs set to zero, as shown below:

$$\left[H\right] = \left[V\right] \cdot \left[\Sigma_r\right]^{-1} \cdot \left[U\right]^T \cdot \left[Y\right] \tag{2.10}$$

where Σ_r is the PC matrix with lower PCs eliminated [16].

Figure 2.3 illustrates the complete OTPA algorithm. The sound pressure and acceleration signals acquired at the reference DOFs are subjected to CTC and the major PCs are estimated. Further, the cumulative PC score is estimated and the PCs with lower contributions are discarded. The total response synthesis is then obtained by summation of the major PCs with their respective amplitude factors, which in-turn are estimated upon summing up the individual contributions from each of the reference DOFs [17]. It is to be noted that the maximum number of PCs estimated is equal to the total number of reference DOFs considered within the OTPA model. Further, it is necessary to acquire as diverse reference dataset as possible. This means that OTPA measurements have to be conducted in multiple practical load cases, in order to capture all the important principle components within the estimated [H] matrix [16].

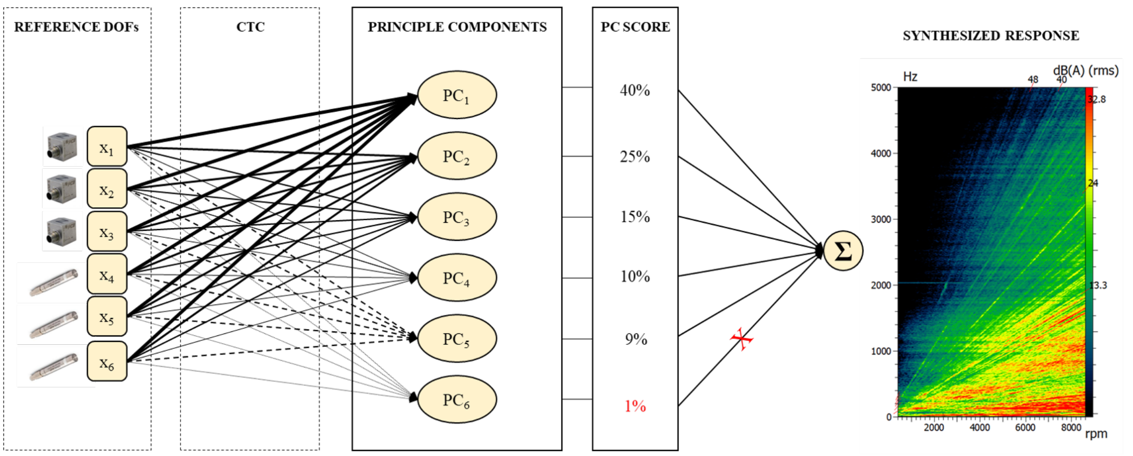

Figure 2.3: Typical approach for response synthesis using Path-Receiver based OTPA investigation.

Figure 2.4 presents a step-wise implementation undertaken within a generic Path-Receiver based OTPA investigation. Upon a satisfactory estimation of the synthesized response levels, the individual path contributions can be investigated and path ranking can be performed in order to highlight the critical transfer paths for a specific NVH concern.

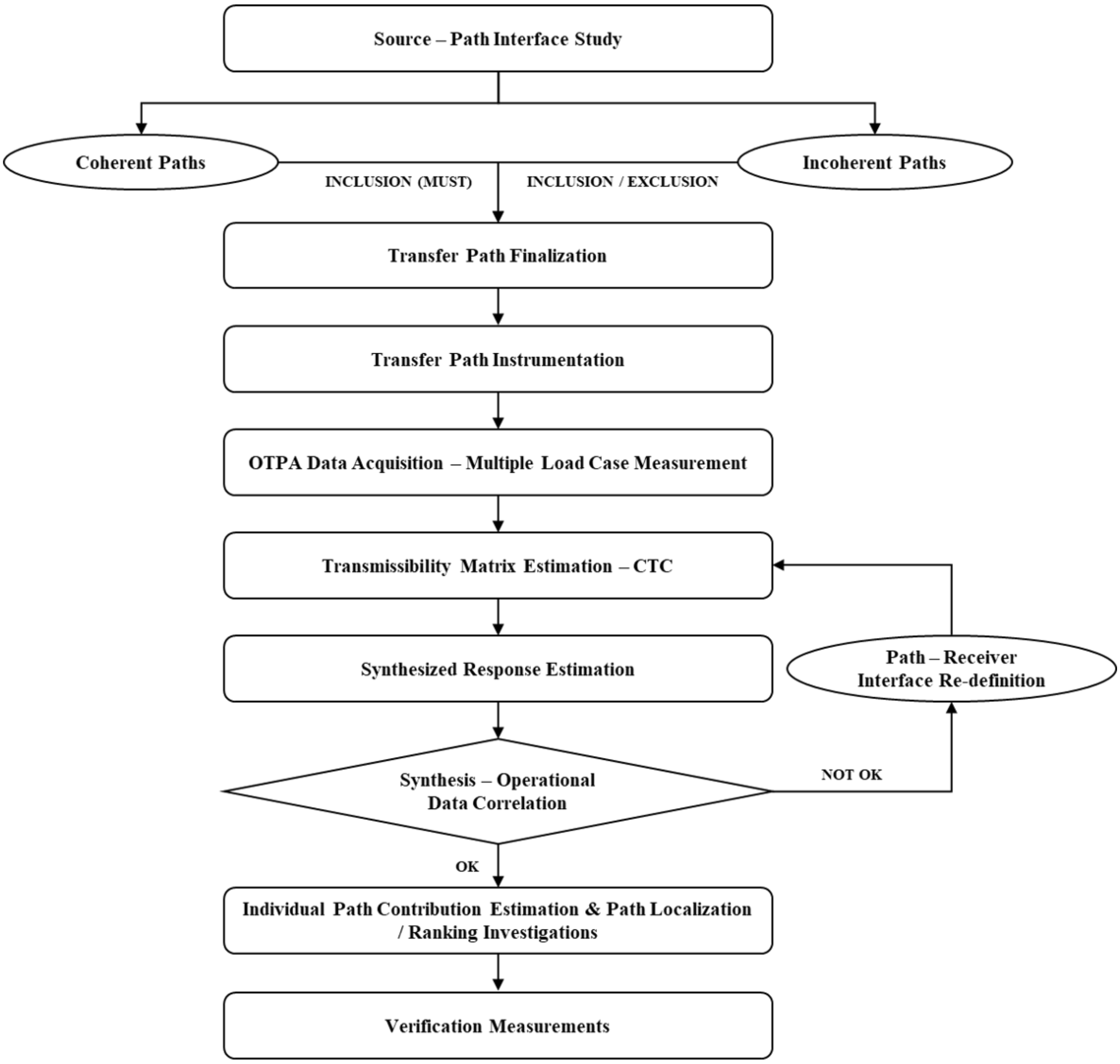

Figure 2.4: Flowchart illustrating an OTPA-based Path-Receiver methodology.

3
Methodology

In this chapter, the methodological steps followed within the project are presented. The project commenced with a detailed literature review over Transfer Path Analysis in general, followed by a deep dive into OTPA algorithm and some implemented case studies. In addition, a study of existing EV architectures and NVH challenges related to BEVs, in specific, was conducted. Literature review was followed by a dedicated CAD study of the test vehicle where the vehicle architecture, mechanical assembly/sub-assemblies and overall specifications were observed, in addition to the hunt for any parasitic air-borne or structure-borne transfer paths. In the next step, the air-borne transmissibility measurements were conducted in order to determine and prioritize air-borne DOFs within the OTPA framework. Basis the knowledge acquired during these stages of the project, the OTPA measurement setup was finalized and the operational measurements were finally conducted inside a semi-anechoic chamber over a chassis dynamometer. The research within this project has been conducted on an all-wheel driven prototype BEV. The vehicle was powered by two Permanent Magnet Synchronous Motors (PMSMs), one each at the front and rear. The front and the rear electric motor units are termed as Electric Front Axle Drive (EFAD) and Electric Rear Axle Drive (ERAD) respectively. An overview of the workflow followed during the project is presented below.

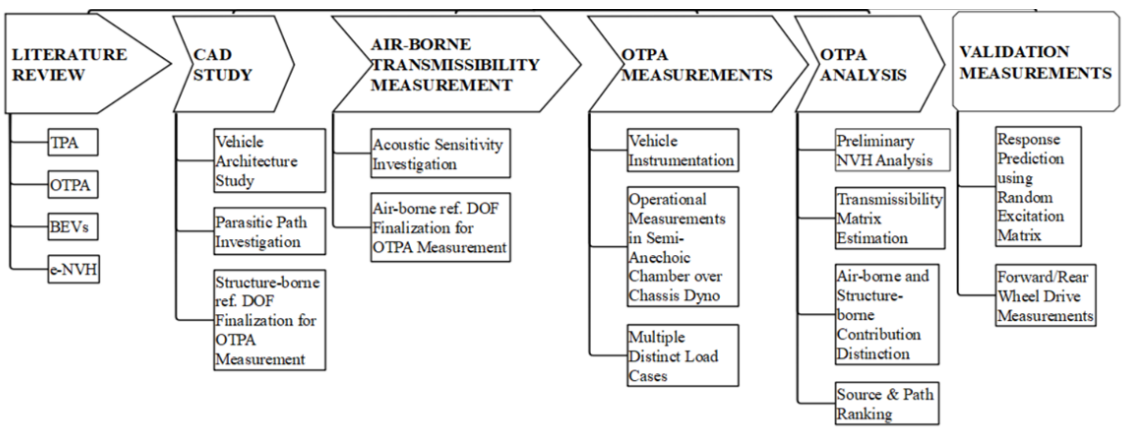

Figure 3.1: An illustration of the workflow followed within the presented Master Thesis project.

The OTPA measurement was eventually followed by an extensive data post-processing phase and ultimately, the validation measurements were performed in order to ensure the legitimacy of the formulated Path-Receiver based vehicle model. These shall be discussed in later chapters within the report.

3.1 Structure-Borne Propagation

An essential requirement of any OTPA workflow is the inclusion of all coherent paths within the measurement, so as to ensure the estimate of correct contributions from the individual sub-systems [17] [18]. Therefore, it was necessary to study the CAD model of the test vehicle in depth to reveal all possible transfer paths. The study presented in this section aims at highlighting all the existing transfer paths between the individual sub-systems and the body in the tested prototype vehicle. Eventually, it helped in finalizing the necessary structure-borne reference DOFs (accelerometer positions) to be included within the implemented OTPA framework.

3.1.1 Transfer Path Study

Since the focus during investigation was mainly the electric motor and transmission orders, special attention towards the EFAD and ERAD sub-systems was expected. In addition, any possible propagation from the drive axles to the knuckles and eventually to the body could not be neglected. Hence, the road contact and suspension systems were also studied. Further, the Heating Ventilation and Air Conditioning (HVAC) hose pipes, electric harness network, high voltage cables and ground cables were studied as the suspected parasitic transfer paths. The sub-sections below discuss the individual sub-systems in detail.

3.1.1.1 Electric Front Axle Drive Unit

Figure 3.2 illustrates the CAD model of the EFAD as installed in the test vehicle. The EFAD is connected to the cross-member/cradle by the top engine mounts. The cross-member connects to the front body side-rails, and also supports the onboard charger as well as the front invertor unit (IHFA) at the top. Towards the bottom, the EFAD can be seen connected to the front subframe by the two torque restrictor mounts. The front subframe connects to the body at two junctions each on vehicle's left hand (LH) and right hand (RH) sides. Towards the front, the impact box is connected to the body and the front subframe. In addition, a ground cable connection exists between the cross-member and the EFAD housing. At the bottom, the EFAD unit is protected by an exterior baffle.

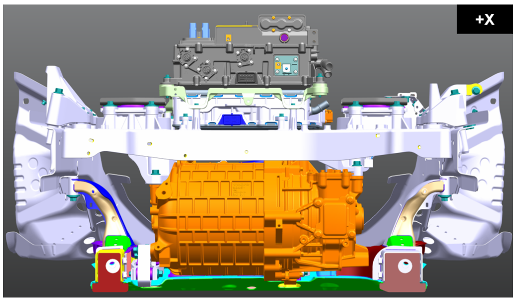

(a)

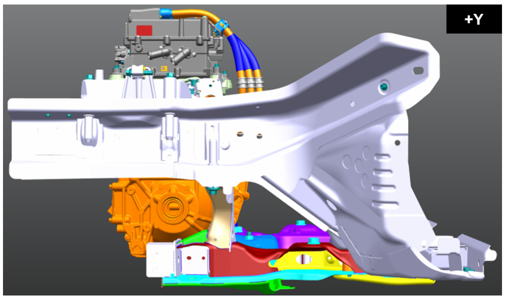

(b)

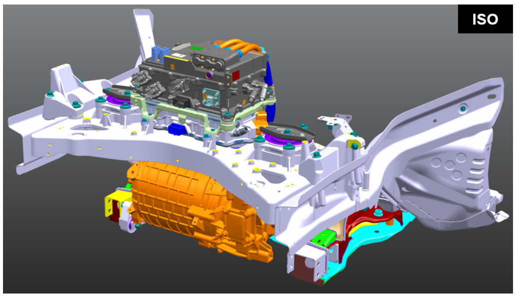

(c)

Figure 3.2: CAD illustration for the EFAD as installed in the test vehicle.

3.1.1.2 Electric Rear Axle Drive Unit

The CAD model for the rear electric propulsion unit (ERAD) is visualized in Figure 3.3. The ERAD at the rear is fitted inside the rear subframe by two mounts at the front and two mounts at the rear. The rear subframe is connected to the rear body side-rails. The rear subframe supports the rear DC-AC (voltage) converter (IEM) for the rear motor. Further, ground cable connections exist between the ERAD housing and the rear subframe, as well as the rear subframe and the body. The ERAD housing is also equipped with an encapsulation to achieve reduction in air-borne noise propagation. The under-floor panels protect the ERAD from the bottom.

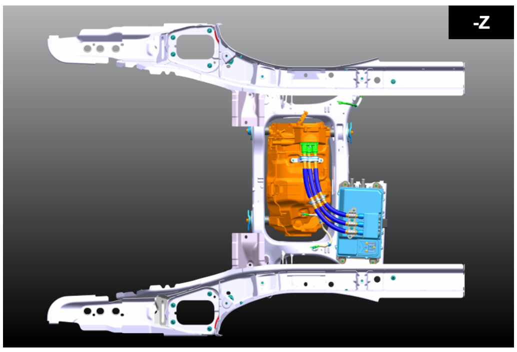

(a)

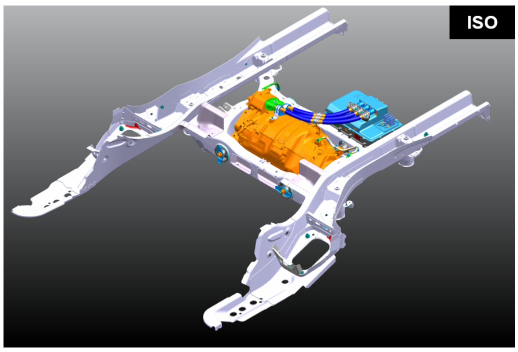

(b)

Figure 3.3: CAD illustration for the ERAD as installed in the test vehicle.

3.1.1.3 Suspension System

Figure 3.4 illustrates the CAD models for the front and the rear road contact and suspension systems as installed in the test vehicle. The suspension system comprises of MacPherson struts at the front and trailing arm multi-link suspension at the rear. The front drive axles from EFAD connect to the front knuckle bearings while the knuckles fit into the wheel hubs. The front knuckles are connected to front subframe through link arms at the bottom and to the wheel housings through the front struts at the top. The subframe can also be seen to be bolted to the body side-rails via two C-forged mounts towards the sides, and to the traction battery floor towards the rear. At the rear, the drive axles from the ERAD connect to the knuckle bearings which are fitted into the wheel hubs. The knuckles are connected to the body by longitudinal rods towards the front of ERAD. At the bottom, the knuckles are connected to the rear subframe through lower link arms. Over the lower link arms sit the parallel spring and damper units. While the springs are connected to the rear body side-rails close to the subframe's mount to body, the dampers are attached to the rear wheel housings. Further, the knuckles are also connected to rear subframes via camber and tow links.

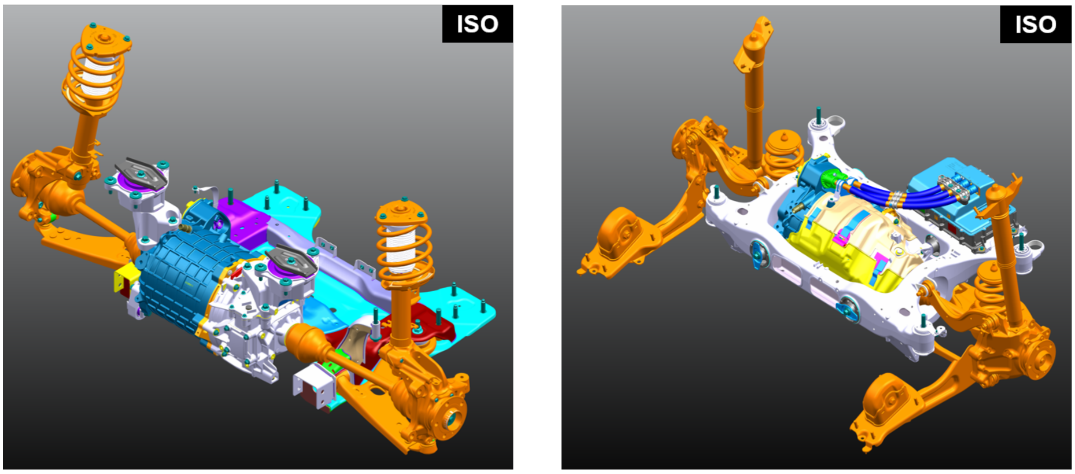

(a) Front suspension **(b)** Rear suspension

Figure 3.4: CAD illustration for the suspension system as installed in the test vehicle.

3.1.1.4 Electronic Power Steering

Figure 3.5 shows the CAD model for the Electronic Power Steering (EPS) subsystem. EPS acts as a transfer path through the firewall inside the vehicle because of the steering column's interaction with the firewall. In addition, the steering column can be observed to be attached to the steering gear, which in-turn is mounted over the front subframe. Further, the steering gear is attached to steering tierods at both ends which are connected to the front knuckles. Hence, any possibility of structure-borne transfer from front knuckles through tierods or from the front subframe through steering gear into the steering column, and hence inside the cabin, could not be neglected. Inside the cabin, steering column can also be observed to be connected to cross-member over which rests the dashboard. Hence, any leakage through the steering column into the cross-member might induce structure-borne radiation through the dashboard panels as well. Further, the steering column interface with the firewall has been a known path for air-borne leakage inside the vehicle interior [19]. The air-borne transmissibility across the steering column and firewall interface shall be studied further in depth in the next section of this report.

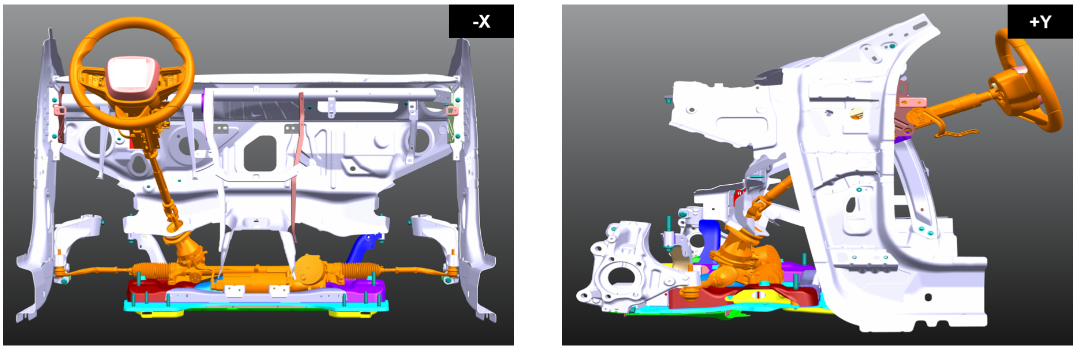

(a) **(b)**

Figure 3.5: CAD illustration for EPS sub-system as installed in the test vehicle.

It is worth noticing that the front and rear anti-roll bars have not been considered as a potential transfer path within the presented CAD study. The anti-roll bars were observed to be mounted on the subframes. Also, the front anti-roll bar was connected to the strut-mounts and the rear anti-roll bar was connected to the rear knuckles. Hence, any contribution through the anti-roll bars can be captured either at the subframe to body mounts or at the strut mounts for the front anti-roll bar and the rear knuckles for the rear anti-roll bar. Hence, the instrumentation of anti-roll bar connections was neglected in order to eliminate any chance of over-prediction through the considered transfer paths.

3.1.1.5 Parasitic Paths

In addition to the main transfer paths as discussed above, vibroacoustic energy (at higher frequencies in particular) can transmit through parasitic paths. By parasitic paths, one refers to the unexplored paths within a general system which might be a potential contributor towards vibration or noise transfer [20]. The omission of parasitic paths during an OTPA measurement might lead to erroneous contribution results upon analysis and hence, a deep dive into such suspected paths was necessary. The following sub-systems were studied in this section as suspected parasitic paths:

1. Firewall
2. HVAC system
3. High Voltage (HV) cables
4. Electronic harness and ground cables

The firewall separates the passenger compartment from the front e-machine bay. Figure 3.6 illustrates the CAD model for the firewall unit in the test vehicle. Further, Figure 3.7 represents the schematic model of the firewall, with various interfaces on its surface highlighted. With a large number of mechanical cables, climate unit and cooling hoses, as well as electric harness traversing through, the firewall becomes a suspect for the possible air-borne propagation due to leakage across the highlighted interface locations. Hence, an air-borne transmissibility measurement was planned across the firewall, the results from which have been discussed further in the next section of this report.

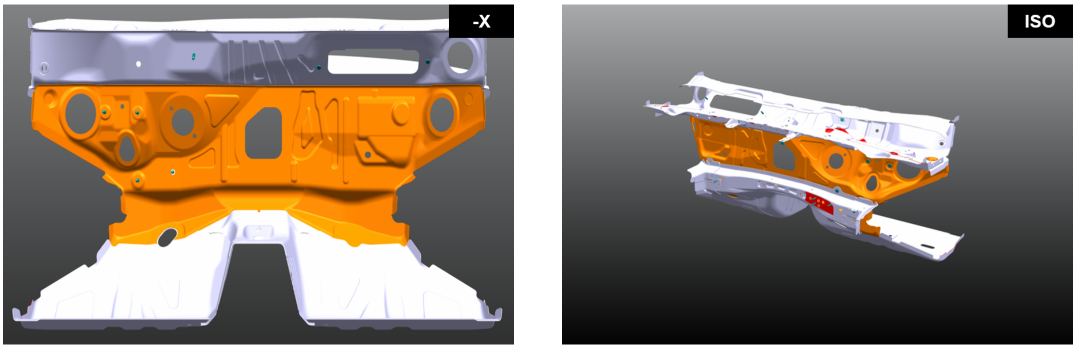

(a) **(b)**

Figure 3.6: CAD illustration for the firewall as installed in the test vehicle.

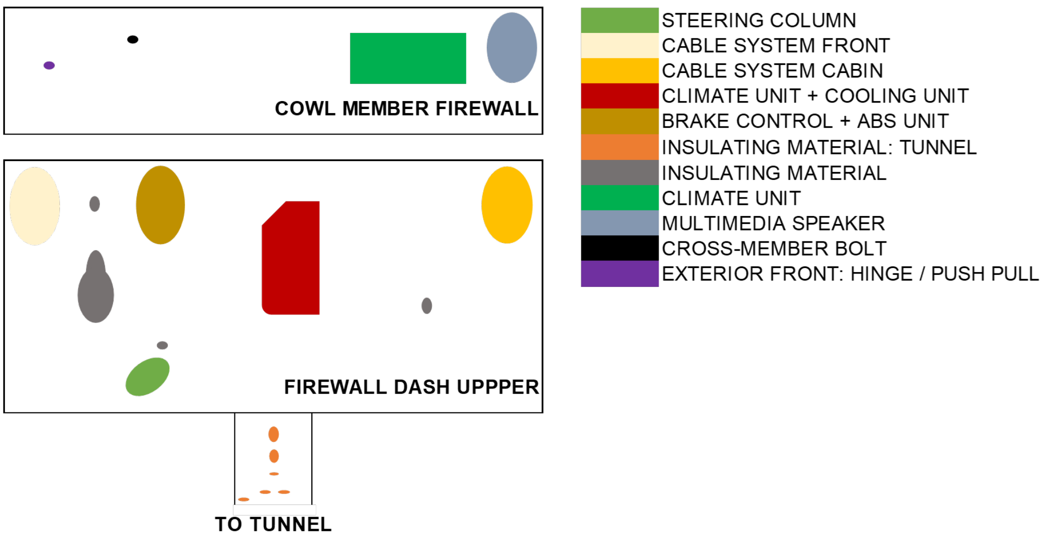

Figure 3.7: Schematic model for the firewall as installed in the test vehicle.

The HVAC system in the test vehicle can be classified into (i) thermal management and (ii) climate comfort systems. Thermal management system comprises of a radiator fan assembly bolted to the body at the front, expansion tank seated over body on soft rubber bush arrangement, water pump mounted over EFAD mount and the cooling pumps mounted over EFAD housing. The climate comfort system comprises of an encapsulated air compressor mounted on EFAD housing in the front, an electric heater mounted on the firewall and an air distribution unit which extends into the cabin through the upper firewall. Figure 3.8 illustrates the CAD model of the HVAC unit as installed in the test vehicle. The HVAC system comprises of a number of hose pipes extending all along the front e-machine bay and into the cabin through the firewall. The ERAD cooling hose bundle extends all along the central tunnel floor towards the rear of the vehicle, as can be seen in Figure 3.8a. Further, the traction battery cooling hoses can be observed to be connected to the battery panel at the bottom, as shown in Figure 3.8b. The climate comfort/air-conditioning hose pipes can also be seen to cross the firewall in Figure 3.8c. Hence, the HVAC hose bundles became a possible suspect towards high frequency noise and vibration transfer. While the hose pipes act as structure-borne paths, the climate unit ducts and the interactions of climate unit hoses with the firewall become a suspected contributors towards acoustic leakage.

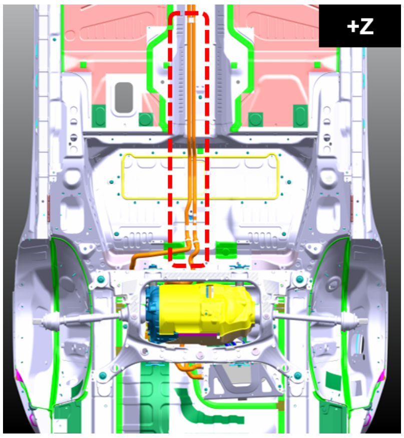

(a) ERAD cooling hose

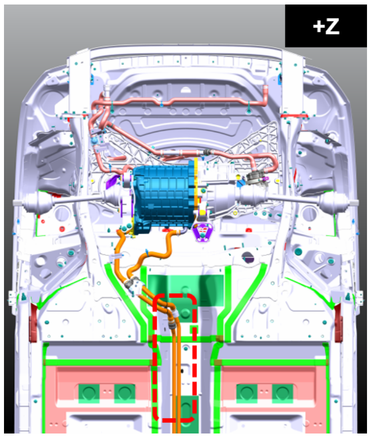

(b) EFAD cooling hose

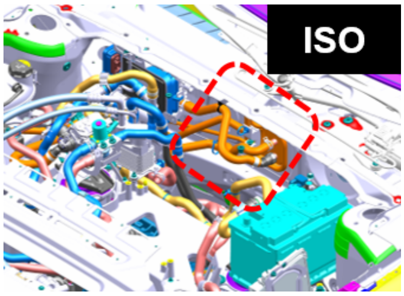

(c) Climate comfort hose

Figure 3.8: CAD illustration for the HVAC unit as installed in the test vehicle.

Stiffness of High Voltage (HV) cables in an EV architecture makes them a suspected structure-borne transfer path. The HV cables in the tested prototype vehicle can be observed to be attached to the central tunnel, as shown in Figure 3.9. The HV cables carry DC current from the traction battery to the front and rear inverter units, which are mounted on respective subframes. Hence, there is a possibility of energy getting transmitted from the EFAD/ERAD through subframes and inverter assemblies along HV cables into the body. In addition to HV cable network, ERAD cooling hoses and brake lines can also be seen attached to the central tunnel.

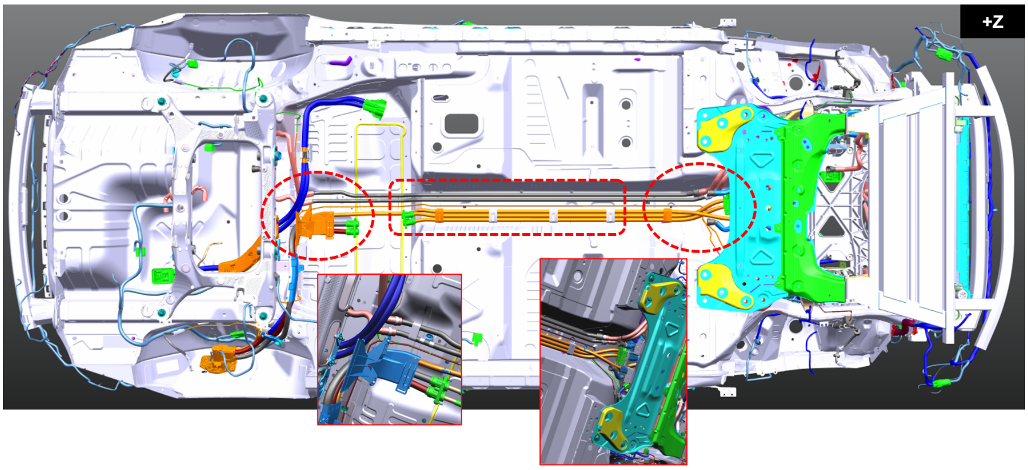

Figure 3.9: CAD illustration for the HV cable system as installed in the test vehicle.

Finally, assuming the front and rear e-machine bays as the active systems and the cabin interior as the passive system, electric harness network was studied and the interfaces where the harness interacts with the body were highlighted. Figures 3.10a and 3.10b illustrate the electric harness network in the front and the rear of the vehicle respectively. As can be observed in Figure 3.10a, the front harness system interacts with the firewall through two bundles, one towards the left and other towards the right of the vehicle. Since the cables passing through the right interface extend all along the cabin panels, it became a suspected parasitic (structure-borne) path. Further, the rear harness network can be observed to interact with the cabin through the wheel cowl on the rear left side in Figure 3.10b, making it a possible parasitic path as well. Furthermore, recent studies also hold the ground cables accountable for high frequency structure-borne propagation [21].

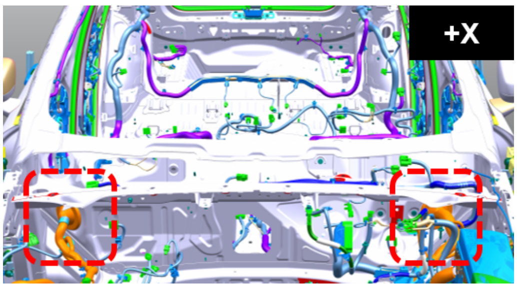

(a) Front electric harness network

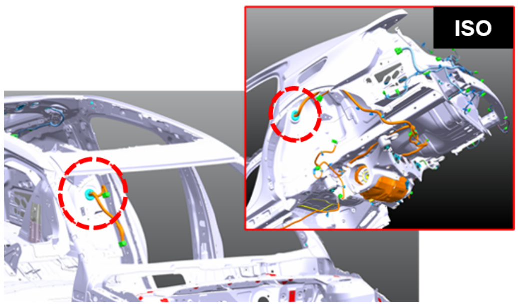

(b) Rear electric harness network

Figure 3.10: CAD illustration for the electric harness network as present in the test vehicle.

3.1.2 Instrumentation

Detailed investigation of potential structure-borne transfer paths during vehicle CAD study enabled the selection of critical vibration transfer paths from the EFAD and ERAD to the body. Taking all the coherent transfer paths into consideration, accelerometer positions were selected not only for the EFAD and ERAD assemblies but also for parasitic paths as highlighted in the earlier section. Figure 3.11 illustrates the chosen accelerometer positions for estimating the structure-borne contributions from ERAD. Vibrations from ERAD shall be transmitted through the subframe mounts to the rear body side-rails, which shall be captured by accelerometers at positions from label 26 to 29. Vibrations from rear drive shafts shall be captured at rear knuckles (label 30 and 31), and further propagation to body shall be captured beyond the longitudinal rods (label 32 and 33) at the front and over suspension (seated over lower link arm) at the rear wheel cowl (label 34 and 35). Note that the path leading from the lower link arm to rear body side-rail through the rear spring was neglected since the mount position was observed to be in close proximity with the subframe mount (label 28). Thus, an inclusion of another sensor at this location might lead to enhanced cross-talk among the two reference sensors. However, in order to not completely neglect the rear spring connection at the body side-rail, a decision to investigate the path was made in case an enhanced contribution over paths with the labels 32 or 33 but not over 34 or 35 was later revealed upon OTPA investigation. Further, the camber and tow link connections were also neglected since they did not attach directly to the body, and their contribution shall be captured by already considered reference sensors.

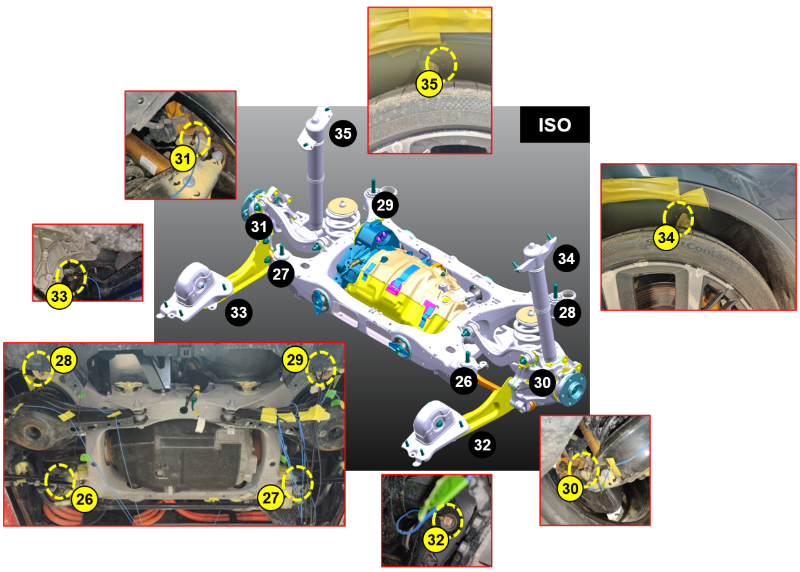

Figure 3.11: Image showing the structure-borne reference DOF positions for ERAD as instrumented for the OTPA measurement.

Figure 3.12 shows the chosen paths for estimating the structure-borne contributions from EFAD. At the top, the energy transmitted from EFAD assembly into body side-rails shall be captured on the passive side of top mounts (label 56 and 57) and on the passive side of the cross-member mounts (label 37 and 38). Towards the bottom, the energy transmitted across the lower torque rods shall be captured at paths with the label 50 and 51. Further transfer of energy through the front subframe to body shall be captured at paths with label from 39 to 42 towards the rear and 43 and 44 towards the front. To accommodate for any vibration transfer though the front drive axle, accelerometers were mounted on front knuckles (label 47 and 48) and the front strut mounts (label 45 and 46).

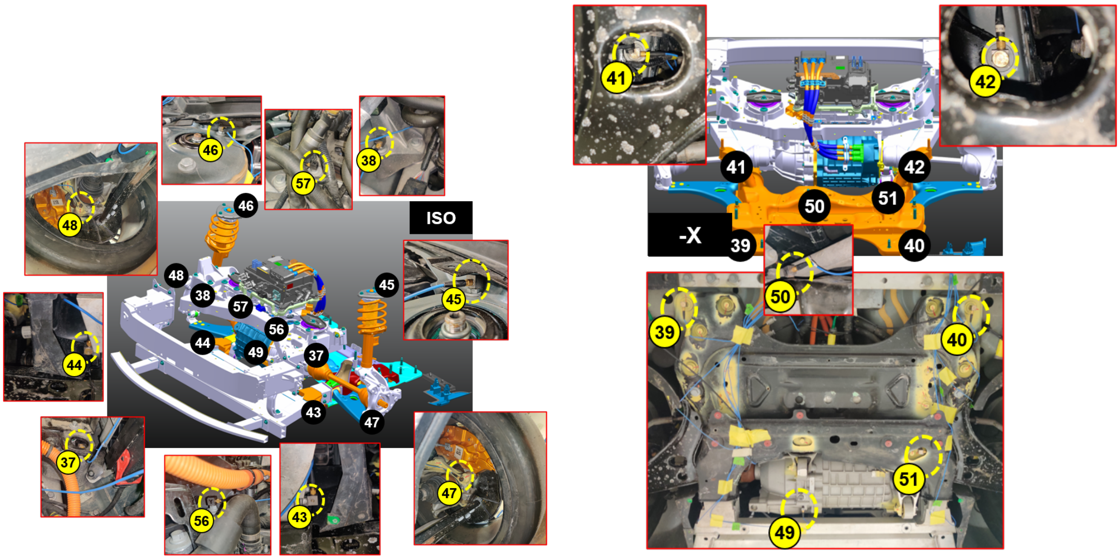

(a) (b)

Figure 3.12: Image showing the structure-borne reference DOF positions for EFAD as instrumented for the OTPA measurement.

Additionally, parasitic paths were instrumented using four accelerometer positions as shown in Figure 3.13. Paths with the label 52 and 53 relate to structure-borne contributions from the firewall. Also, this is in accordance with the increased acoustic sensitivity reveled at the firewall below 1 kHz during the air-borne transmissibility measurements (as discussed in the next section of the report), and might prove helpful in quantifying the structure-borne radiations from the firewall. Moreover, accelerometer over path label 53 shall indicate vibration transfer through the cabin harness network. Towards the bottom, accelerometers were mounted at the tunnel towards the front (accelerometer label 55) and the rear (accelerometer label 54) to capture any propagation through HV cables, ERAD cooling hoses or brake lines across the tunnel. Due to mounting constraints because of inaccessibility, the interface for the rear harness network with the body (Figure 3.10b) could not be instrumented, which stands as a limitation.

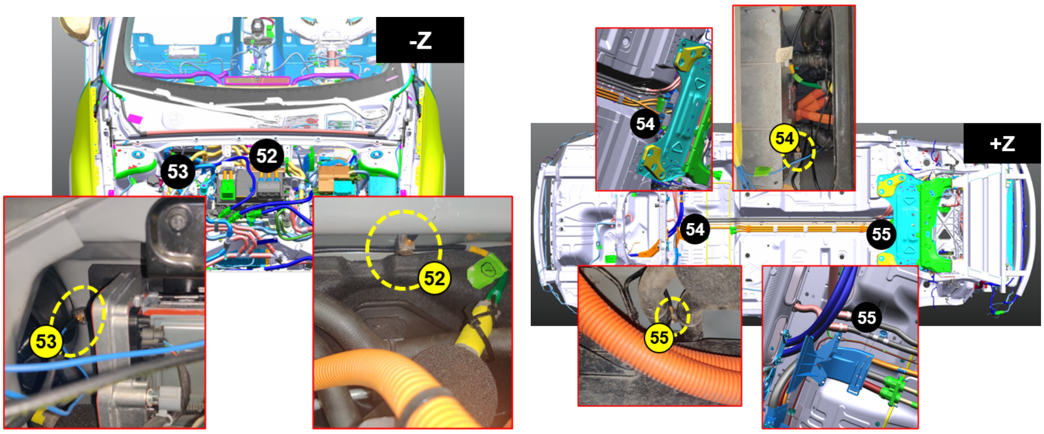

(a) Accelerometers on the firewall (b) Accelerometers at the tunnel

Figure 3.13: Image showing the structure-borne reference DOF positions for the parasitic paths as instrumented for the OTPA measurement.

Lastly, accelerometers were mounted on EFAD and ERAD housings for reference vibration (near-field) measurements, (Figure 3.14), which shall not be included in the complete vehicle OTPA model during post-processing.

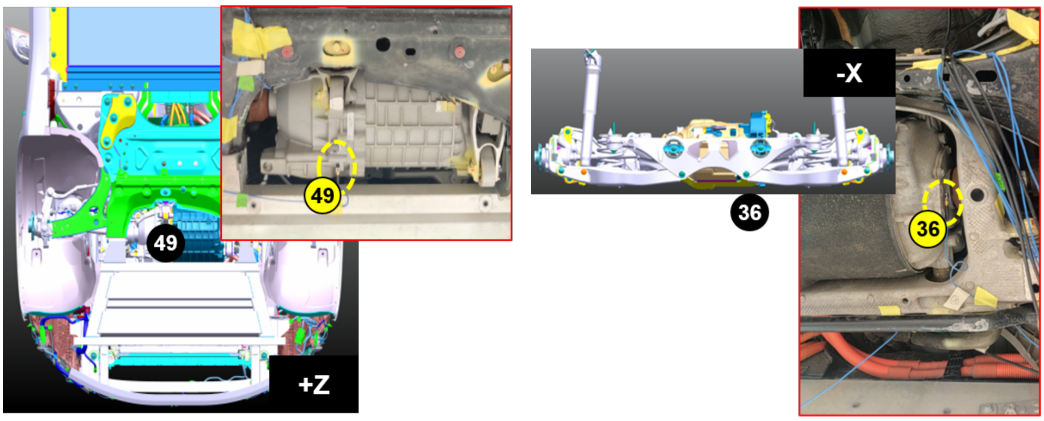

(a) EFAD reference accelerometer (b) ERAD reference accelerometer

Figure 3.14: Image showing the reference accelerometer positions for the EDUs as instrumented for the OTPA measurement.

3.2 Air-Borne Propagation

The study presented in the above section proved to be essential for identifying all possible physical interfaces between the individual sub-systems and the vehicle body. It eventually enabled the finalization of structure-borne reference DOFs within the implemented OTPA framework. However, in order to highlight the weak air-borne paths, it was necessary to gain insights on sound transmissibility characteristics from EFAD and ERAD into the vehicle. Therefore, air-borne transmissibility measurements were conducted as a pre-check before the OTPA measurement in order to ensure the inclusion of all major acoustic leakages or air-borne transfer paths within the OTPA framework. Based on the CAD study and the experience gained by the team at VCC during the early development stages of the tested prototype vehicle, 19 suspected air-borne transfer paths were chosen for the measurement, which are illustrated in Figures 3.15 to 3.18.

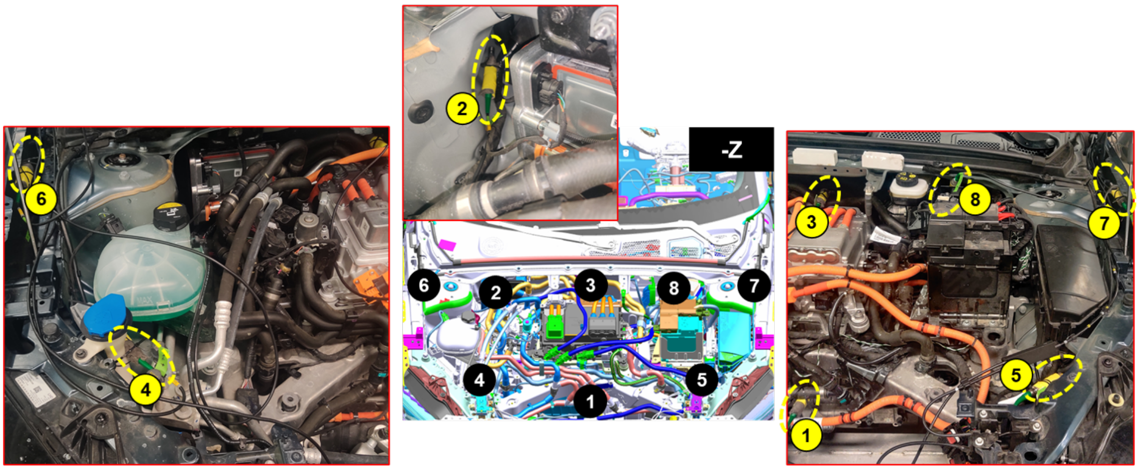

Figure 3.15: Image showing the microphone positions under the hood over EFAD for air-borne transmissibility measurements.

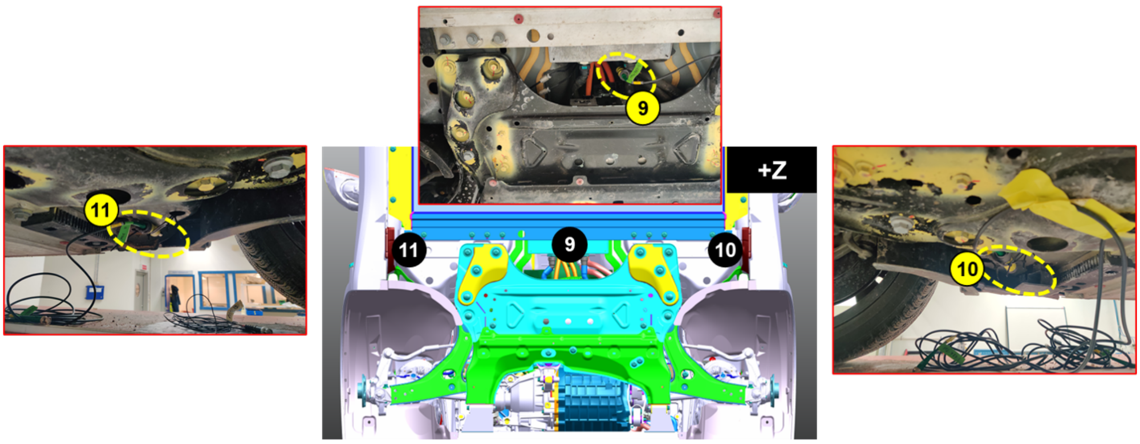

Figure 3.16: Image showing the microphone positions under the front baffle behind EFAD for air-borne transmissibility measurements.

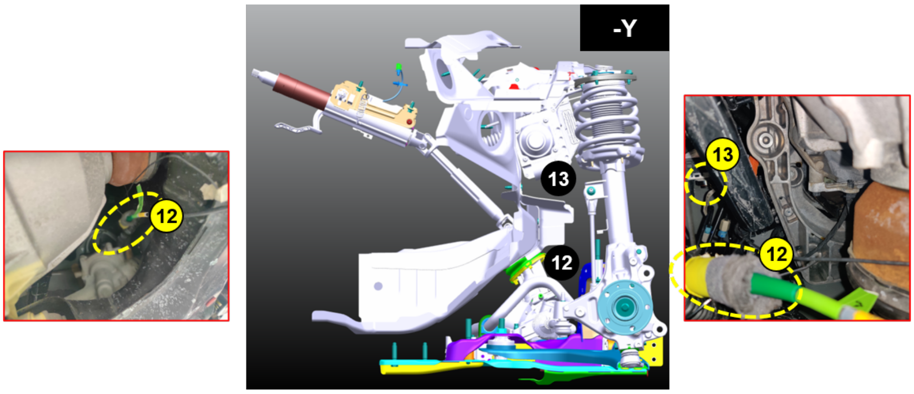

Figure 3.17: Image showing microphone positions along the steering column for air-borne transmissibility measurements.

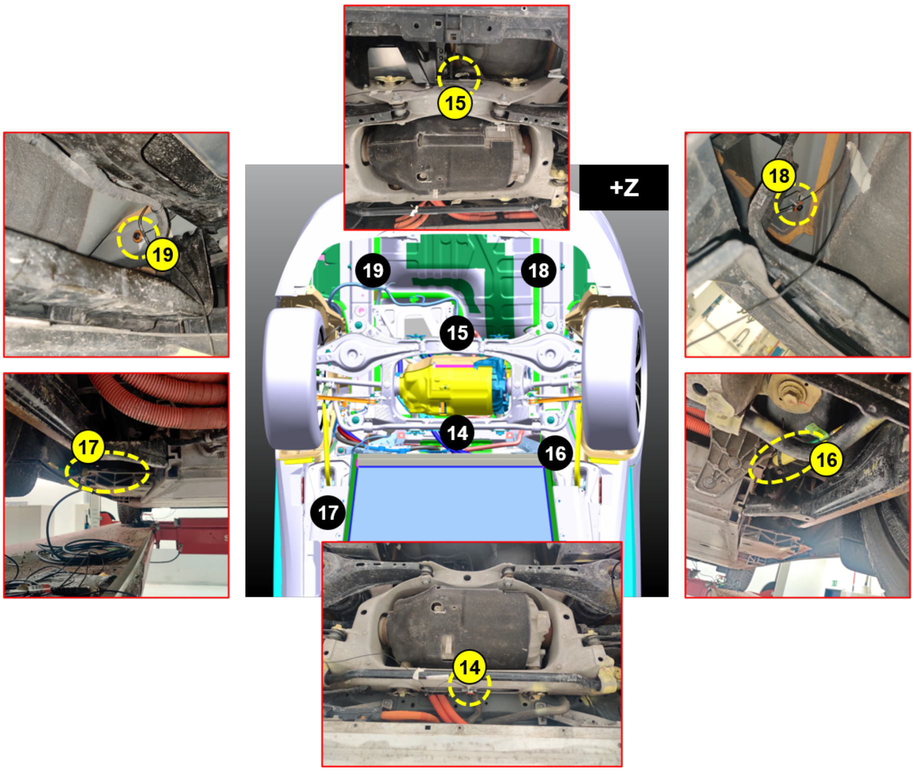

Figure 3.18: Image showing the microphone positions at the rear around ERAD for air-borne transmissibility measurements.

Sound pressure data across the specified air-borne transfer paths was acquired using a mixture of half-inch microphones and flat-bottom, rugged microphones. The high frequency sound source (loudspeaker) used within the transmissibility measurements is shown in figure 3.19. The sound source can be observed to have an attached hose with a built-in ceramic microphone at the orifice. A few of its salient features have been listed below [22]:

- High frequency ISVR MKII omni-directional sound source with a frequency range of 200 Hz to 10 kHz.

- BMS 4590 Horn driver unit (8 Ω) connected to a long flexible hose, enabling easy positioning at confined locations for easier acoustic excitation of complex mechanical assemblies.

- Non-ICP type ceramic microphone fitted at the orifice and connected to the pre-amplifier in the driver unit, delivering free-field approximation at 1 m SPL.

- Hose resonance frequency at 8 kHz, much higher than the considered frequency range of 550 Hz to 6.5 kHz during the air-borne transmissibility measurements.

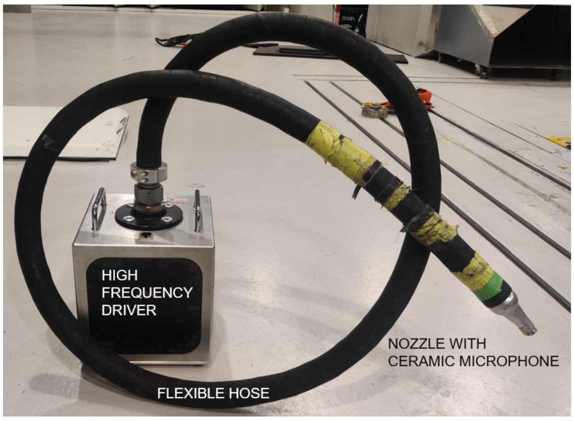

Figure 3.19: Image showing the high frequency sound source used for the air-borne transmissibility measurements.

Air-borne transmissibilities were measured from the EFAD and ERAD bays into the cabin using reciprocity measurements with the source placed inside the vehicle and the microphones installed at the suspected transfer paths. Transmissibilities were estimated using Cross-Power Spectra (CPS) for the response microphones with respect to the nozzle (reference) microphone, with the nozzle positioned close to the Driver Ear Level (DEL) inside the vehicle. Power amplifier was set to generate white noise signal in the frequency range of 550 Hz to 6.5 kHz which served as an input to the high frequency driver. Both the response and the reference microphones were connected to the Müller-BBM PAK MKII frontend [23], which has been used for data acquisition within the project. The measurements were conducted inside a semi-anechoic chamber. To estimate the transmissibilities from EFAD into the cabin, the hose was pointed towards the front of the vehicle, as shown in Figure 3.20a, and CPS for the 13 microphones at the front were determined with respect to the nozzle (reference) microphone. Similarly, the flexible hose was pointed towards the rear of the vehicle, as shown in Figure 3.20b, in order to estimate the CPS for the 6 microphones at the rear.

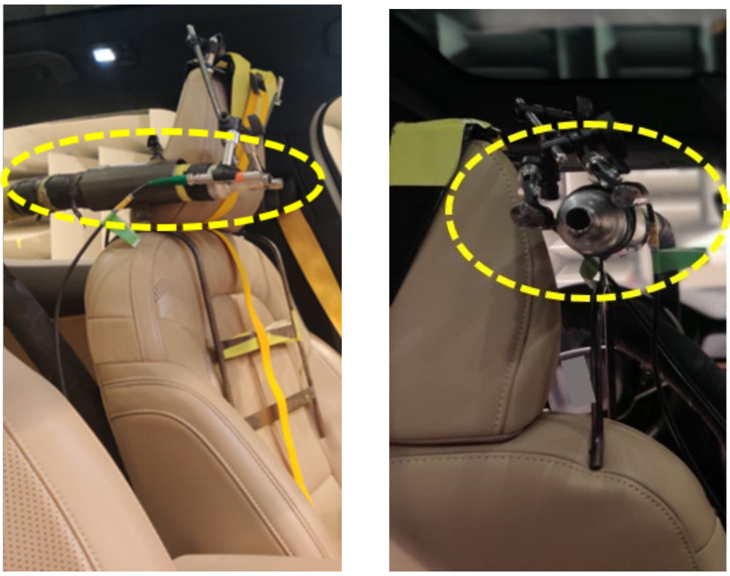

(a) EFAD transmissibility measurement

(b) ERAD transmissibility measurement

Figure 3.20: Images showing the hose mounting configurations at the DEL inside the test vehicle for air-borne transmissibility measurements.

It is worth mentioning that such measurements do not reveal absolute quantification about the air-borne path's sensitivity but, rather, prove to be a good tool to compare relative sensitivities among various air-borne transfer paths [24]. A general assumption within the measurements was the validity of the reciprocity principle, which was not completely valid because of the non-anechoic conditions which prevailed inside the vehicle and the e-machine bays, as a result of reverberance due to multiple reflections. Also, the directivity for EDUs cannot be considered similar to that of the sound source used within the measurements, which again contradicts the reciprocity assumption [25]. Further, the SPL generated by the high frequency source during the measurements was much higher in comparison to the actual SPL with operational EFAD and ERAD. Nevertheless, CPS transfer function estimate for microphones at the suspected air-borne transfer paths with respect to the reference microphone at the DEL revealed significant understanding about the relative transfer path sensitivities.

3.2.1 Acoustic Sensitivity Investigation

CPS comparison among the considered microphone positions enabled the finalization of air-borne reference DOFs across the higher sensitive air-borne paths within the OTPA framework. Figure 3.21 compares the five microphones around EFAD under the front hood. It can be observed that channel 1 shows least sensitivity across the spectrum with respect to other four channels, whereas inline sensitivity has been observed for channels 4 and 5. Further, channels 6 and 7 revealed consistently higher sensitivity levels across the spectrum, especially above 1 kHz. Hence, it can be concluded that the air-borne contributions from paths captured using channels 1, 4 and 5 can be rightly captured using channels 6 and 7, or at the microphones installed under the panels over wheel cowl cavity.

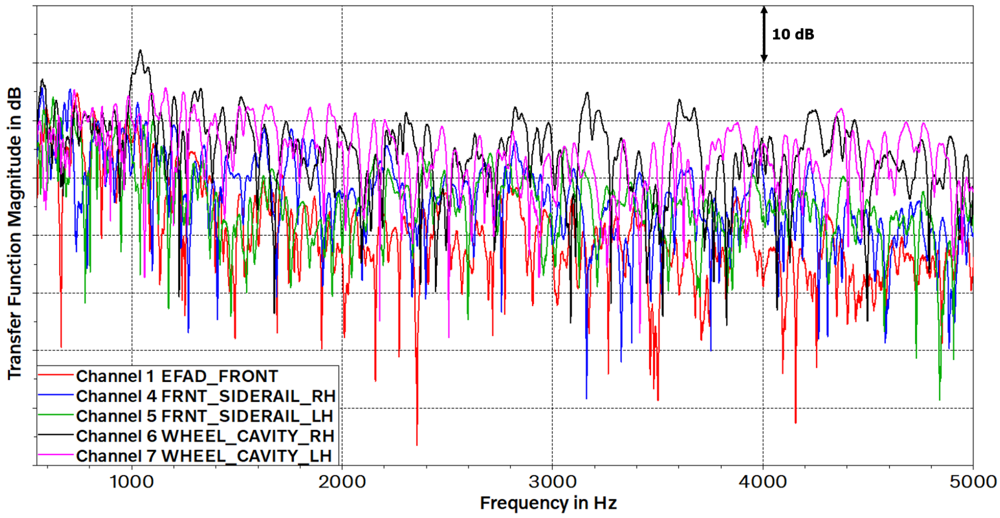

Figure 3.21: Comparison of AB transmissibility from acoustic leakages around EFAD under the front hood inside the vehicle in the form of CPS.

Figure 3.22 presents a comparison of 5 microphones installed towards the top of the firewall. It can be observed that channel 3 shows enhanced sensitivity below 1 kHz, whereas channel 2 can be observed to show higher sensitivity at higher frequencies above 3.9 kHz. Channel 2 can also be seen to dominate channel 8 above 2.6 kHz. Sensitivity for channels 6 and 7 can be observed to dominate at higher frequencies above 3.1 kHz. Hence, while the contributions from channels 2, 6 and 7 are predominant at higher frequencies, channel 3 has been revealed to be more sensitive to lower frequencies below 1 kHz.

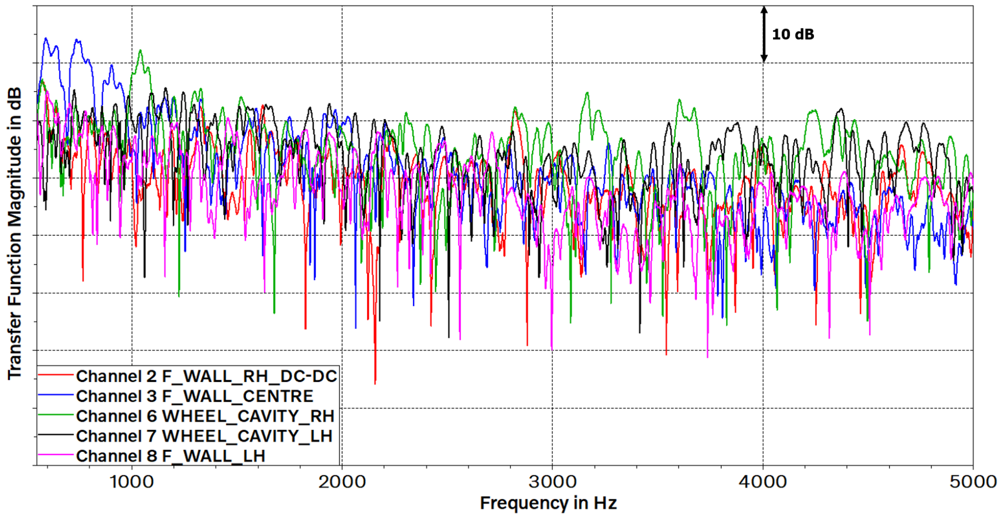

Figure 3.22: Comparison of AB transmissibility from acoustic leakages along the top of the firewall inside the vehicle in the form of CPS.

Figure 3.23 compares the sensitivities of transfer paths considered towards the rear of EFAD. Channel 12 can be observed to show consistently low sensitivity across the spectrum, which confirms insignificant leakage across the steering column's interface with the firewall. However, the region above steering column and firewall interface (channel 13) can be observed to be sensitive at frequencies above 4 kHz. Channel 9 can be observed to show enhanced sensitivity across the spectrum, which advises towards the front tunnel section being a major air-borne transfer path. Sensitivities for channels 9, 10 and 11 can be observed to be inline.

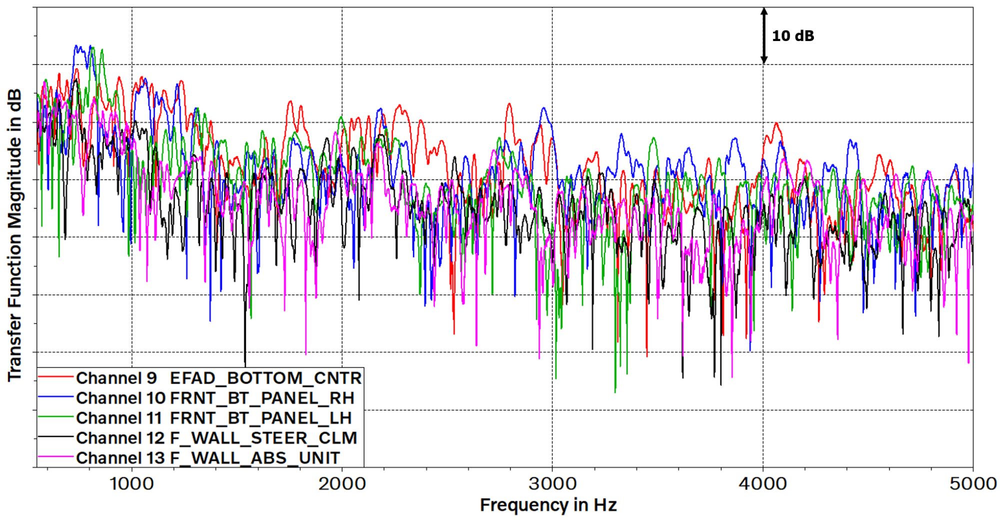

Figure 3.23: Comparison of AB transmissibility from acoustic leakages around the rear of EFAD inside the vehicle in the form of CPS.

Figure 3.24 emphasizes over the sensitivity comparison for the considered air-borne transfer paths around ERAD. Channels 18 and 19 can be observed to show increased sensitivity levels across the spectrum. Channel 14 can be observed to show enhanced sensitivity above 3.2 kHz, and enhanced sensitivity with respect to channels 16 and 17 above 1.4 kHz. Further, consistently low sensitivity levels can be observed across spectrum for channel 15 when compared to channels 18 and 19. Hence, the contributions from the rear end of ERAD (channel 15) can be interpreted to be captured with microphones installed at the rear body side-rails (channels 18 and 19).

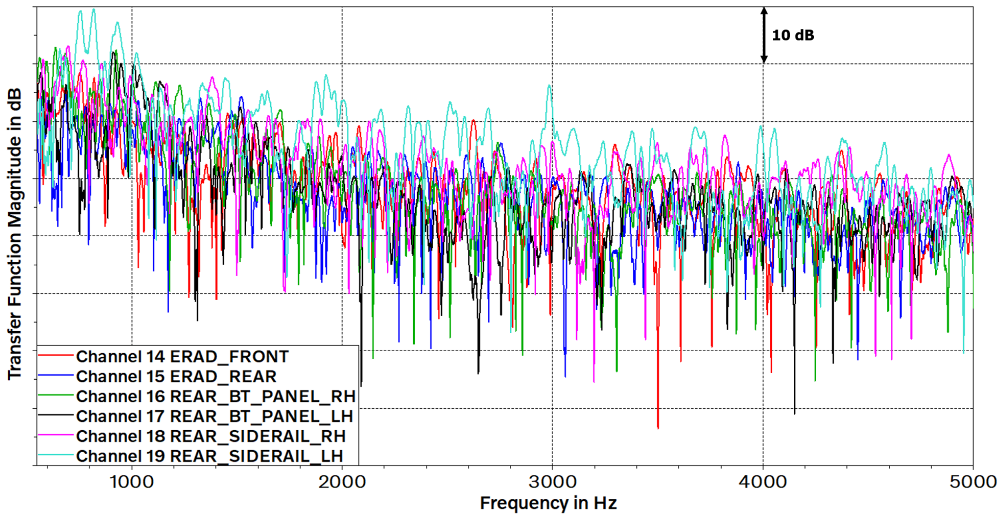

Figure 3.24: Comparison of AB transmissibility from acoustic leakages around ERAD inside the vehicle in the form of CPS.

3.2.2 Instrumentation

With reference to the above specified comparisons, the acoustic leakages which revealed higher sensitivity for noise propagation from the e-machine bays inside the vehicle became crucial air-borne transfer path considerations during the OTPA measurement. 13 such air-borne leakages were then selected to be included within the OTPA framework, 8 around EFAD (microphone label 2, 3, 6, 7, 9, 10, 11 and 13 as can be seen in Figures 3.15 to 3.17) and 5 around ERAD (microphone label 14, 16, 17, 18 and 19 as can be seen in Figure 3.18). Hence, the conducted air-borne transmissibility measurements enabled an optimized selection of air-borne reference DOFs within the OTPA framework.

With regards to the road noise, it was assumed that the orders generated by the interaction of the tire and dynamometer roller during vehicle testing do not interact with the e-machine and transmission orders at higher frequencies. Hence, incoherent air-borne transfer path from tires into the vehicle could have been neglected within the analysis. However, in order to confirm the same, 2 microphones were installed at the trailing ends of the front-left and the rear-right tires over the dynamometer, as illustrated in Figure 3.25. Additionally, 2 microphones were installed close to EFAD and ERAD housings for near-field measurements, which shall be excluded within the estimation of the transmissibility matrix (microphone label 1 and 15, as can be seen in Figures 3.15 and 3.18 respectively).

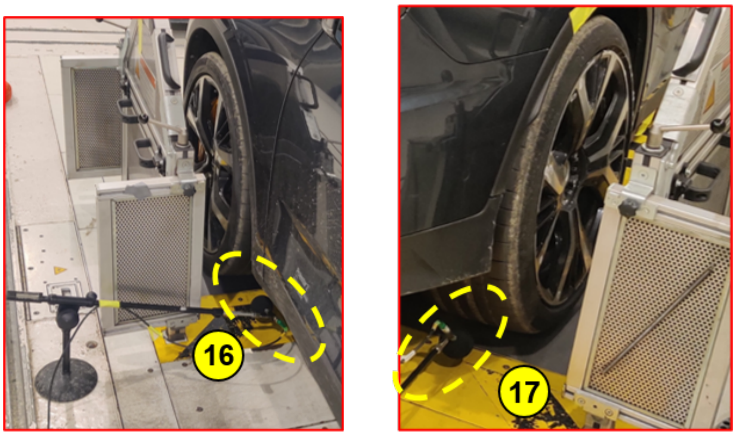

(a) Microphone position behind the front left tire

(b) Microphone position behind the rear right tire

Figure 3.25: Image showing the microphone positions for tire noise acquisition during OTPA measurements inside the semi-anechoic chamber.

4
OTPA Measurements

Upon a detailed study of the major acoustic leakages and vibration transfer paths, reference sensors were instrumented across the vehicle as detailed in the previous chapter of the report. Since the primary aim of the project is to highlight the contributions from the electric propulsion units towards the interior noise, path continuity was especially ensured for EFAD and ERAD assemblies during the finalization of the sensor positions. Further, each sensor selected to be installed at a chosen location was ensured to be a healthy indicator of that particular path's contribution for better SNR and CTC, which shall eventually lead to distinct contributions. For instance, the accelerometers around EFAD and ERAD units were mounted on the passive side and not on the active side, in order to avoid any non-linearity due to soft mounts into the considered paths, which improves SNR. This chapter further highlights the OTPA measurement details with regards to response sensor positions, measurement system interface and testing load cases.

4.1 Response Sensors

In order to capture the receiver SPL, microphone arrays were installed at the driver ear level (DEL) inside the vehicle, as shown in Figure 4.1. A combination of 4 half-inch microphones were used in order to enable the spatial averaging of SPL at the DEL position, which is essential at high frequencies when the predominance of noise directivity increases.

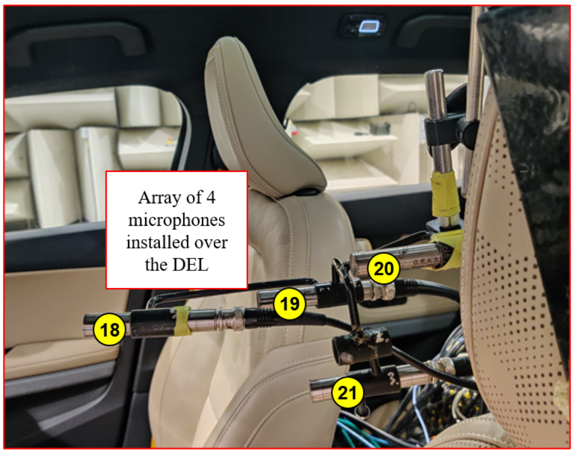

Figure 4.1: Image demonstrating the response microphone positions inside the test vehicle as instrumented for the OTPA measurements.

4.2 Measurement Setup

A total of 32 tri-axial accelerometers and 25 half-inch microphones were instrumented over the vehicle for OTPA measurements. The instrumented air-borne and structure-borne transfer paths have been summarized in Tables A.1 to A.3 in the appendix. Figure 4.2 illustrates the instrumentation diagram as followed during the OTPA measurements. Microphones and accelerometers were instrumented over the vehicle and were connected to the Müller-BBM PAK MKII systems for data acquisition (DAQ). Owing to the high count of channels (123) involved in the data acquisition, a combination of two DAQ systems were used in synchronized mode to avoid any latency in signals acquired from the two frontends. Various vehicle parameters like EFAD/ERAD RPM and torque, traction battery's State-of-Charge (SOC) and temperature, HVAC fan state (ON/OFF) and vehicle speed were acquired using the Controller Area Network (CAN) channel from the On-board Detection (OBD) module. The CAN channel input was fed to the PAK frontends, which were in-turn connected to laptop via LAN connection. For the test vehicle motoring over the chassis dynamometer, traction force was controlled from the control room workstation. In addition, vehicle driving mode was remotely controlled to be either All Wheel Drive (AWD), Front Wheel Drive (FWD) or Rear Wheel Drive (RWD) using Integrated Calibration & Application Tool (INCA) which flashed the modified vehicle parameters on the ECU module installed over the test vehicle. It is to be noted that the vehicle's default driving mode is AWD, where both the EFAD and ERAD are operational. However, measurements in vehicle's FWD and RWD configurations shall help to understand high frequency noise and vibration propagation from the front and rear of the vehicle separately, which has also been adopted as a verification approach towards the later phase of the project.

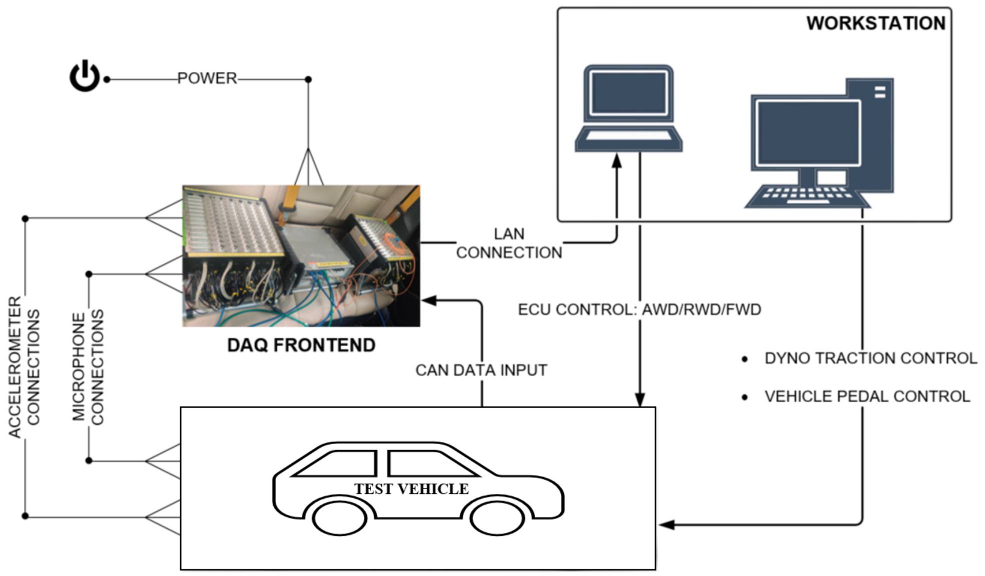

Figure 4.2: Schematic diagram detailing the instrumentation as followed during the OTPA measurements within the project.

In general, high sensitive microphones and accelerometers were used for the OTPA measurement to ensure high SNR. The following types of microphones were used to acquire the air-borne contributions:

1. B&K Type 4189: Half-inch free-field pre-polarized microphone with a sensitivity of 50 mV/Pa and frequency range of 6.3 Hz to 20 kHz.

2. GRAS TYPE 46AE: Half-inch CCP free-field microphone with a sensitivity of 50 mV/Pa and frequency range of 3.15 Hz to 20 kHz.

For vibration measurements, low sensitivity was desired for the accelerometers at the front and the rear knuckles, as well as on EFAD/ERAD housings in order avoid excessive noise content in the recorded vibration velocities. In total, the following 4 types of accelerometers were used to acquire the structure-borne contributions:

1. PCB Model TLD356A15: Tri-axial, ceramic shear ICP accelerometer with high sensitivity of 100 mV/g and frequency range of 2 Hz to 5 kHz.

2. PCB Model 356A32/NC: Miniature tri-axial, ICP accelerometer with high sensitivity of 100 mV/g and frequency range of 1 Hz to 4 kHz.

3. PCB Model 339B31: Miniature tri-axial, ICP accelerometer with a sensitivity of 10 mV/g and frequency range of 2 Hz to 8 kHz.

4. Dytran series 3023M23: Miniature tri-axial, IEPE accelerometer with lower sensitivity of 10mV/g and frequency range of 1.5 Hz to 10 kHz.

Prior to the measurement, microphones and accelerometers were calibrated in order to ensure minimal deviation from the specified sensitivities, and to accommodate for any deviation, if applicable. Flat frequency response was observed up to 5 kHz, which was desired. Finally, the measurements were conducted inside a semi-anechoic chamber over a chassis dynamometer at Volvo's NVH facility.

4.3 Measurement Load Cases

Various load cases were finalized in order to excite the test vehicle in many realistic ways. This was necessary in order to acquire sufficient operational data to estimate the transmissibility matrix accurately [26]. The vehicle was tested in Electric Wide Open Throttle (ELWOT), Electric Partial Open Throttle (ELPOT) with traction loads of 50 Nm, 100 Nm and 150 Nm, as well as ELPOTs with 35% and 45% pedal actuation. During the ELWOT/ELPOT measurements, vehicle was allowed to respond to the torque as requested by the dynamometer due to traction, the torque request being higher in case of ELWOT measurements. Also, Regenerative Braking (REGEN) tests were conducted where the test vehicle was allowed to decelerate independently. All the above mentioned load cases were performed for three vehicle configurations: AWD, FWD and RWD. The measurements were done with the

HVAC fan switched OFF. The traction battery temperature was monitored to be below 40° C and the SOC level was monitored to ensure a consistent torque output from the test vehicle's e-machines. A maximum of 8700 RPM was achieved as the test vehicle speed was swept from 5 Kph to 130 Kph in a span of 60 seconds.

Figure 4.3 illustrates the torque response during the executed load cases. Both the EDUs were operational during the AWD load cases, as was expected. It can be observed in Figures 4.3a and 4.3b that distinct torque levels were achieved above 2000 RPM in almost every AWD load case. Also, EFAD can be observed to kick-in post 2000 RPM during the AWD measurements over low traction requests, the compensation for which can be seen as increased ERAD torque response below 2000 RPM. The FWD and RWD measurements, as illustrated in Figures 4.3c and 4.3d respectively, can be considered as two distinct load cases owing to the fact that only one of the two motors is operational during these load cases. Negative torque response can be observed for REGEN load cases with each configuration. Since the torque output for the ELPOT measurement done with 45% throttle pedal actuation was similar to that of the ELPOT measurement with 50 Nm load case, a decision to rule it out from transmissibility matrix estimation was made. Lastly, ELPOT measurement with 35% throttle pedal actuation in AWD was reserved for the purpose of synthesized response verification, as discussed later in the report.

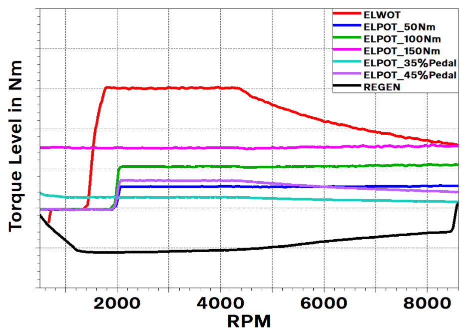

(a) AWD: EFAD torque response

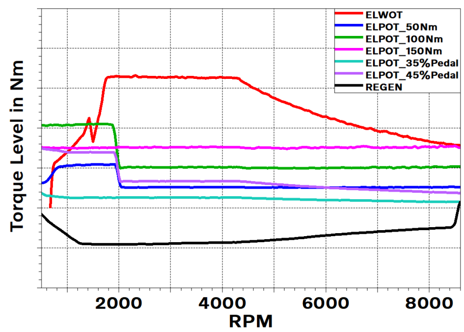

(b) AWD: ERAD torque response

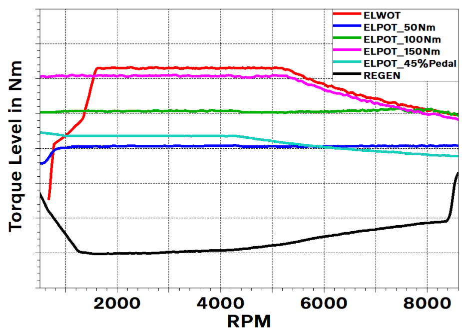

(c) FWD: EFAD torque response

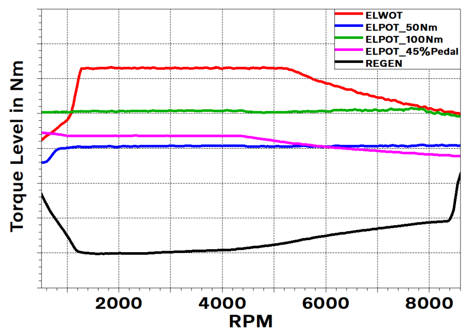

(d) RWD: ERAD torque response

Figure 4.3: Plots for measured EFAD and ERAD torque output versus vehicle RPM during OTPA measurements in 3 different vehicle configurations.

5

Analysis

5.1 Preliminary NVH Analysis

The OTPA measurements provided a large operational dataset under distinct test conditions for further analysis, following which the detailed transfer path investigation was performed. Figure 5.1 illustrates the CAD model of the electric motor and the planetary gearbox in the tested prototype vehicle, followed by a description of the important propulsion orders analyzed within the scope of this research work. As the first step, the interior noise levels at the DEL were probed and were also compared with the near-field data at the front and rear e-machines. Figure 5.2 presents the APS comparison for the interior noise in relation to the near-field noise and vibration data at EFAD and ERAD for the test vehicle in ELWOT load case. The interior noise levels were obtained upon spatial averaging of an array of four microphones at the DEL and the vibration levels were estimated after summation of velocity magnitudes in lateral, longitudinal and vertical directions. The DEL APS plot highlights the dominance of EV-specific order character over the background noise levels inside the vehicle. In addition to the main orders related to the electric motors and the transmission system, considerable side-bands and overtones were also observed, not only in the near-field noise and motor housing vibration, but also inside the vehicle. This revealed the possibility of noise contributions from the tire-dynamometer interaction, macro-geometrical or micro-geometrical defects within the gear train, etc. However, the scope of the presented research limits the investigation to orders specific to vehicle's propulsion system, which includes electric motor and transmission (gearbox).

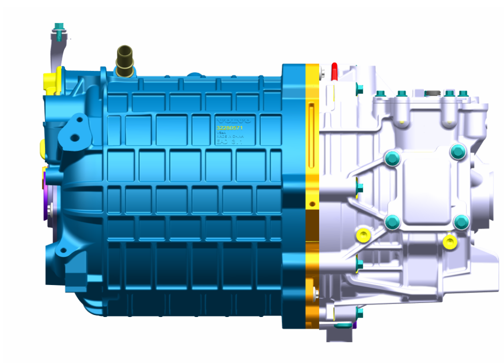

(a) E-machine

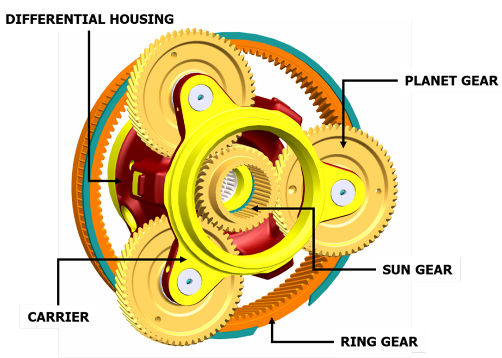

(b) Planetary gearbox

Figure 5.1: CAD illustration of the propulsion system in the test vehicle.

Order No.	Origin
13.3	Planet and Ring gear interaction inside the planetary gearbox.
24	3rd harmonic related to the 3-phase PMSM design.
32.8	Sun and Planet gear interaction inside the planetary gearbox
40	5th harmonic related to the 3-phase PMSM design.
48	6th harmonic related to the 3-phase PMSM design.

Table 5.1: Details of the propulsion-related orders within the test vehicle.

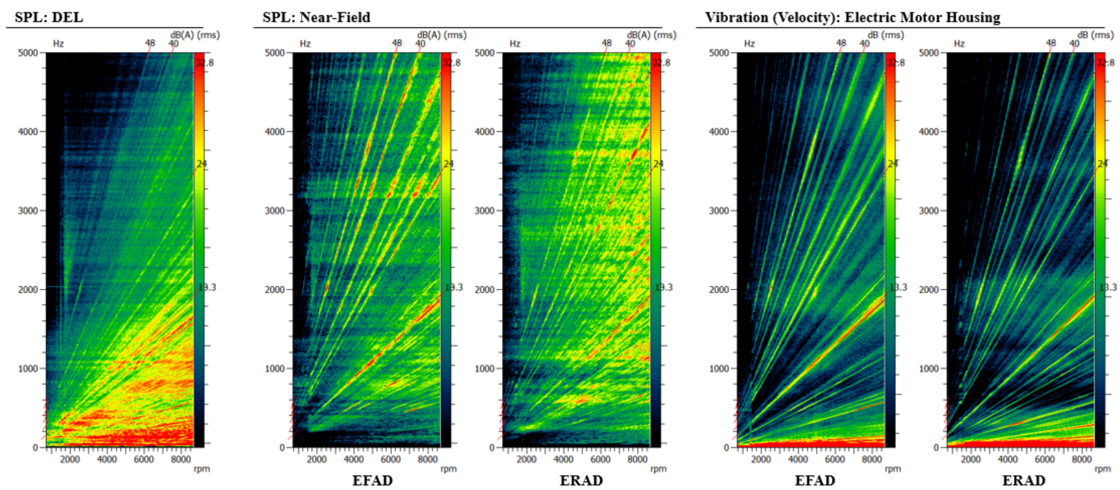

Figure 5.2: Comparison of the interior noise levels at DEL inside the test vehicle with the near-field noise and vibration levels. The plots compare the APS levels in the vehicle for a wide open throttle load case.

Order 13.3's presence can be observed across the RPM range, not only over the e-motor housings as near-field noise and vibration but also inside the vehicle. Resonance can be observed in the frequency range of 1.4 kHz to 2.1 kHz over the e-motor housings, and high frequency resonances can be observed in the near-field noise data over EFAD and ERAD above 2 kHz. Further, resonance can be observed in the interior noise around 1.04 kHz - 1.1 kHz, which also leads to the amplification of order 13.3 and its side-bands in mid-range RPM. In a similar manner, other propulsion-related orders can be observed in the interior noise, and can also be correlated with their presence in the near field noise and motor housing vibration data.

Similar studies were performed for the three other load cases - ELPOT_150 Nm, ELPOT_35% PEDAL and REGEN. An APS comparison of the interior vehicle noise in the four analyzed load cases have been presented in Figure 5.3. Again, spatially averaged data for four interior microphones at the DEL has been presented. Similar observations can be highlighted with the other three load cases, with the overall levels being relatively lower for the ELPOT_35% PEDAL test case.

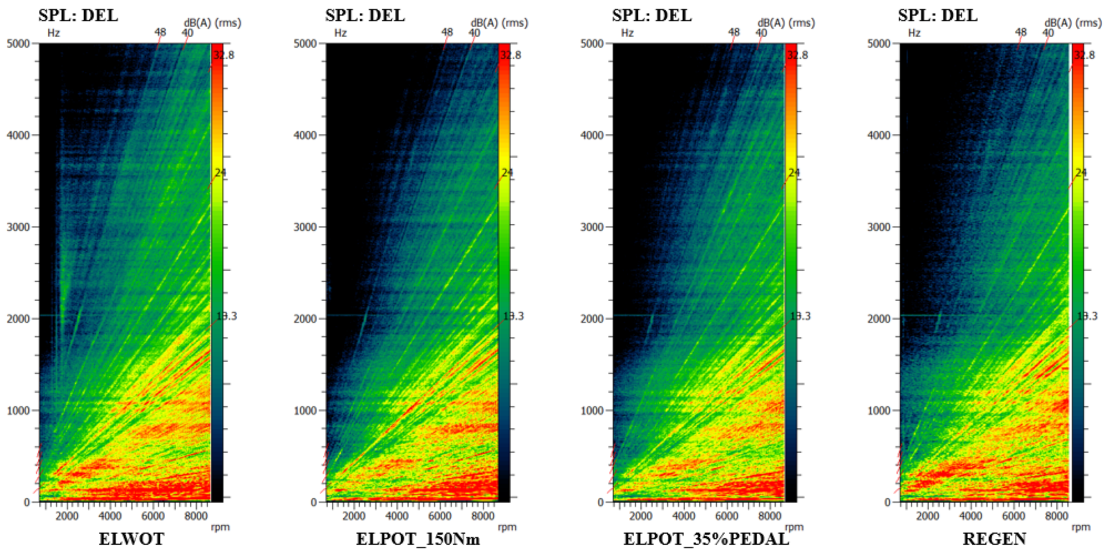

Figure 5.3: Comparison of interior noise levels at DEL inside the test vehicle in four different load cases. The plots compare the APS levels for the interior noise inside the test vehicle for ELWOT, ELPOT_150 Nm, ELPOT_35% PEDAL and REGEN load cases.

Since the absence of adequate masking noise in EVs lead to an increased annoyance associated with the propulsion noise, it is essential to define the likely audible RPM ranges for each of the considered propulsion orders in all the measured load cases [27]. Figure 5.4 illustrates the RPM ranges where the whine perception associated with the propulsion orders is likely to be audible inside the test vehicle in ELWOT load case. Tonal perception can be regarded as annoying in the RPM ranges marked as red. Hence, order 13.3 can be observed to be most likely audible among the five the propulsion orders under ELWOT load case. Further, order 24, 32.8 and 48 can be observed to be perceivable in lower RPM ranges. However, the perception of order 40 can be considered as negligible. Similar comparison were done for the other three load cases as well.

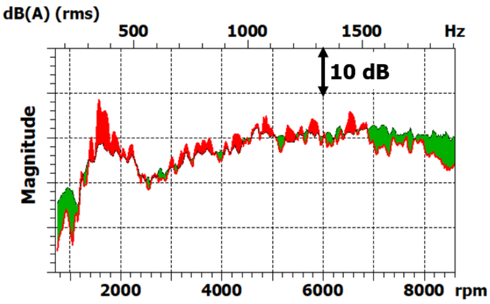

(a) Order 13.3

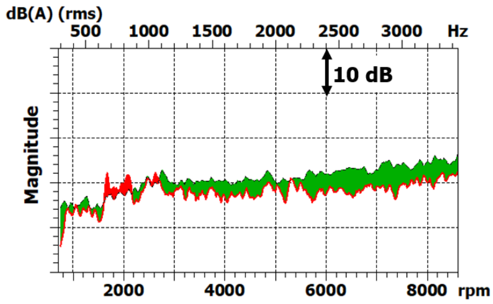

(b) Order 24

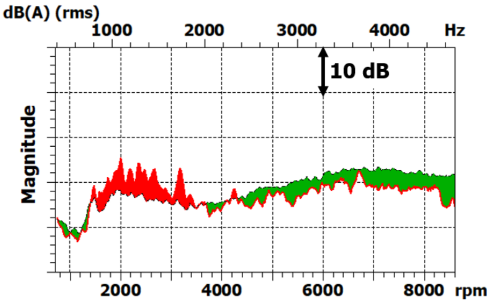

(c) Order 32.8

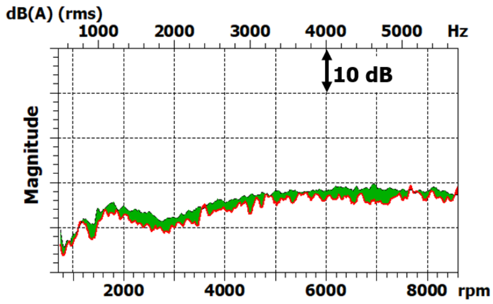

(d) Order 40

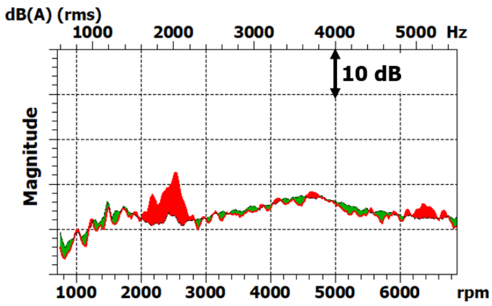

(e) Order 48

Figure 5.4: Plot highlighting the audible RPM ranges for the five propulsion orders within the test vehicle in ELWOT load case.

Figure 5.5 illustrates the audible RPM ranges for the five considered propulsion orders in ELPOT_150 Nm test case. Similar conclusions can be drawn for the ELPOT_150 Nm load case, with an additional observation of order 40 being perceivable at lower RPM ranges under this particular load case.

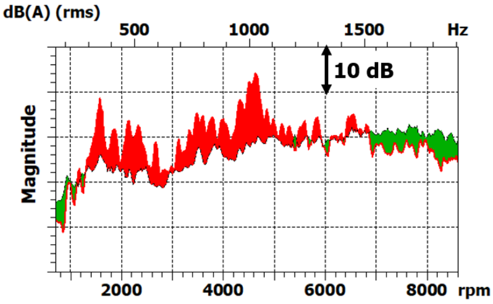

(a) Order 13.3

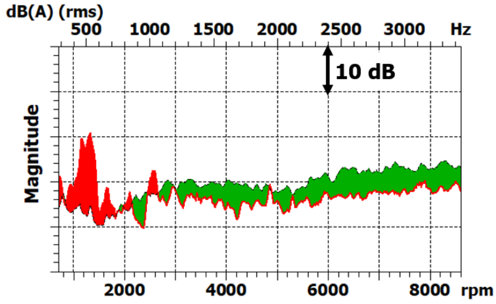

(b) Order 24

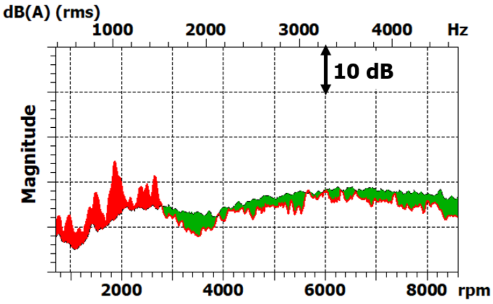

(c) Order 32.8

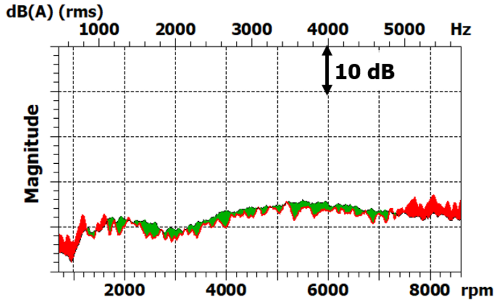

(d) Order 40

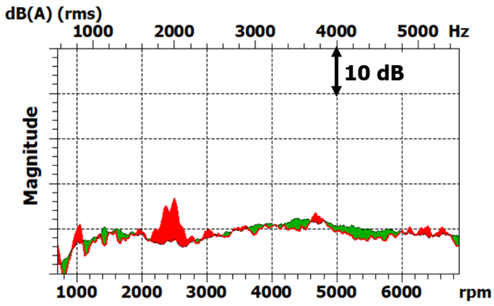

(e) Order 48

Figure 5.5: Plot highlighting the audible RPM ranges for the five propulsion orders within the test vehicle in ELPOT_150 Nm load case.

Figure 5.6 illustrates the audible RPM ranges associated with the five propulsion-related orders in ELPOT_35% PEDAL test case. It can be observed that orders 24 and 40 are most likely to be non-perceivable in this specific operational condition inside the vehicle. Also, in contrast to previous two load cases, order 32.8 can be observed to be the most dominantly perceived order in ELPOT_35% PEDAL load case.

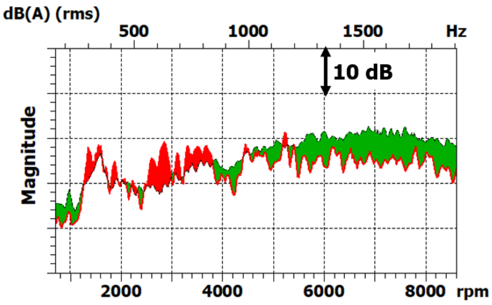

(a) Order 13.3

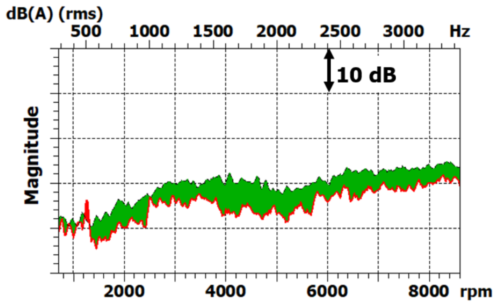

(b) Order 24

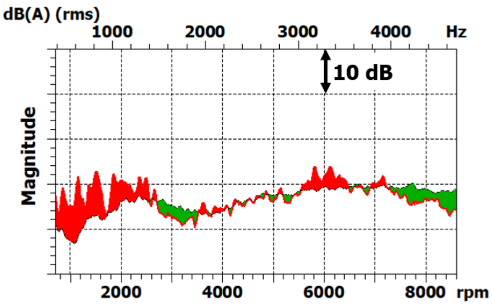

(c) Order 32.8

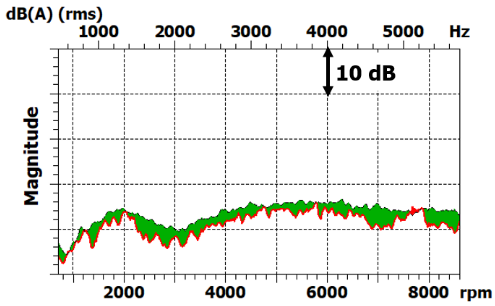

(d) Order 40

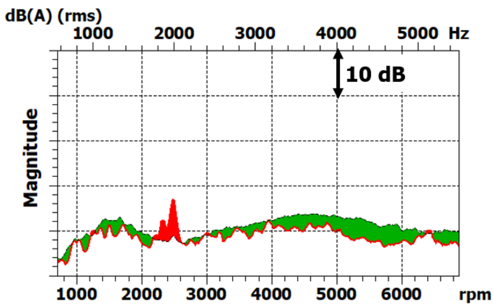

(e) Order 48

Figure 5.6: Plot highlighting the audible RPM ranges for the five propulsion orders within the test vehicle in ELPOT_35% PEDAL load case.

Figure 5.7 illustrates the audible RPM ranges associated with the propulsion orders in REGEN load case. Again, orders 24 and 32.8 can be considered to be the most dominant order in REGEN test case, with order 40 being non-perceivable across the RPM.

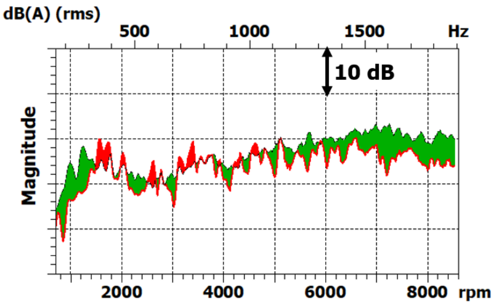

(a) Order 13.3

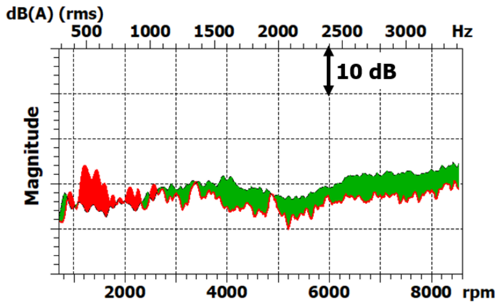

(b) Order 24

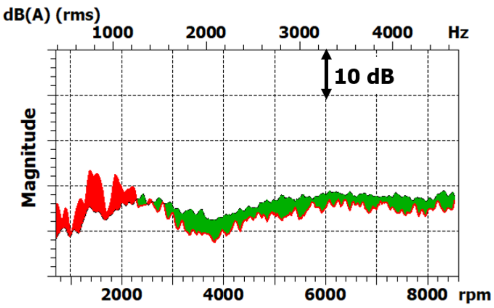

(c) Order 32.8

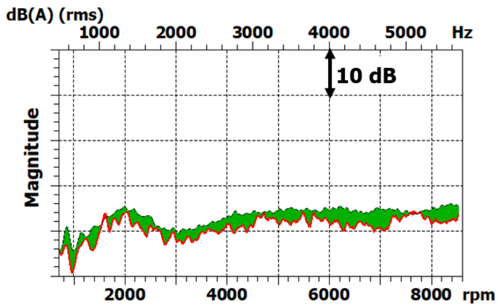

(d) Order 40

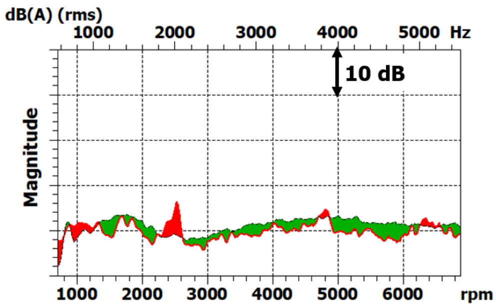

(e) Order 48

Figure 5.7: Plot highlighting the audible RPM ranges for the five propulsion orders within the test vehicle in REGEN load case.

In such a manner, the RPM ranges where the considered five propulsion orders were most likely to be perceived inside the test vehicle for all the four measured load cases were selected. The study, therefore, guided the OTPA investigations to be centered around the aim of mitigating the propulsion-related NVH concerns, hence, highlighted.

5.2 OTPA Strategy

In order to study noise and vibration propagation through various transfer paths, it was first essential to set up an accurate Path-Receiver model for the complete vehicle. This means that not only the inclusion of all coherent transfer paths has to be cared for, an effort to minimize any over-estimation for any transfer path should be made. Furthermore, the interface between the source and the body has to be judiciously defined in order to formulate a proper Path-Receiver based OTPA model. This section discusses an iterative approach undertaken within the research work for formulating a detailed Path-Receiver model for the tested prototype vehicle. Several combinations of the instrumented sensors over the vehicle were analysed and their estimated synthesized responses were compared with the actual operational data in order to check the overall over-estimation or under-estimation up to 5 kHz.

To estimate the synthesis from the considered reference DOFs within each iteration, i.e., with each Path-Receiver model, the first step was to estimate the transmissibility functions using CTC. Then, the PC score was computed for each of the estimated principle component and the cumulative PC score value in percentage was checked. Figure 5.8 illustrate the PC score on a cumulative scale for one of the iterations. It can be observed that no distinction exists between the PCs beyond 94% cumulative value. The inclusion of such PCs within the transmissibilities shall lead to a degraded SNR and enhanced noise content. Hence, a decision to exclude such PCs beyond threshold cumulative value was made for all iterations.

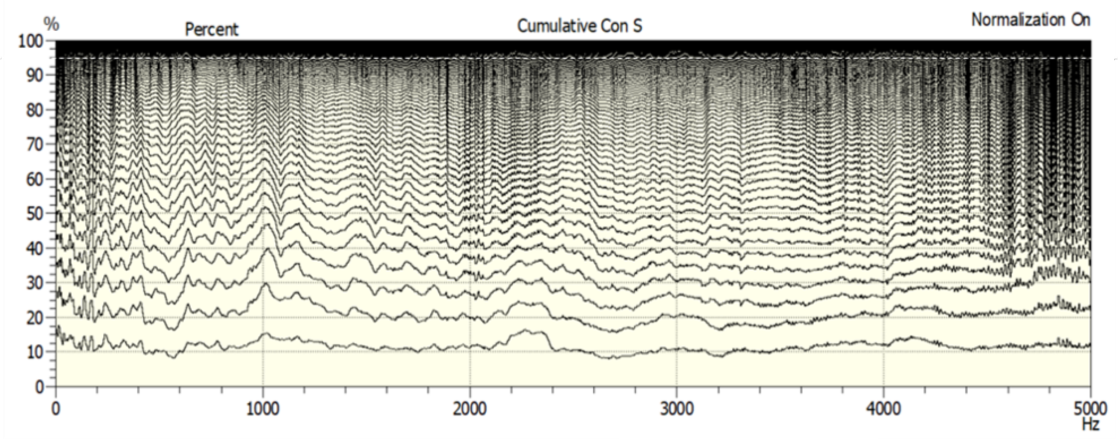

Figure 5.8: Illustration of the Cumulative PC Score up to 5 kHz for one of the analyzed Path-Receiver based OTPA model.

Upon the estimation of the transmissibility functions for the vehicle model, they can be used with any excitation matrix over the reference DOFs and the individual path contributions can be estimated. Figure 5.9 presents a typical example of the Path-Receiver network which couples reference excitations with the CTC-estimated vehicle's transmissibility functions. Excitations over each path in the excitation matrix ([X]) are convolved (time domain processing) with their respective transmissibility functions to the DEL in the CTC-estimated transmissibility matrix ([H]), which results in the individual path contributions. These can be grouped basis the type of analyses one wishes to conduct. In Figure 5.9, an attempt to distinguish between the overall air-borne and structure-borne contribution has been made by grouping all the microphones in a separate adder and all the accelerometers in a separate adder group. Ultimately, all the contributions can be added together in order to estimate the synthesized total response at the receiver position, i.e., the DEL.

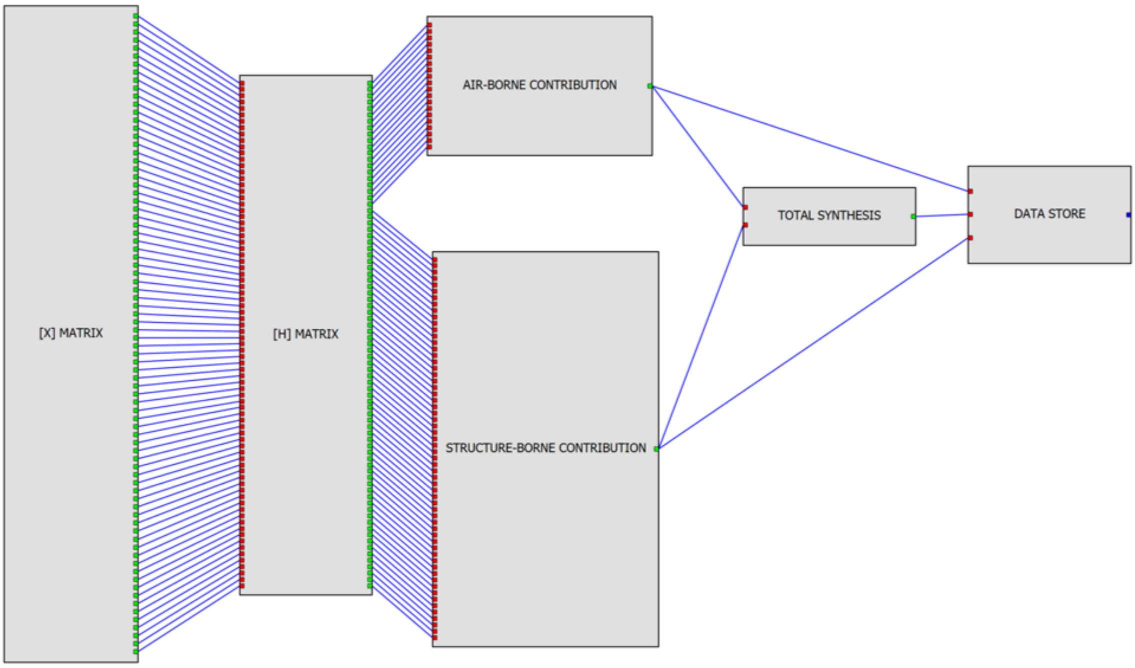

Figure 5.9: An illustration of a typical transfer Path synthesis network in OTPA to highlight the total air-borne and structure-borne contributions, as well as the total synthesized response at the receiver position.

Upon estimating the synthesized response from the defined Path-Receiver model at the DEL, a comparison of the synthesis with the measured data was made in order to define the legitimacy for different analyzed iterations. Figures 5.10 to 5.12 present a comparison between the operational data and the synthesis in ELWOT test condition for the scenario where all the instrumented sensors were considered within the Path-Receiver model, with a total of 30 structure-borne paths and 15 air-borne leakages (Model A). Again, the spatially averaged data over 4 microphones at the DEL has been compared. The APS comparison in Figure 5.10 indicates towards a decent overall correlation with respect to the captured orders and resonance in the synthesis. However, under-estimation can be observed above 3 kHz, as apparent in the comparison of the frequency average across the track parameter (RPM) in Figure 5.11. Also, Figure 5.12 presents a correlation between the measured order magnitude with the synthesised magnitude for the five critical propulsion orders. Since the presented model could correlate well with the operation data only up to 3 kHz, considerable under-estimation for higher orders above 5000 to 6000 RPM can be observed.

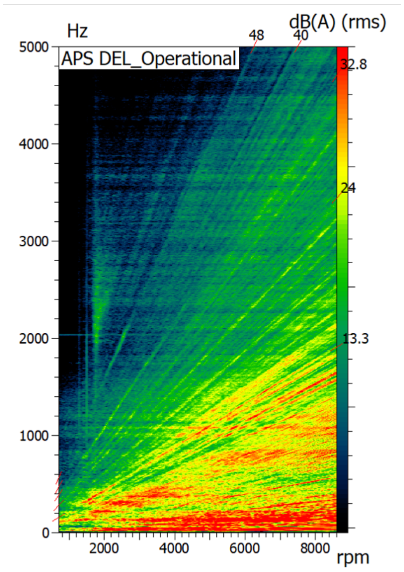

(a) DEL Operational APS

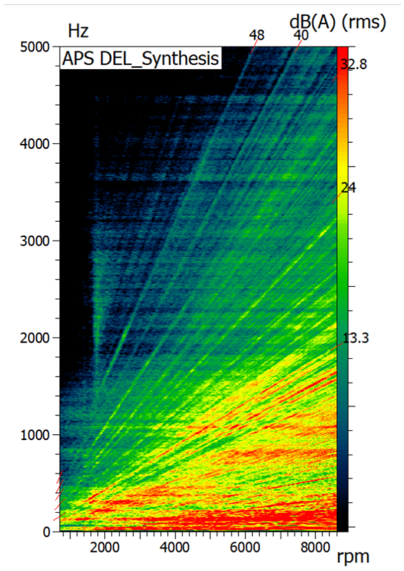

(b) DEL Synthesis APS

Figure 5.10: A comparison of the synthesized interior noise using OTPA Model A with the measurement data at the DEL. The plots compare the APS levels for the interior noise within the test vehicle in ELWOT load case.

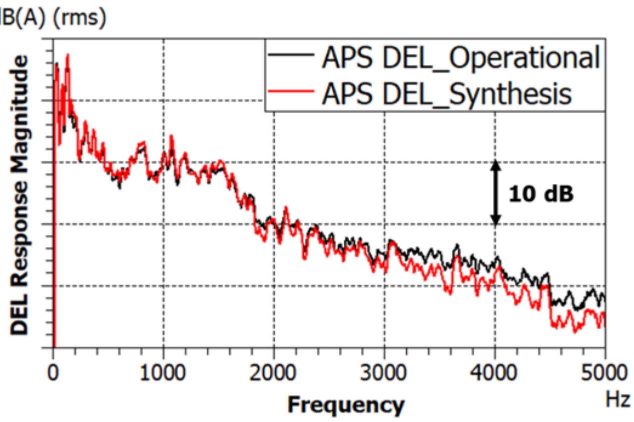

Figure 5.11: A frequency average comparison across the RPM range for the synthesized interior noise using OTPA Model A with the measurement data at the DEL in ELWOT load case.

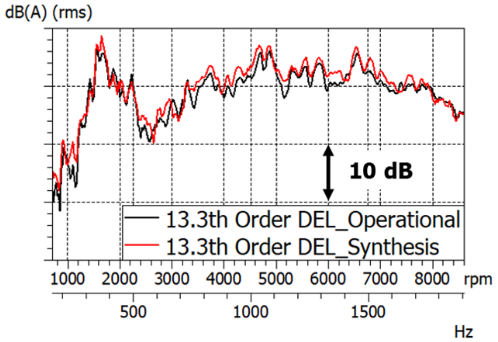

(a) Order 13.3

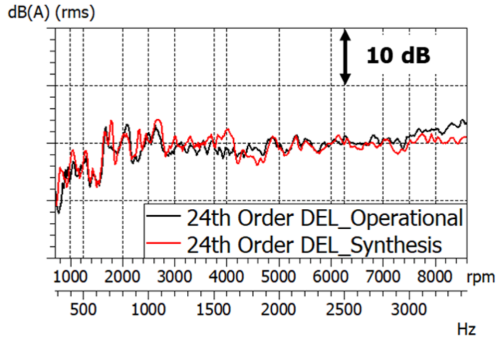

(b) Order 24

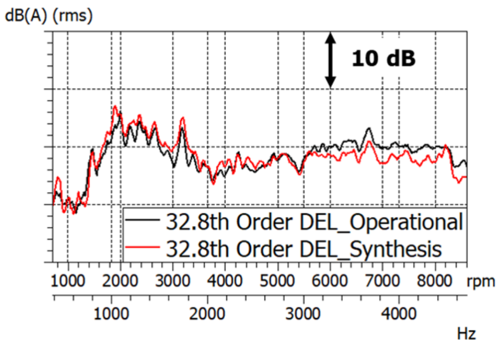

(c) Order 32.8

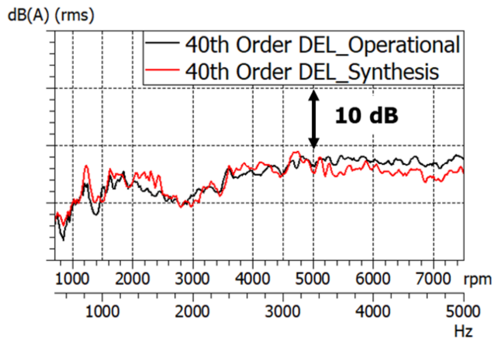

(d) Order 40

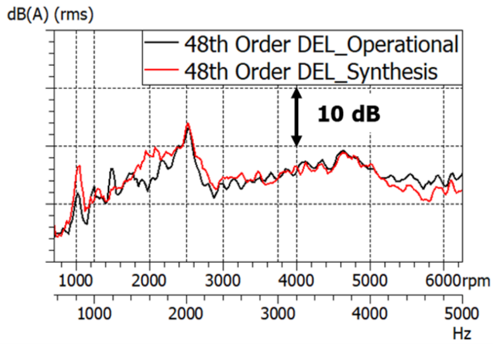

(e) Order 48

Figure 5.12: Order magnitude comparison for the synthesized interior noise using OTPA Model A with the measurement data at the DEL in ELWOT load case.

The under-estimation at higher frequencies with the above presented Path-Receiver model motivated an iterative approach for the path selection in order to enhance the correlation of the synthesized data with the operational levels. Ultimately, a Path-Receiver model with the vehicle's passive side defined from the subframe mounts to body was formulated, with Figure 5.13 illustrating the considered paths defined within the model (Model B). A total of 16 structure borne transfer paths were considered in the model (8 each on the front and rear drive units), along with the parasitic paths, i.e., two paths along the tunnel and two on the firewall. With regards to the air-borne contributions, no changes exist between Model A and B and the number of air-borne paths considered were as finalized based upon the results from the air-borne transmissibility measurements.

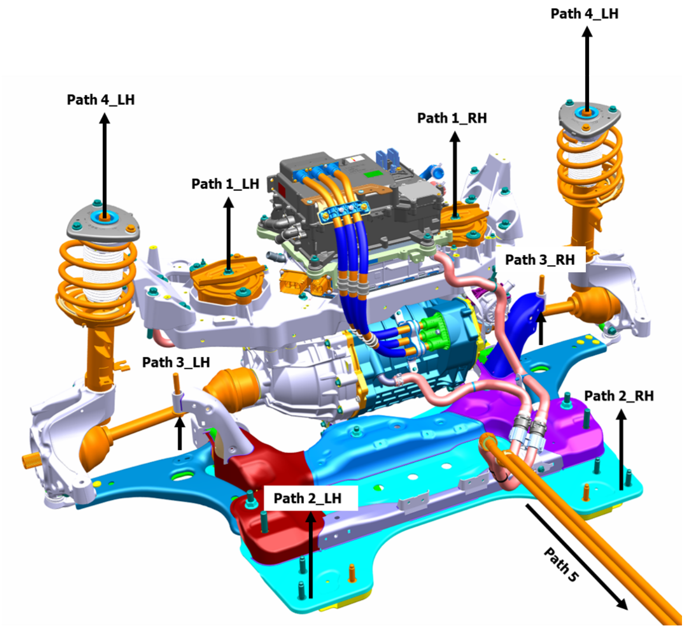

(a) EFAD - Body transfer paths

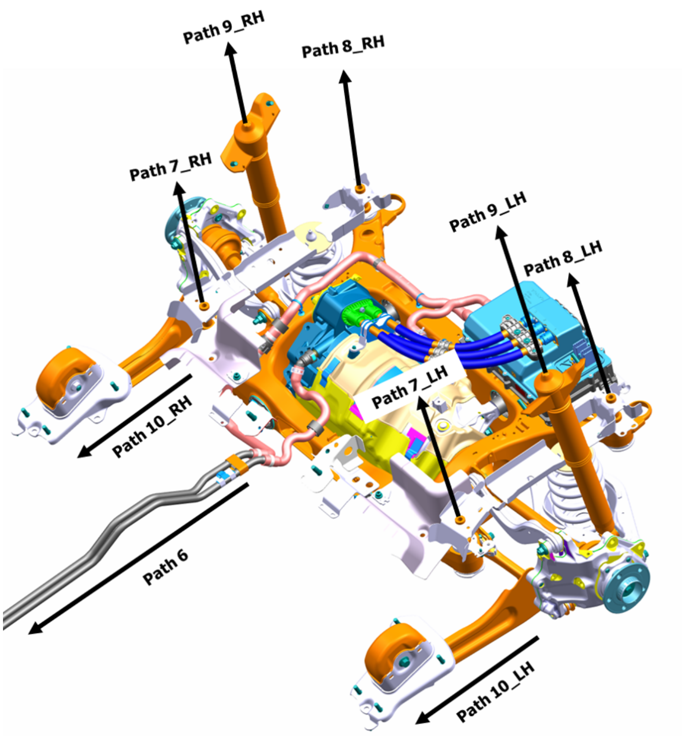

(b) ERAD - Body transfer paths

Figure 5.13: An illustration of the structure-borne transfer paths considered from the e-machines to the body within the OTPA Model B.

Figures 5.14 to 5.16 present a comparison between the operational data and the synthesized response levels in ELWOT test condition for Model B. An improved data correlation, especially at higher frequencies with respect to Model A can be observed. Further, better correlation at higher RPM for the propulsion orders can be observed with the specified Path-Receiver model, with an over-estimation in 1600 RPM to 3000 RPM for order 48.

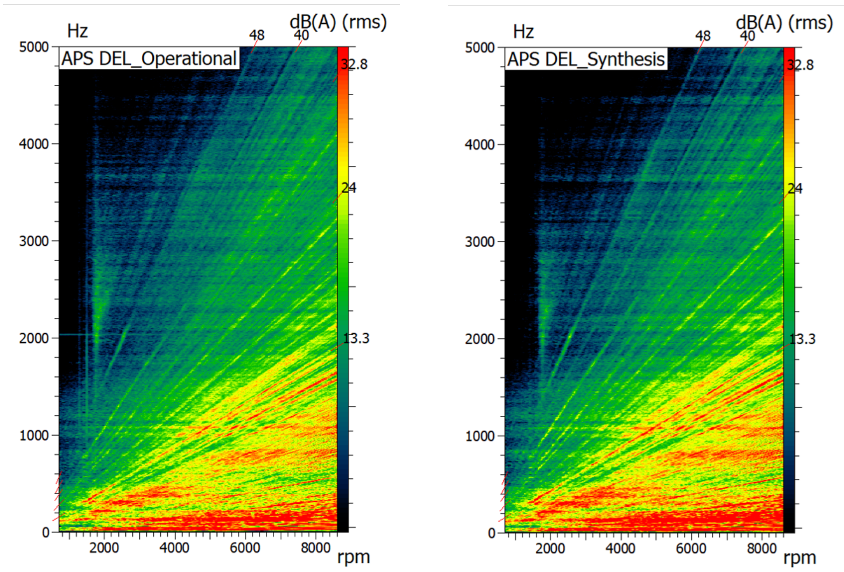

(a) DEL Operational APS **(b)** DEL Synthesis APS

Figure 5.14: A comparison of the synthesized interior noise using OTPA Model B with the measurement data at the DEL. The plots compare the APS levels for the interior noise within the test vehicle in ELWOT load case.

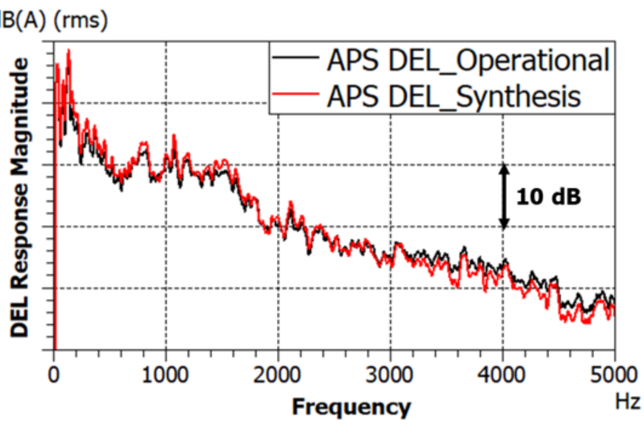

Figure 5.15: A frequency average comparison across the RPM range for the synthesized interior noise using OTPA Model B with the measurement data at the DEL in ELWOT load case.

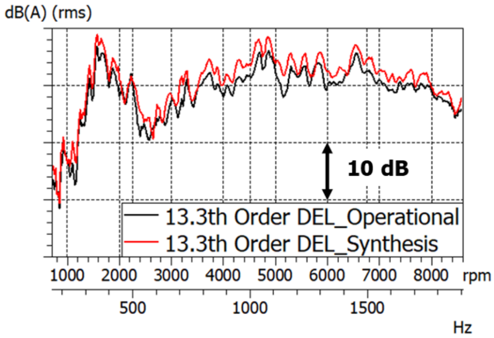

(a) Order 13.3.

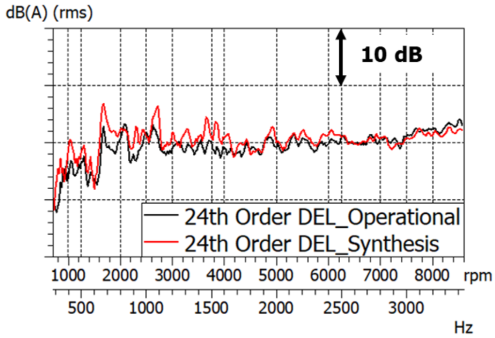

(b) Order 24.

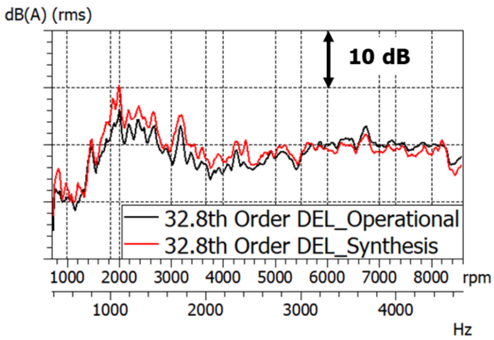

(c) Order 32.8.

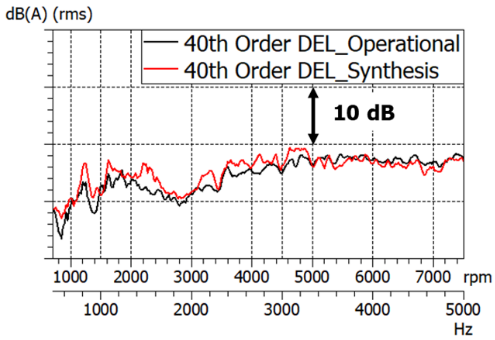

(d) Order 40.

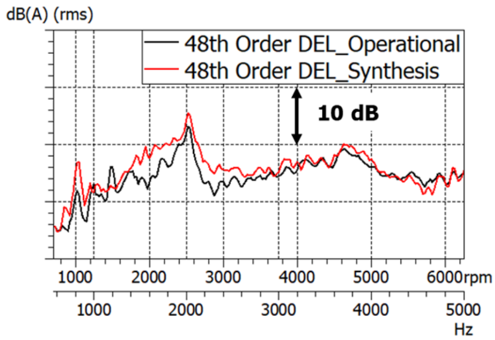

(e) Order 48.

Figure 5.16: Order magnitude comparison for the synthesized interior noise using OTPA Model B with the measurement data at the DEL in ELWOT load case.

Similar conclusions were drawn upon comparing Model B's total synthesis output with the measured data for three other load cases. Hence, Model B was finalized for further investigation with regards to path localization for the earlier highlighted propulsion-related challenges over the test vehicle. Further, an attempt to study the distinction between the air-borne and structure-borne contributions was also made. The details of all the considered transfer paths (reference DOFs) within the chosen model can be looked upon in Table A.4.

6
Results

On the basis of the enhanced degree of correlation between the synthesized and the operational data at the response position achieved with the OTPA-based Path-Receiver Model B, a deep dive into the model was carried out in order to highlight the critical transfer paths responsible for high frequency noise propagation in the tested prototype vehicle. To restate, the deep dive was performed only in selected RPM ranges where the order-related whine character was observed to be likely audible in different load cases, as was detailed in Figures 5.4 to 5.7. First, an attempt to highlight the dominance of the source sub-systems, i.e, EFAD and ERAD for each of the considered propulsion-related order was made. Next, a detailed path investigation was conducted in order to highlight the critical transfer paths responsible for the possible whine perception inside the test vehicle. In addition, an investigation was conducted in order to highlight high frequency structure-borne transfer through the parasitic paths considered within the OTPA model. To conclude, an attempt to distinguish between the structure-borne propagation and air-borne leakages in frequency domain was made upon considering all the load cases and the analyzed propulsion orders.

6.1 Source Ranking

Prior to the path-based investigation for every possible audibility associated with the five propulsion orders, an overall investigation was conducted in order to rank the dominance of NVH propagation from EFAD and ERAD towards the interior noise levels in the tested prototype vehicle.

6.1.1 Order 13.3

Figure 6.1 illustrates the overall decomposition of the synthesized order magnitude into the total contribution levels from the EFAD and ERAD units for the transmission-related order 13.3. The total contribution from EFAD was estimated upon the summation of all path contributions (structure-borne propagation and air-borne leakages) considered around the EFAD unit, while the total ERAD contribution was estimated upon the summation of all path contributions considered around the ERAD unit. The comparison clearly highlights a mixed trend in contributions from the EFAD and ERAD units in ELWOT and ELPOT_150 Nm load cases up to 5000 RPM to 6000 RPM. EFAD dominance can be observed at higher RPM ranges. Further, ERAD dominance can be observed in lower to mid-range

RPM up to 5000 RPM to 6000 RPM for the ELPOT_35% PEDAL and REGEN load cases.

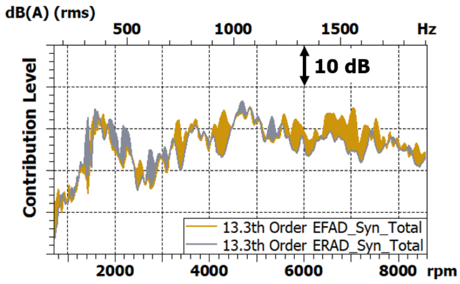

(a) ELWOT

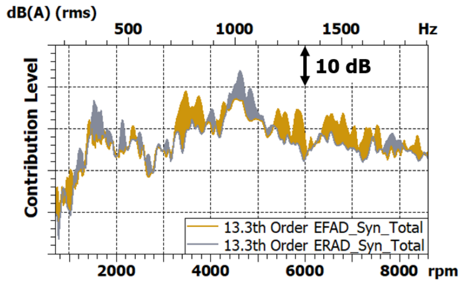

(b) ELPOT_150 Nm

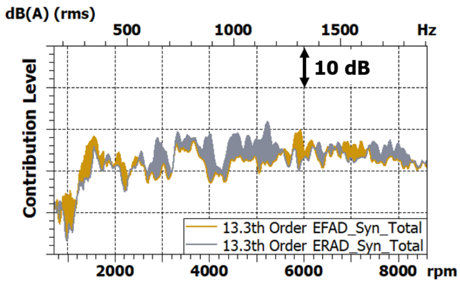

(c) ELPOT_35% PEDAL

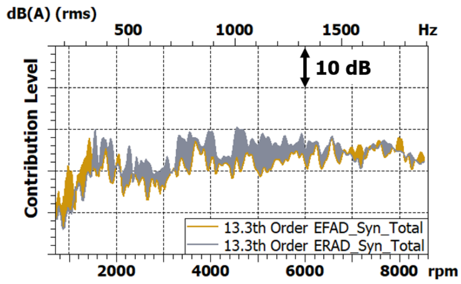

(d) REGEN

Figure 6.1: Magnitude comparison of the total contributions from the EFAD and ERAD units towards the DEL noise order 13.3 within the test vehicle in four distinct load cases.

6.1.2 Order 24

Figure 6.2 illustrates the overall decomposition of the synthesized order magnitude at the DEL into the total contribution levels from the EFAD and ERAD units for order 24 related to the e-machine. The resonances at 0.5 kHz and 1.95 kHz can be observed to be EFAD dominant, whereas the peaks in the frequency range from 0.8 kHz to 1.1 kHz can be observed to be dominated by the ERAD contributions. Mixed contributions can be observed from both the EFAD and ERAD units towards the total response level above 5000 RPM, i.e., at higher frequencies above 2 kHz.

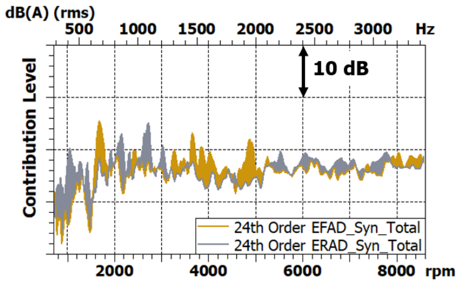

(a) ELWOT

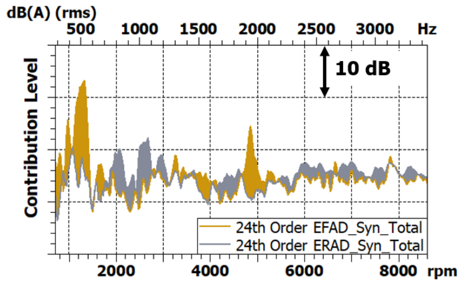

(b) ELPOT_150 Nm

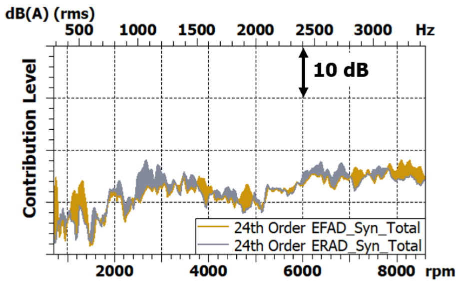

(c) ELPOT_35% PEDAL

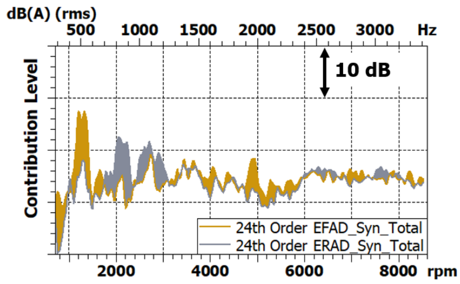

(d) REGEN

Figure 6.2: Magnitude comparison of the total contributions from the EFAD and ERAD units towards the DEL noise order 24 within the test vehicle in four distinct load cases.

6.1.3 Order 32.8

Figure 6.3 illustrates the overall decomposition of the synthesized order magnitude into the total EFAD and total ERAD contributions for order 32.8 related to the transmission system within the test vehicle. The comparison signifies a clear dominance of the EFAD contributions towards the overall synthesized DEL response across the spectrum, with an exception at 1.1 kHz, the resonance at which can be seen to be ERAD dominated. This resonance from the ERAD unit can be observed to be captured within the ELWOT, ELPOT_150 Nm and REGEN measurements.

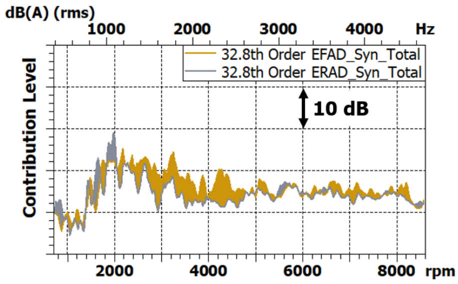

(a) ELWOT

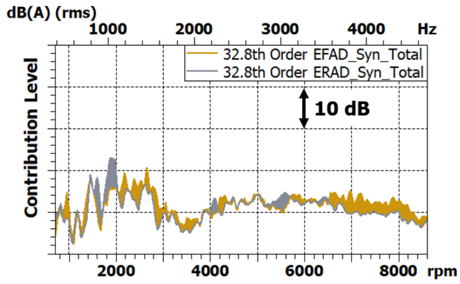

(b) ELPOT_150 Nm

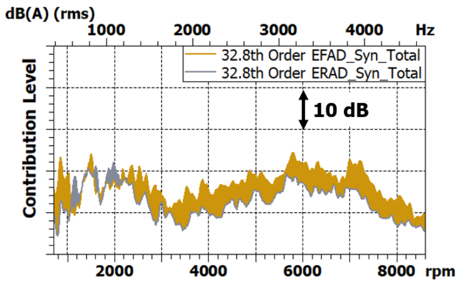

(c) ELPOT_35% PEDAL

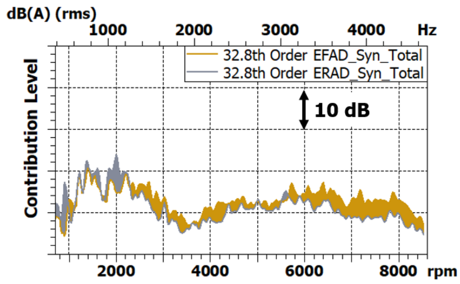

(d) REGEN

Figure 6.3: Magnitude comparison of the total contributions from the EFAD and ERAD units towards the DEL noise order 32.8 within the test vehicle in four distinct load cases.

6.1.4 Order 40

Figure 6.4 illustrates the overall decomposition of the synthesized order magnitude into the total EFAD and total ERAD contributions for the electric motor-related order 40. An overall dominance by the EFAD contributions towards the DEL response can be observed in all the four load cases. Additionally, slight dominance from the ERAD contributions can be observed for the ELWOT and ELPOT_150 Nm test cases below 2000 RPM.

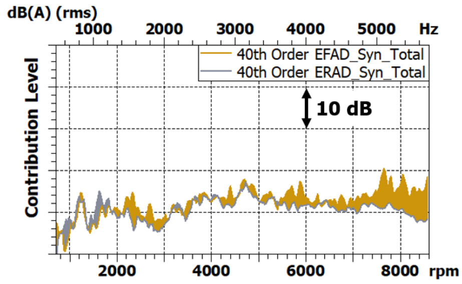

(a) ELWOT

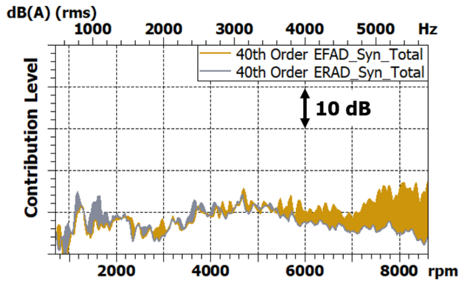

(b) ELPOT_150 Nm

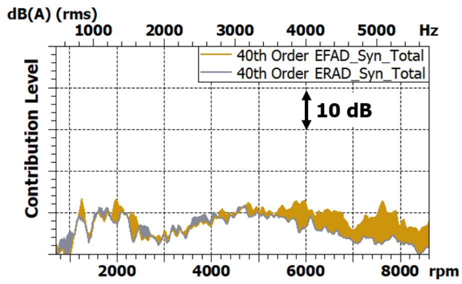

(c) ELPOT_35% PEDAL

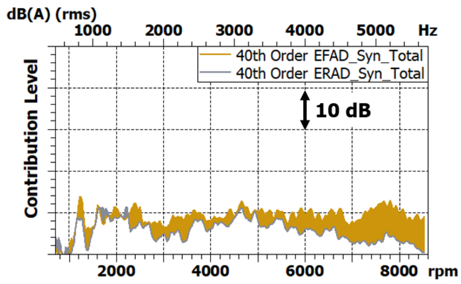

(d) REGEN

Figure 6.4: Magnitude comparison of the total contributions from the EFAD and ERAD units towards the DEL noise order 40 within the test vehicle in four distinct load cases.

6.1.5 Order 48

Figure 6.5 illustrates the overall decomposition of the synthesized order magnitude over the DEL into the total EFAD and total ERAD contributions for the electric motor-related order 48. A mixed trend in contribution levels can be observed from the EFAD and ERAD units in lower to mid-range RPM ranges. However, the resonance peaks at 0.8 kHz, 2 kHz and 3.9 kHz can be observed to be distinctly dominated by the EFAD unit. Additionally, EFAD dominance can be observed above 5000 RPM, i.e., at higher frequencies.

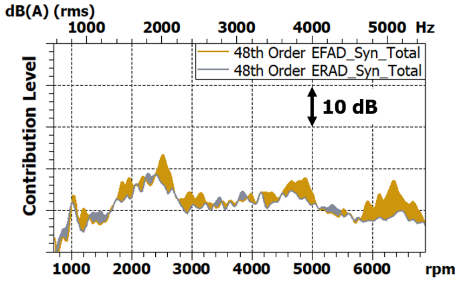

(a) ELWOT

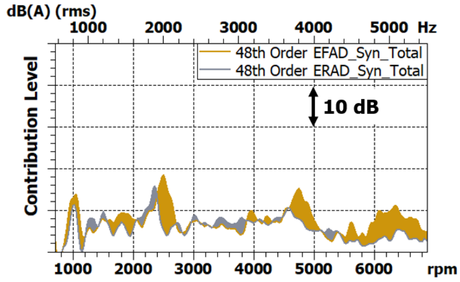

(b) ELPOT_150 Nm

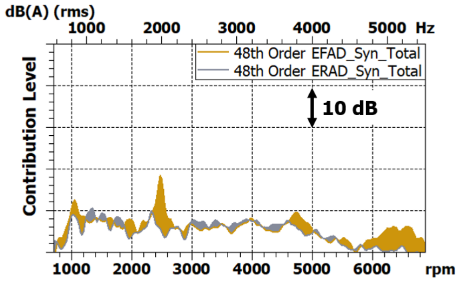

(c) ELPOT_35% PEDAL

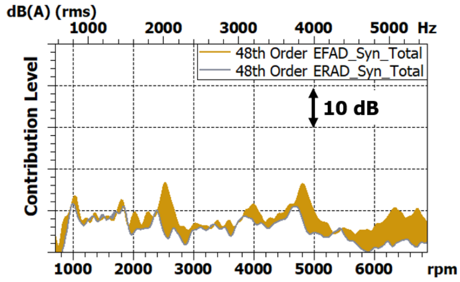

(d) REGEN

Figure 6.5: Magnitude comparison of the total contributions from the EFAD and ERAD units towards the DEL noise order 48 within the test vehicle in four distinct load cases.

The above comparison provided an overview about the contributions from the EFAD and ERAD units towards the interior noise levels within the test vehicle. Overall, an equal contribution from the EFAD and ERAD units was observed in lower to mid-range RPMs, whereas EFAD contributions were observed to dominate the interior noise levels at higher RPMs. In frequency domain, noise propagation at lower frequencies below 0.5 kHz was dominated by both the EFAD and ERAD units. Further, a mixed trend of EFAD and ERAD contribution was observed in the frequency ranges of 0.5 kHz to 1 kHz and 2 kHz to 3 kHz, with slight dominance by the EFAD contributions in all load cases except ELPOT_150 Nm. An ERAD dominant resonance phenomena can be localized at 1 kHz since the peak occurs for almost all the order magnitudes, with ERAD being the dominant contributor. EFAD dominance can be concluded, in general, above 1 kHz.

6.2 Path Ranking

The study presented below details the outcomes from the OTPA-based path localization conducted over the most likely audible RPM ranges for each of the considered propulsion orders. The selection of audible RPM ranges in terms of whine perception inside the test vehicle is based upon the investigation as presented in the Analysis chapter of the report. The study further aims at proposing a methodological workflow in order to perform path ranking over the order-based concerns by utilizing OTPA as a trouble-shooting tool.

6.2.1 Order 13.3

Based on the equation 2.1.1, it can be stated that the maximum frequency presence for order 13.3 when the electric motor RPM is restricted up to 8700 RPM (which is the maximum tested RPM of the EFAD/ERAD on the test vehicle when it was swept up to 130 kph during the OTPA measurements) is up to 2 kHz. Hence, order 13.3 can be rightly supposed to either excite or be perceivable in lower to mid-frequency ranges. With reference to Figures 5.4a, 5.5a, 5.6a and 5.7a, it can be concluded that order 13.3 is most likely to be audible in ELPOT_150 Nm load case. Hence, it was logical to study the transfer paths for order 13.3 in this particular load case. A detailed transfer path synthesis network was formulated to estimate how much of the contribution was dominated from EFAD and ERAD units. Further, individual path contributions were compared and the critical paths responsible for the whine perception associated with order 13.3 inside the test vehicle were highlighted in ELPOT_150 Nm load case.

Figure 6.6 presents the OTPA outcomes for order 13.3 in ELPOT_150 Nm load case. The investigation was conducted over the Path-Receiver model as discussed earlier in the report (Figure 5.13). First, the audible RPM ranges with respect to the synthesized order magnitude were highlighted for detailed analysis. Then, the synthesis was decomposed into the total contributions from the EFAD and ERAD units towards the interior noise at DEL. Next, EFAD and ERAD contributions were further decomposed into their total air-borne and structure-borne contributions. Finally, the individual path contribution levels for each of the reference DOF were relatively compared across the audible RPM range and the paths with the maximum contribution levels were accentuated.

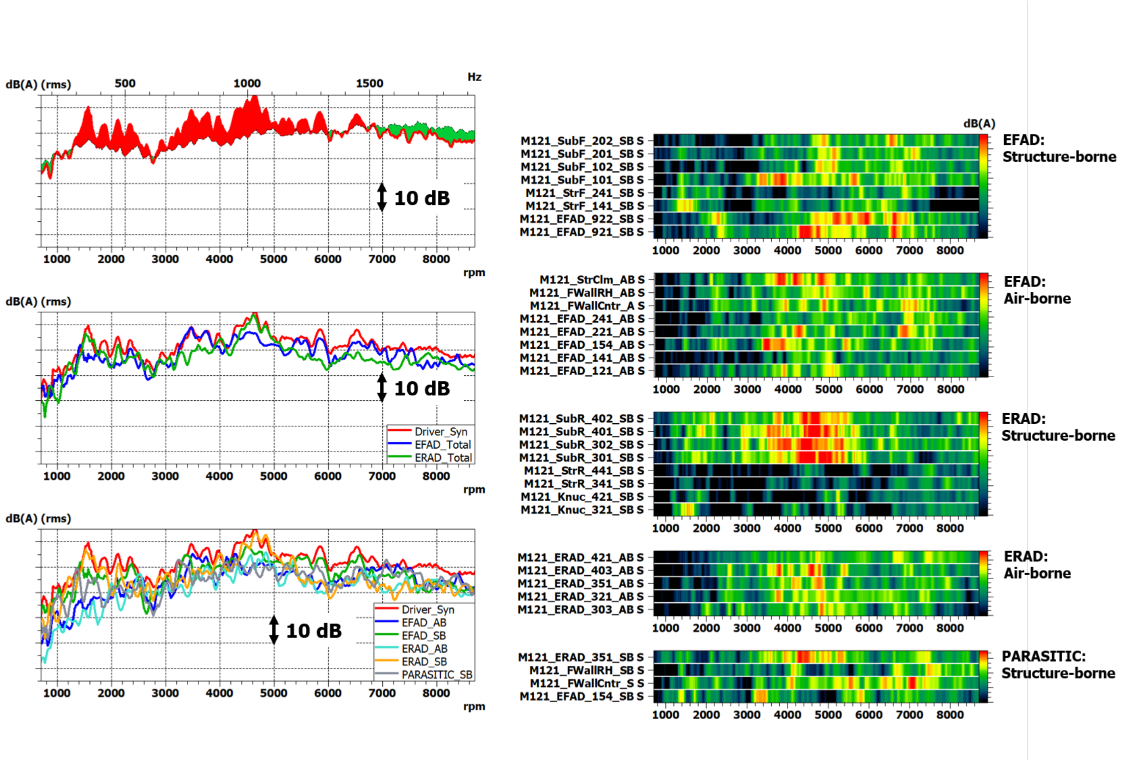

Figure 6.6: An illustration of the path localization results over the test vehicle for order 13.3 in ELPOT_150 Nm load case.

The audible RPM range for order 13.3 in ELPOT_150 Nm load case have been highlighted as the red region in the top-left graph, and the path ranking was conducted in this RPM range. It can be observed that the order magnitude peaks below 3000 RPM are equally dominated by both the EFAD and ERAD units. Further, the structure-borne propagation can be observed from both the EDUs. Upon referring to the channel overview (order magnitude) presented for the individual contributions from each path in the specified RPM range, it can be concluded that the strut mount towards LH is the main contributor at the front, with the rear suspension's longitudinal rods on LH being the main contributor at the rear. Some contribution from the rear subframe mounts can also be observed, especially from its front LH mount to the body side-rails. However, it can be seen that the top mounts do not show any significant contribution at the front. This turned suspect towards structure-borne propagation from the drive shafts to suspensions links, and hence, the vibration data at the front and rear knuckles was analysed in order to confirm this path as the major contributor.

Figure 6.7 compares the APS levels for the knuckle vibration velocity in ELPOT_150 Nm test case over four knuckles up to 2 kHz. A resonance at around 280 Hz to 390 Hz can be observed in almost all the knuckle positions. However, the resonance can be seen to interact with the order 13.3 and amplify its magnitude over the front and rear knuckles only on LH, with its amplification being the maximum at the front knuckle position from 300 Hz to 380 Hz and at the rear from 560 Hz to 610 Hz. This confirms the transfer path from the drive shaft to the body via suspension links on the LH to be structure-borne dominant below 3000 RPM.

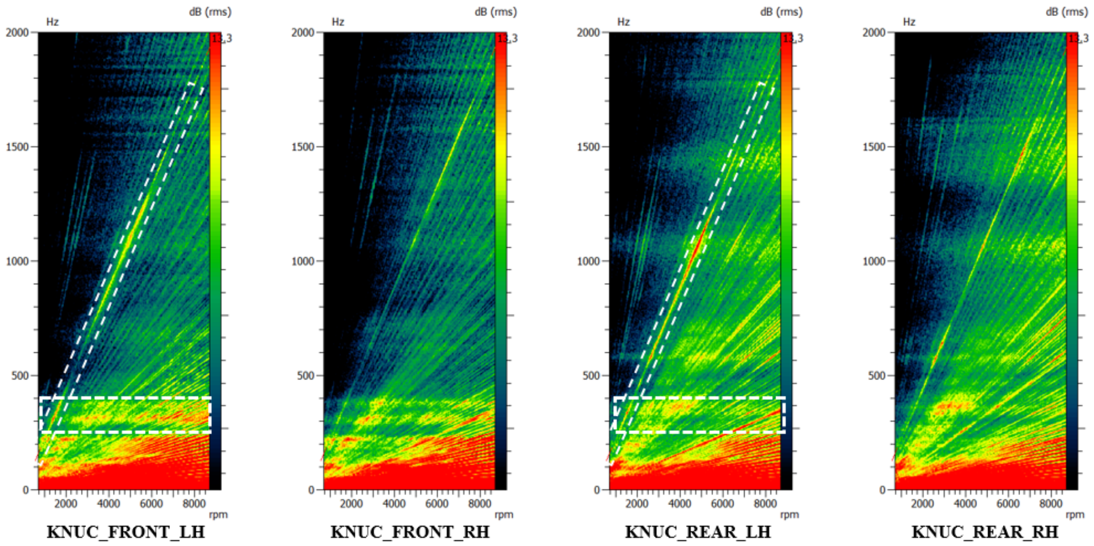

Figure 6.7: An APS comparison for the vibration velocity at four knuckle positions over the test vehicle in ELPOT_150 Nm load case.

In a similar manner, an attempt to highlight the dominant transfer paths for other peaks was made. The peaks in 3000 RPM to 4000 RPM range (665 Hz - 890 Hz) can be observed to be air-borne dominant, with dominant transfer paths detected to be the front tunnel and the firewall-steering column interface. ERAD dominance can be observed in the RPM range from 4000 RPM to 5000 RPM (900 Hz - 1100 Hz), with structure-borne propagation prevailing from the rear subframe mounts to the rear body side-rails. Parasitic vibration transfer via rear tunnel into the body can also be observed in 4200 RPM to 4500 RPM. Further, EFAD dominant structure-borne propagation can be observed above 5000 RPM (above 1.1 kHz), with the major transfer path highlighted to be front RH top mounts via front subframe (C-mount on LH and rear body mount on RH) to the body.

6.2.2 Order 24

With reference to Figures 5.4b, 5.5b, 5.6b and 5.7b, it can be inferred that the whine perception associated with order 24 is most likely to be audible inside the test vehicle in ELPOT_150 Nm load case, specifically in the RPM range of 1000 RPM to 2000 RPM. Hence, path ranking was conducted for order 24 over this particular load case in the specified RPM range. Similar to the previous study, Figure 6.8 illustrates the OTPA results from the path-receiver based investigation over the dominant peak for order 24 in 850 RPM - 1500 RPM range.

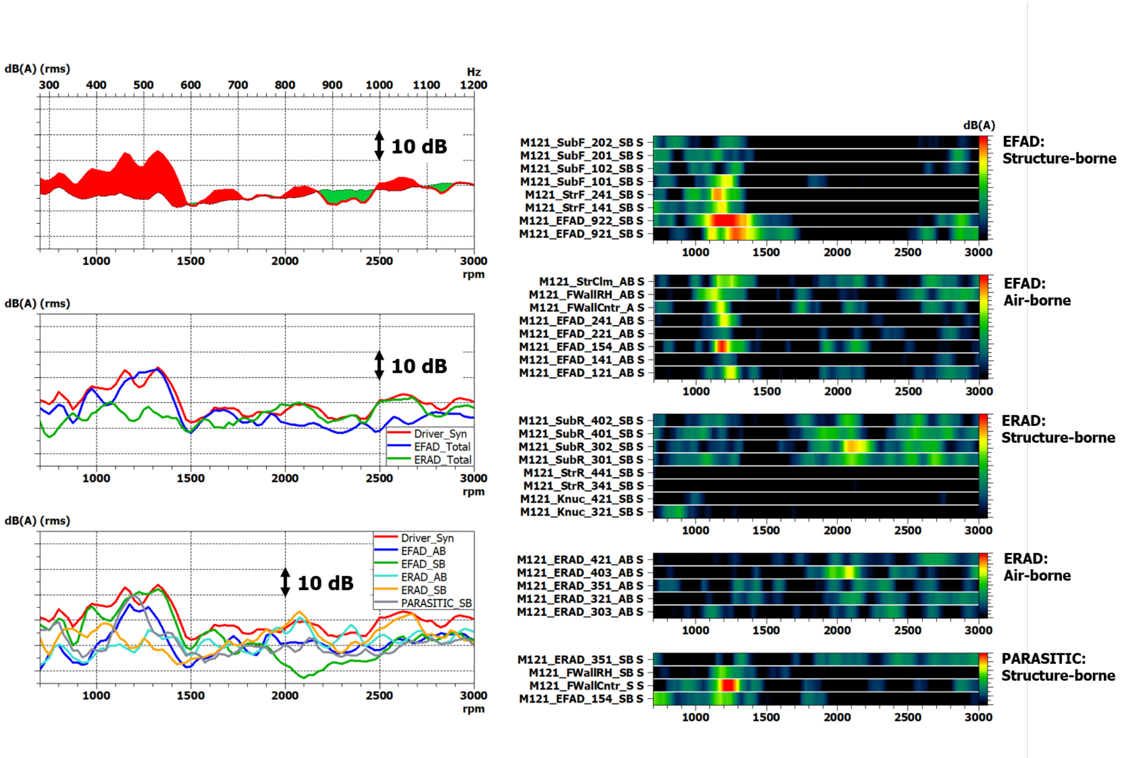

Figure 6.8: An illustration of path localization results over the test vehicle for order 24 in ELPOT_150 Nm load case.

It can be observed that the peaks in the RPM range from 850 RPM to 1500 RPM are EFAD dominant. In addition, mixed trend in contributions from the air-borne leakages and the structure-borne transfer paths can be noticed. Upon referring to the channel overview of the order magnitude for each of the individual path contributions towards the response at DEL, the path from the front top mount on the RH to the body can be highlighted. The vibration transfer can also be detected at the strut mount on the RH. Further, the front tunnel opening to the EFAD unit can also be seen to be an air-borne leakage, leading to an enhanced order magnitude in the specified RPM range. Further, parasitic presence at the firewall centre location in terms of structure-borne vibration can be highlighted.

6.2.3 Order 32.8

Upon referring to Figures 5.4c, 5.5c, 5.6c and 5.7c, it can be observed that the whine perception associated with the transmission-related order 32.8 is most likely to be audible inside the vehicle in the ELWOT load case, precisely below 4000 RPM. Hence, path ranking was conducted for order 32.8 over the ELWOT load case. Figure 6.9 presents the OTPA results from the path-receiver based investigation over the dominant peaks for order 32.8 below 4000 RPM range.

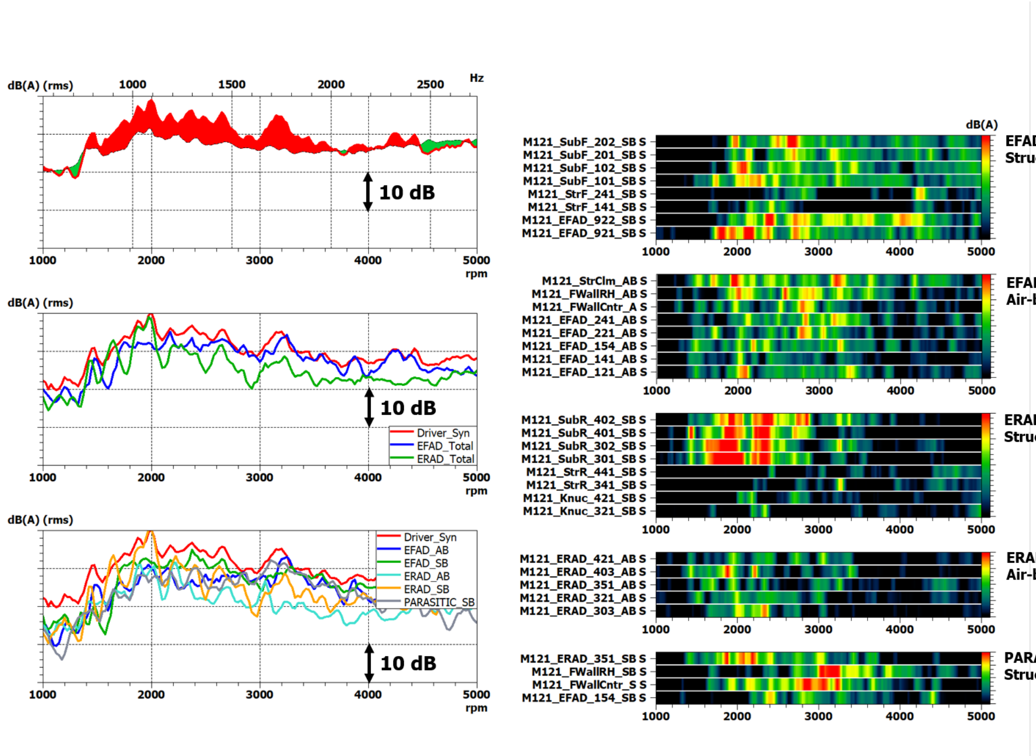

Figure 6.9: An illustration of path localization results over the test vehicle for order 32.8 in ELWOT load case.

Total structure-borne propagation from ERAD constitutes the major contribution at the response levels in 1000 RPM to 2000 RPM range, localized to rear subframe mounts over the rear body side-rails, primarily via LH mounts. Mixed structure-borne contributions from the EFAD and ERAD can be observed in 2000 RPM - 2500 RPM range, with major contributions from the rear subframe mounts (front mounts) towards the rear and top mounts (LH and RH) towards the front. At the mid-range to higher RPM ranges, distinct EFAD contribution can be observed from 2500 RPM onwards, which is dominated by both the air-borne leakages and structure-borne transfer paths. The higher end contributions in RPM from EFAD can also be observed to be dominated by both the air-borne leakages and structure-borne propagation, with the structure-borne transfer localized to the front top mounts and the vibration being transmitted to the body via the rear right subframe mount to body, and the air-borne leakages localized across the firewall via steering column - firewall interface, cabin harness network - firewall interface and the firewall centre. Moreover, parasitic transmission can be detected at the firewall centre location.

6.2.4 Order 40

Referring to Figures 5.4d, 5.5d, 5.6d, and 5.7d, it can be concluded that the whine perception linked to order 40 is most likely to be audible inside the test vehicle only in the ELPOT_150 Nm test case. Hence, path ranking was conducted for order 40 over the ELPOT_150 Nm load case. Figure 6.10 illustrates the OTPA results from the path-receiver based investigation done over the dominant peaks for order 40 below 2000 RPM.

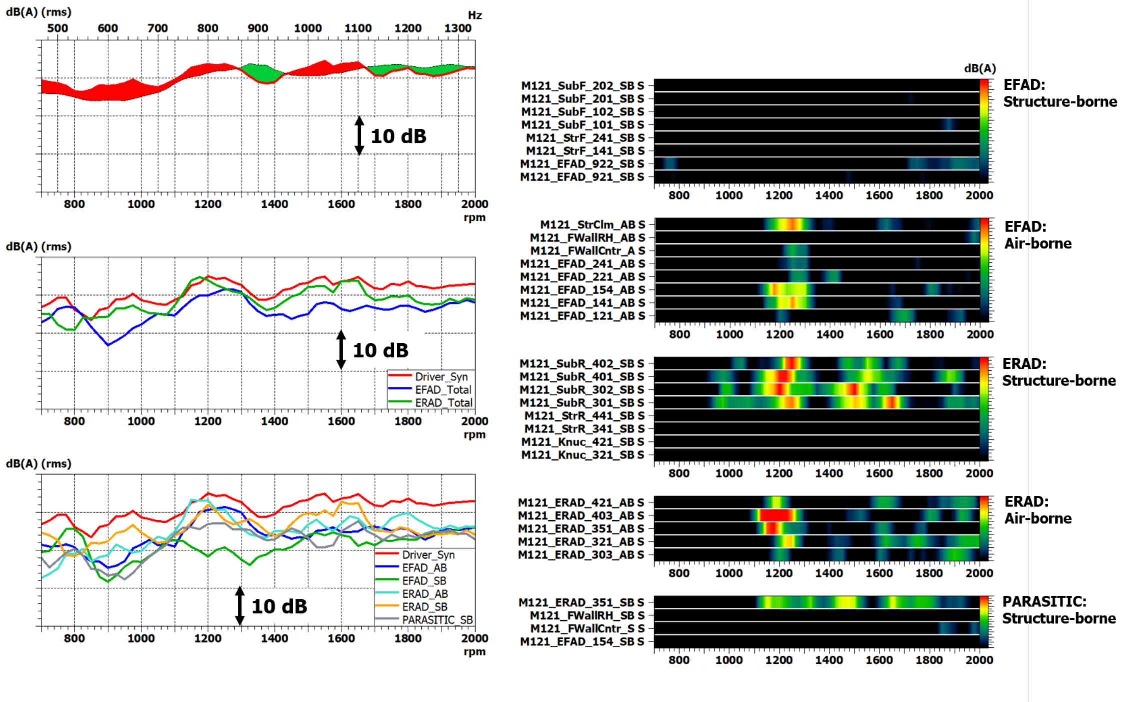

Figure 6.10: An illustration of path localization results over the test vehicle for order 40 in ELPOT_150 Nm load case.

It can be observed that the overall contributions towards the synthesized interior noise level are majorly dominated by the ERAD contributions. Further, mixed contributions from the overall synthesized air-borne and structure-borne contributions can be observed. The rear subframe mounts over the rear body side-rails can be highlighted as the major vibration transfer paths, whereas air-borne leakage can be detected at the rear side-rail location and the rear tunnel opening to the ERAD unit. Additionally, slight contributions from EFAD in terms of air-borne leakages have also been detected across the firewall and the front tunnel locations.

6.2.5 Order 48

Upon referring to Figures 5.4e, 5.5e, 5.6e and 5.7e, it can be observed that the whine perception associated with order 48 is most likely to be audible in the ELWOT load case, specifically in the RPM range of 2000 RPM to 3000 RPM. Hence, path ranking was conducted for order 48 in the ELWOT load case. Similar to the previously mentioned studies, Figure 6.11 illustrates the OTPA results from the path-receiver based investigation over the dominant peaks for order 48, i.e., for the peak at 2500 RPM.

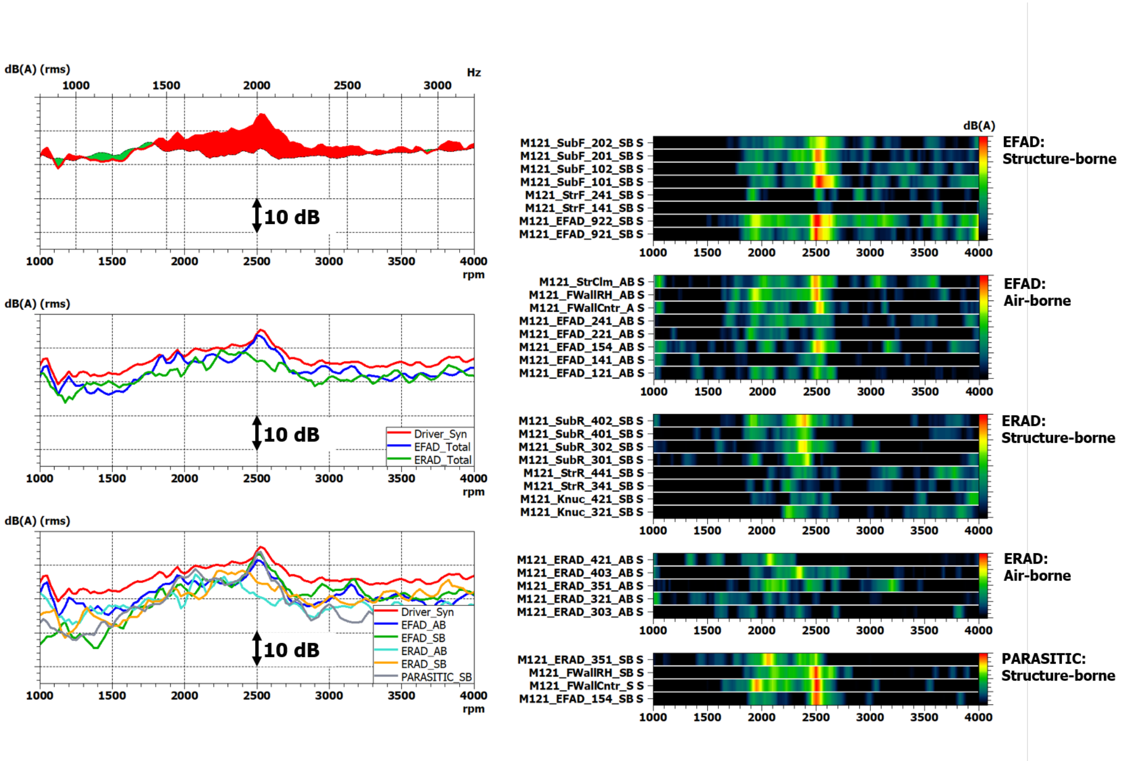

Figure 6.11: An illustration of path localization results over the test vehicle for order 48 in ELWOT test case.

It can be observed that the peak at 2550 RPM is EFAD dominant, with mixed contributions from the air-borne leakages and structure-borne transfer paths. In addition, enhanced parasitic presence can also be observed. Upon comparing the individual path contributions, it is apparent that the most dominant vibration transfer path is from the front top mounts (both LH and RH) via subframe mounts (C-Mount and front subframe's rear mount on LH) to the body. Further, the dominant air-borne leakages include leakages across the firewall, i.e., the steering column - firewall interface and the cabin harness network - firewall interface, as well as via front tunnel opening to the EFAD unit. In addition, parasitic vibration propagation can be observed at the firewall locations, which might be an indication of structure-borne radiation from the firewall unit inside the cabin. Front tunnel floor vibration transfer was another parasitic propagation detected as a contributor for order 48.

6.3 Outlook

The above explained case studies for each of the propulsion orders present an example of a detailed OTPA-based investigative approach aiming to highlight critical transfer path information on a complete vehicle level. The formulated Path-Receiver model, hence, proved to be effective in its utilization as an efficient trouble-shooting tool to gain insights over the critical transfer paths for NVH challenges associated with the propulsion whine character. Basis the methodology explained in the presented case studies, similar study was conducted for each audible peak associated with the analyzed propulsion-related orders in all the measured load cases. Critical path information for all five propulsion orders was hence gathered and the most dominant air-borne leakages and structure-borne transfer paths were identified over the test vehicle. Parasitic presence in the form of structure-borne propagation was also highlighted. The critical path information was documented and was provided as a reference to be used for further NVH refinement over the tested prototype vehicle.

The path ranking data estimated for various order-based challenges in the tested prototype vehicle can be summarized in order to gain insights about the general behaviour behind NVH propagation in EVs. For instance, Figure 6.12 presents a distribution of path contributions from the EFAD and ERAD units basis the magnitude of audibility for all the measured load cases in frequency domain. Upon an overview, it can be concluded that most audibility occurs at lower frequencies below 1500 Hz. Lower audibility can be observed at higher frequencies. Further, EFAD dominance can be observed at higher frequencies.

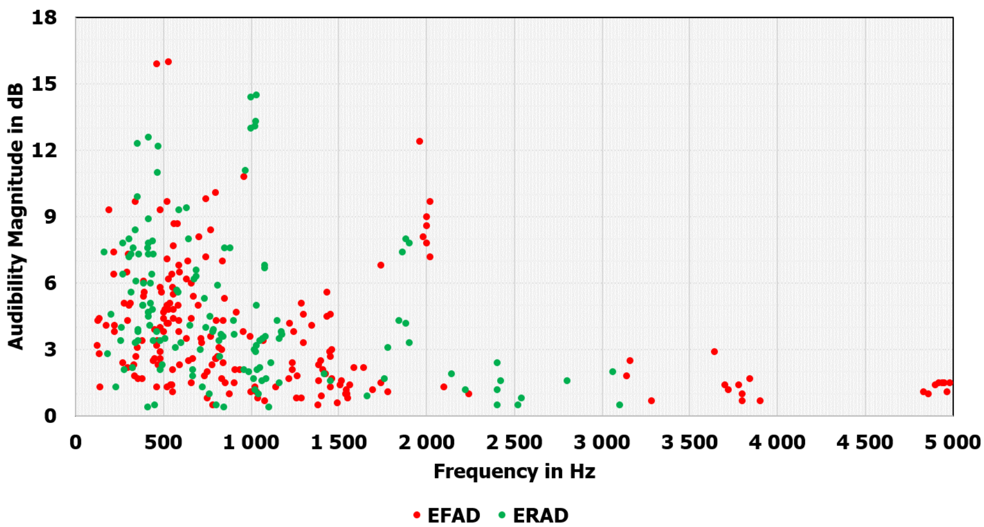

Figure 6.12: Summary of propulsion dominance towards the interior noise level in the test vehicle for all four load cases. The plot illustrates the spread of EFAD and ERAD dominance in terms of audibility across frequency.

6.4 Air-borne v/s Structure-borne Distinction

In order to develop an understanding about a distinction in frequency domain with respect to NVH propagation inside EVs, the synthesized response level at the receiver position was decomposed into total contributions from the air-borne leakages and the total contributions form structure-borne transfer. Figures 6.13a to 6.13d present the decomposition of the total synthesis into air-borne and structure-borne contributions for four distinct load cases. The decomposition has been presented as an averaged frequency spectrum across the RPM range.

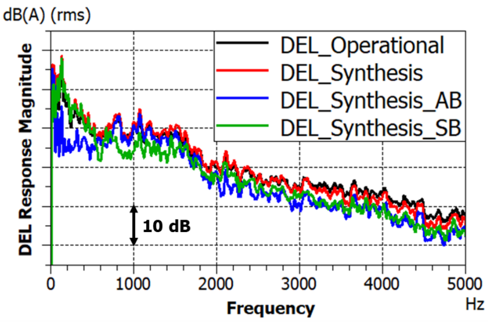

(a) ELWOT

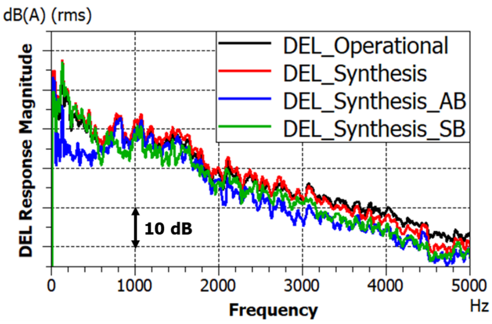

(b) ELPOT_150 Nm

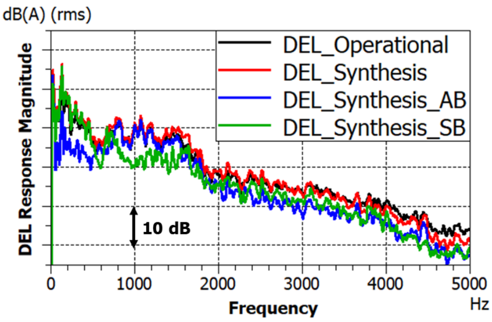

(c) ELPOT_35% PEDAL

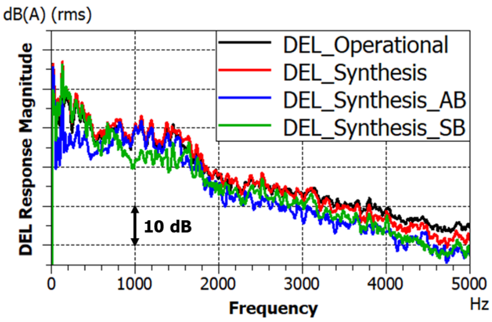

(d) REGEN

Figure 6.13: A comparison between the total air-borne and structure-borne contributions towards the interior noise level inside the test vehicle in frequency domain for four load cases.

Upon observing the distinction in contribution levels for all the load cases at lower frequencies below 600 Hz, it can be observed that structure-borne dominance prevails, which was rightly expected. This low frequency structure-borne dominance can also be observed to be most distinct in the ELPOT_150 Nm load case. Further, dominance towards the interior noise levels from the air-borne contributions can be observed in mid-frequencies from 600 Hz to 1.6 kHz, with the distinction being major in case of the ELPOT_35% PEDAL load case. However, a mixed trend can be observed among the total air-borne and structure-borne contributions at higher frequencies above 1.6 kHz. The structure-borne contributions can be observed to peculiarly reveal enhanced presence at higher frequencies for all the four load cases, with the contribution magnitude almost equal when compared to the air-borne contributions. In addition, a decomposition of total EFAD and ERAD contributions in Figure 6.12 results in Figure 6.14, where a distribution of air-borne and structure-borne contributions from the EFAD and ERAD units with regards to perception has been presented in frequency domain. It can be observed that the structure-borne contributions are present at higher frequencies, especially from the EFAD unit.

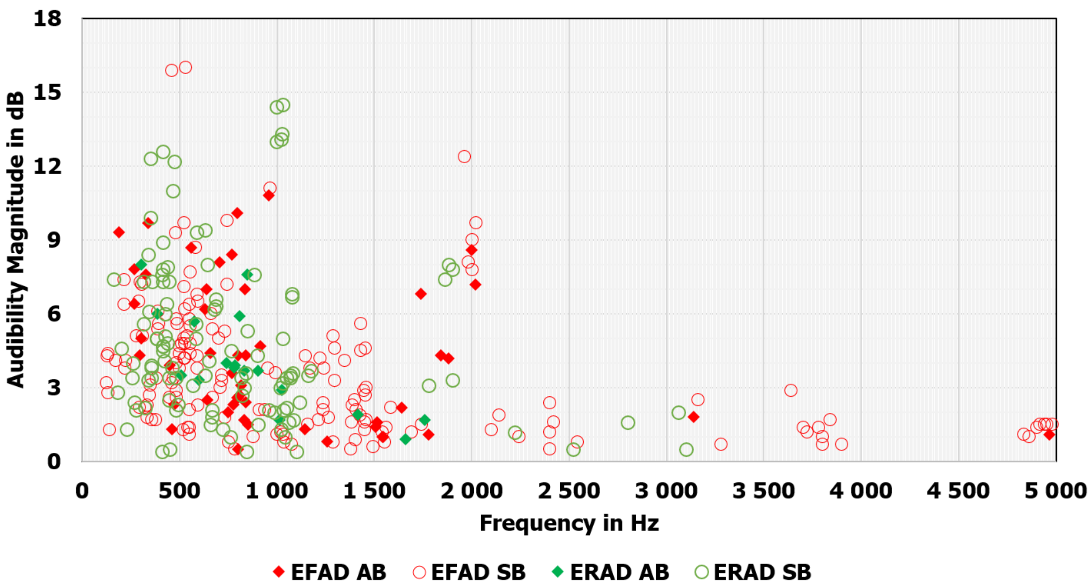

Figure 6.14: Summary of propulsion dominance towards the interior noise level inside the test vehicle for all four load cases. The plot illustrates the spread of air-borne and structure-borne contributions from the EFAD and ERAD in terms of audibility across frequency.

The distinction with respect to the air-borne and structure-borne contributions in frequency domain is well researched in conventional ICE vehicles. However, the enhanced high frequency structure-borne presence as observed in Figure 6.13 might either be characteristic to the NVH propagation in EVs, or can be a result of the limitation of the established OTPA model to accurately define a distinction between the air-borne and structure-borne contributions in frequency domain. This can be confirmed upon conducting FRF measurements in order to estimate the Noise Transfer Functions (NTFs) and the Acoustic Transfer Functions (ATFs), which shall correspond to the structure-borne transfer and air-borne leakage respectively. Another possibility can be the inability of the established OTPA model to accurately distinguish between the structure-borne and air-borne contributions, since the current methodology focused on path ranking and revolved around the instrumentation of air-borne leakages across the vehicle. To confirm this, an OTPA investigation can be conducted with the air-borne reference DOFs instrumented along the near-field of the source sub-systems, i.e., around the EFAD and ERAD units, and the structure-borne reference DOFs instrumented immediately around the EDU mounts to the subframe and body. Hence, it would be worthwhile to see if such an investigation reveals similar trend for the structure-borne and air-borne contributions in frequency domain or not. In any case, the current study shows that the established OTPA-based Path-Receiver model is unable to provide a clear distinction in frequency domain at higher frequencies between the structure-borne and the air-borne contributions towards the interior noise levels in an EV.

7

Validation

In order to validate the formulated OTPA model to confirm the path ranking results acquired from the established Path-Receiver model, it was essential to conduct validation studies at the later stages of the thesis work. An obvious validation could have been the verification measurements on a complete-vehicle level with modifications made over the earlier highlighted critical transfer paths for a particular load case. These modifications could have been either the deployment of damping pads, stiffeners or mass in case of structure-borne transfer paths, or blockages in case of air-borne leakages. However, such measurements could have been time consuming, which was not feasible within the tight schedule of the thesis work. Instead, a few alternative approaches were adopted in order to verify the established OTPA model.

Theoretically, the complete-vehicle transmissibility functions estimated using a distinct set of path excitations can be coupled with any excitation over the considered transfer paths to predict the response at the receiver positions. This rightly fulfills the general essence of TPA as a response prediction tool even without performing any physical testing. Hence, a particular ELPOT excitation was selected which was not considered earlier for transmissibility estimation within the CTC algorithm. Upon comparison of the measured interior noise at the DEL in the specific ELPOT load case with the synthesis predicted by coupling its path excitations with the earlier estimated vehicular transmissibilty functions, a conclusion over the health of the formulated OTPA-based Path-Receiver model was made [26]. It is to be noted that such predictions are expected to work only for realistic load cases, which means that there should generally be no expectation from the OTPA-estimated transmissibility matrix to predict non-linearities arising due to soft mount progressions, etc.

Another approach adopted to verify the formulated OTPA model considered the FWD and RWD measurements. For scenarios where either one of the ERAD or the EFAD was observed to be the dominant contributor towards the propulsion noise propagation, the interior noise at DEL was analysed in the FWD and RWD measurements respectively. Upon the observation of significant reduction in interior noise levels within the test vehicle in FWD or RWD measurements for such scenarios, the legitimacy over the path ranking information revealed from the formulated Path-Receiver model can be well and truly established. It is to be noted that such validation approach should strictly include only low torque measurements, so as to prevent soft mounts from going into progression during FWD/RWD measurements. Hence, ELPOT (and not ELWOT) load cases were used to compare AWD and FWD/RWD configurations for validating OTPA outcomes using this approach.

7.1 Response Prediction with Random Excitation Matrix

Since the ELPOT_35% Pedal load case was not considered earlier within the CTC algorithm, it was used for validation purpose in order to predict the response using the formulated OTPA model. Figures 7.1 and 7.2 illustrate a comparison between the operational and synthesized interior noise at the DEL in ELPOT_35% Pedal load case. Decent correlation can be observed between the measured noise level and the synthesis in the APS plot comparison as shown in Figure 7.1. Slight under-estimation can be observed at higher frequencies above 4 kHz and over-estimation can be observed at lower frequencies.

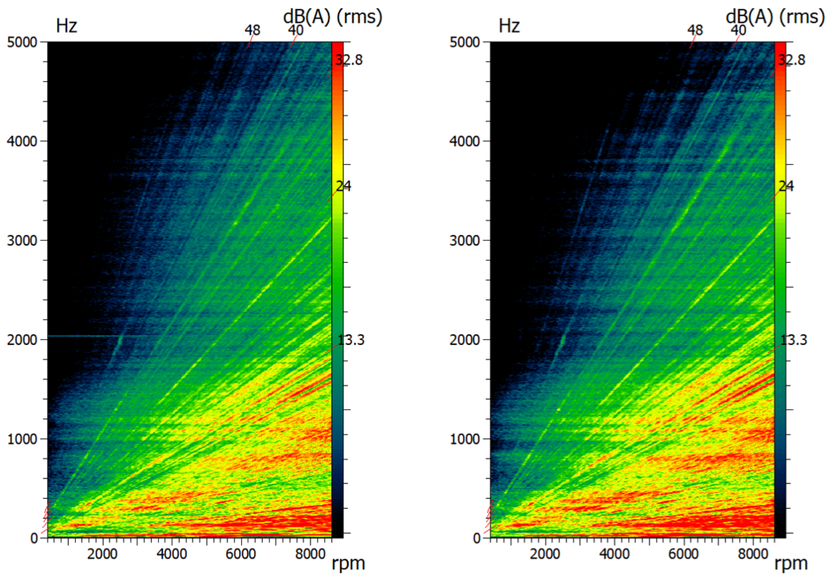

(a) DEL Operational APS **(b)** DEL Synthesis APS

Figure 7.1: APS plot comparison for the synthesized interior noise at the DEL inside the test vehicle with the measurement data in ELPOT_35% Pedal load case.

Similar conclusions can be drawn in Figure 7.2, where an averaged frequency spectrum for the interior noise levels across the RPM has been presented. The under-estimation for the synthesis with respect to the actual noise levels becomes significant only above 4 kHz and hence, it can be stated that the established Path-Receiver model is effective as a response prediction tool up to 4 kHz.

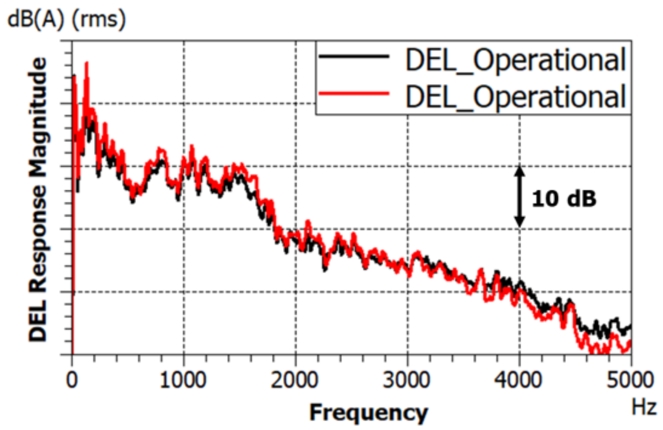

Figure 7.2: Comparison of frequency average across the RPM for the synthesized interior noise at DEL with the measurement data in ELPOT_35% Pedal load case.

Since the observations revealed upon comparison of the synthesis with the measurement data for the in ELPOT_35% Pedal test case (not included in CTC) are similar as were revealed with the ELWOT test case (included in CTC), the accuracy of the established Path-Receiver model for predicting accurate response synthesis at the receiver positions was confirmed.

7.2 Verification of ERAD Dominance using FWD Measurement

Figure 7.3 highlights the RPM regions (coloured as red) where the whine associated with the transmission-related order 13.3 is likely to be perceivable inside the test vehicle in ELPOT_100 Nm load case. It can be observed that the whine associated with order 13.3 is most likely to be audible in 4250 RPM to 5000 RPM range.

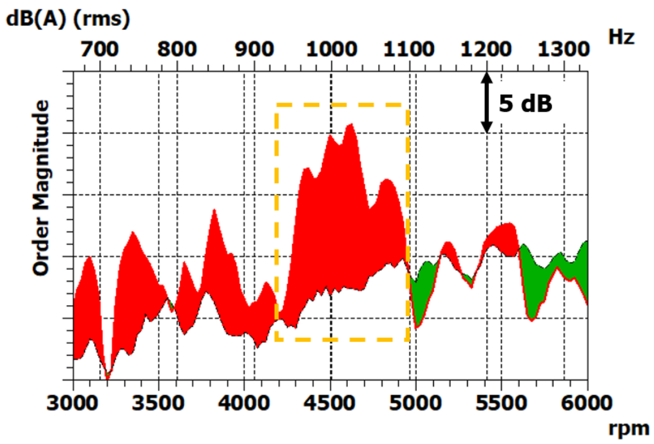

Figure 7.3: Plot highlighting the audible RPM ranges (in red) for the DEL order 13.3 in ELPOT_100 Nm load case.

The OTPA investigation highlighted ERAD to be the dominant contributor towards the specified whine audibility. Figure 7.4 illustrates the decomposition of the synthesized DEL response into the total contribution from EFAD and ERAD. The dominance of ERAD towards the synthesized response in the specified RPM range of 4250 RPM - 5000 RPM can be clearly observed.

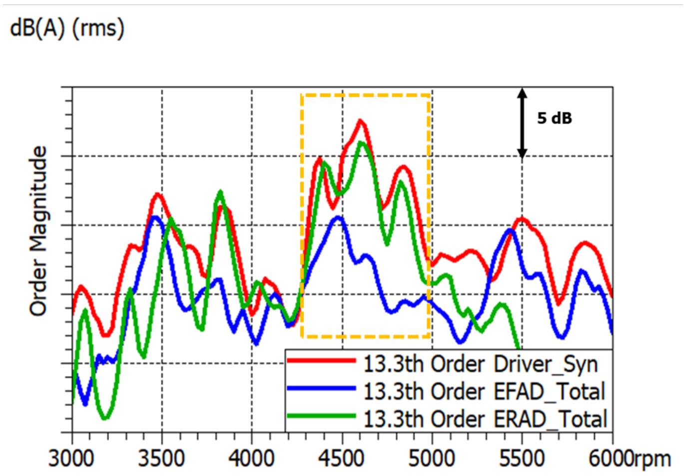

Figure 7.4: Comparison of the contributions from EFAD and ERAD towards the total synthesized DEL order 13.3 in ELPOT_100 Nm load case.

In order to validate this conclusion revealed from the established Path-Receiver model, a FWD measurement was selected, maintaining the exact torque level on EFAD as was maintained over EFAD in AWD measurement (100 Nm). Figure 7.5 presents a comparison of the magnitudes for DEL order 13.3 in AWD, FWD and RWD vehicle configurations. It can be observed that upon switching the ERAD off (FWD measurement), the order magnitude in the specified RPM range was attenuated by more than 5 dB. Further, a RWD configuration, with the same torque over ERAD as in AWD measurement, led to an insignificant drop in the order magnitude. Hence, ERAD dominance over order 13.3 in the specified RPM range for the ELPOT_100 Nm load case was justified.

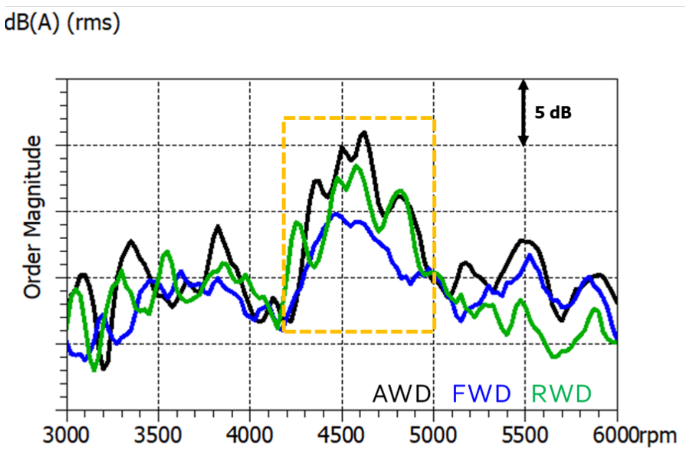

Figure 7.5: Magnitude comparison for the DEL order 13.3 in ELPOT_100 Nm load case for the AWD, FWD and RWD configurations over the test vehicle.

7.3 Verification of EFAD Dominance using RWD Measurement

Similar verification study was conducted for an EFAD dominant whine perception scenario, by using the measured interior noise levels in the RWD vehicle configuration. Figure 7.6 highlights the RPM regions (coloured as red) where the whine associated with the transmission-related order 32.8 is likely to be perceivable inside the test vehicle in ELPOT_100 Nm load case. It can be observed that the whine perception associated with order 32.8 is most likely to be audible in the RPM range of 2100 RPM to 2700 RPM.

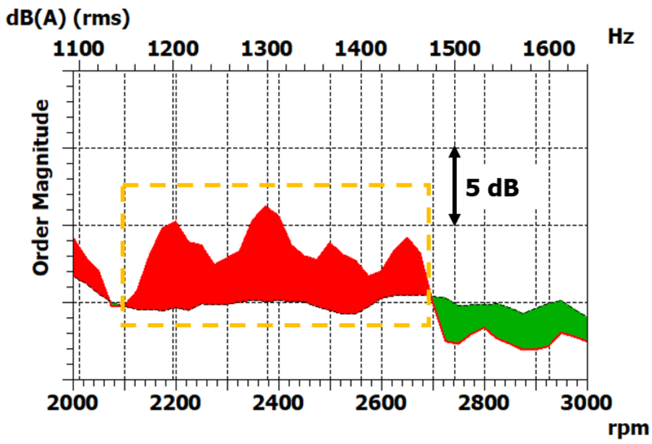

Figure 7.6: Plot highlighting the audible RPM ranges (in red) for the DEL order 32.8 in ELPOT_100 Nm load case.

The OTPA investigation revealed EFAD as the dominant contributor towards the specified whine perception. Figure 7.7 illustrates the decomposition of the total synthesized DEL response into the total contribution from EFAD and ERAD, and the dominance of EFAD towards the synthesized response in the specified RPM range of 2100 RPM - 2700 RPM can be clearly seen.

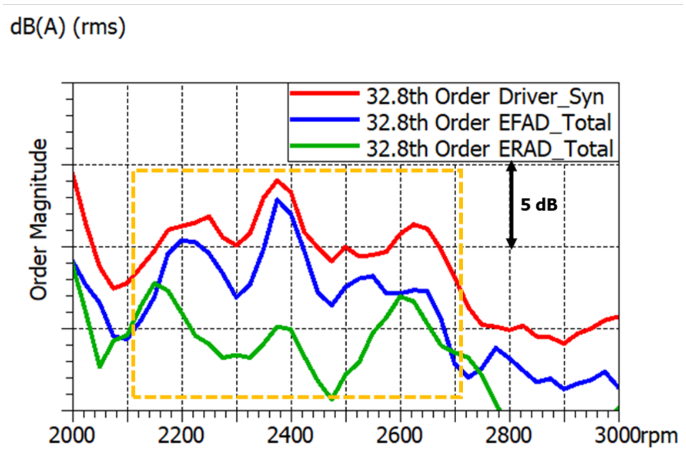

Figure 7.7: Comparison of the contributions from EFAD and ERAD towards the total synthesized DEL order 32.8 in ELPOT_100 Nm load case.

In order to validate this revelation, a RWD measurement was selected, maintaining the exact torque level on ERAD as was maintained over ERAD during the AWD measurement (100 Nm). Figure 7.8 presents a comparison of the magnitude for DEL order 32.8 in AWD, FWD and RWD configurations. It can be observed that upon switching the EFAD off (RWD measurement), the order magnitude in the specified RPM range was attenuated by almost 5 dB. Further, an FWD configuration (with same torque over EFAD as in the ELPOT_100 Nm AWD measurement) led to an insignificant change in the order magnitude. Hence, EFAD dominance over DEL order 32.8 in the specified RPM range in ELPOT_100 Nm load case was justified.

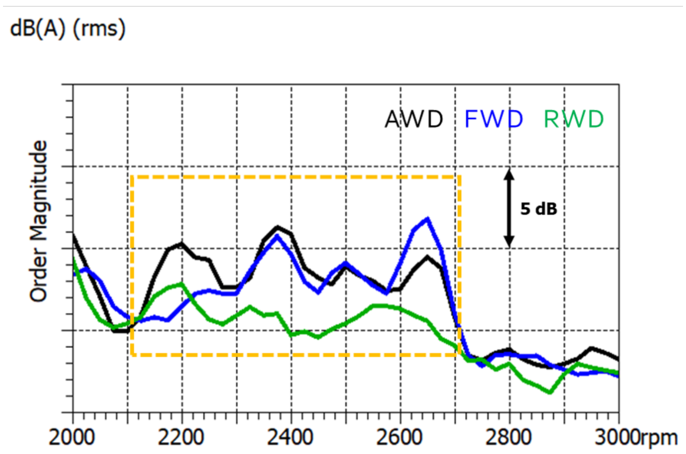

Figure 7.8: Magnitude comparison for DEL order 32.8 in ELPOT_100 Nm load case for the AWD, FWD and RWD configurations over the test vehicle.

Hence, the above discussed case studies validate the accuracy of the formulated Path-Receiver model and emphasis upon the legitimacy of its utilization not only as a response prediction tool but also for correct path ranking estimations.

8
Conclusion

The presented Master Thesis work illustrated upon the formulation of a detailed Path-Receiver model of a complete BEV using OTPA. Initially, the importance of both the structure-borne as well as air-borne propagation of vibration and noise towards high-frequency interior noise in EVs was highlighted. Then, OTPA was used to dig deeper to understand concerns related to the propagation of propulsion noise in a prototype BEV.

The study signifies the effectiveness of OTPA as a trouble-shooting tool in order to perform a qualitative path-based ranking in an EV. Since the challenges with regards to energy coherence increase in an EV, special care has to be taken while implementing OTPA as a trouble-shooting tool in order to ensure reliable results after CTC. Some of such important considerations as highlighted and implemented within the presented work are:

- Importance of instrumentation during the OTPA measurements.
- Measurement of the vehicular path excitations in multiple operational (but realistic, ensuring linear range of operation) loading scenarios in order to ensure the determination of all the significant eigenvalues of the vehicle.
- Inclusion of all coherent and incoherent transfer paths form the source subsystems into the body, i.e., identification of all the possible source-body interface levels, as well as acoustic leakages within the vehicle, in order to ensure an accurate prediction of the synthesized response.
- Consideration of parasitic paths into the Path-Receiver modelling.

Subsequently, the essence and possibilities of OTPA in order to gain insights into the critical propagation paths for the high frequency noise inside the vehicle's cabin was illustrated. Source ranking and path ranking was conducted for five different propulsion orders in the test vehicle, and an attempt to reveal the most dominant transfer paths in terms of their individual path contribution towards the interior noise level was made. Towards the later stages of the project, verification case studies were conducted not only to ensure the use of the estimated vehicular transmissibility matrix for response prediction with random excitation scenarios over the same path locations but also to verify the results revealed by the formulated Path-Receiver model within the Master Thesis.

The study revealed high-frequency structure-borne contributions inside the vehicle, which stands in contrast with the knowledge acquired from research over the conventional ICE vehicles over the years. However, this increment in structure-borne contributions at higher frequency is suspected to be a result of the path instrumentation approach followed within the presented research, which primarily revolved around the instrumentation of air-borne leakages across the vehicle as the air-borne reference DOFs. A near field instrumentation of the air-borne reference sensors and its comparison with the findings of the presented work can possibly highlight whether the high-frequency structure-borne dominance is the characteristic feature associated with the NVH propagation in EVs, or is a limitation of the presented Path-Receiver OTPA model towards providing a clear high-frequency distinction in structure-borne and air-borne contributions towards the interior noise inside an EV.

9
Future Scope

This chapter specifies some possible recommendations with regards to further research over utilization of OTPA for better e-NVH characterization over BEVs. As an obvious next step, the critical transfer paths highlighted over the prototype vehicle tested within this Master Thesis work can be further investigated by implementing appropriate modifications in order to either attenuate or mitigate the noise and vibration propagation across them. This shall incorporate dampening, stiffening or mass loading for structure-borne transfer, and blockages for the air-borne leakages. Prior to the actual verification measurements, Response Modification Analysis (RMA) can be conducted over the OTPA-estimated vehicular transmissibility matrix in order to define the sensitivity of each of the highlighted critical transfer paths towards the physical modifications [28] [29].

Another scope of exploration can be the correlation of the test-estimated (OTPA-based) transmissibilty matrix with the transfer functions estimated within Computer-Aided Engineering (CAE) domain. Upon achievement of a good correlation in CAE, further simulations for individual part-based modifications over the critical transfer paths can be performed in order to ensure interior noise refinement in a much more time-efficient and cost-efficient manner.

Because of the inherently enhanced directive nature of high frequency noise, detailed investigations over better localization of high frequency propagation across the multi-linked assembly paths can also be conducted. For instance, each of the electric motor mount on the subframe or the cradle consists of more than one bolted connections, and high frequency transfer across each of such bolted connections can be unique. Hence, the propagation of high frequency vibration across each of the bolted connection can be individually quantified by means of either operational vibration transmissibility measurements or FRF measurements. A decision can then be made to install the reference sensor (accelerometer) across the most dominant bolted connection (with maximum transmissibility), or to consider the isolation characteristics over multi-link assemblies.

Bibliography

[1] A. Diez-Ibarbia, M. Battarra, J. Palenzuela, G. Cervantes, S. Walsh, M. D. la Cruz, and S. Theodossiades, *Comparison between transfer path analysis methods on an electric vehicle*. Journal of Applied Acoustics, 2016.

[2] Siemens. An introduction to transfer path analysis. [Online]. Available: https://community.sw.siemens.com/s/article/an-introduction-to-transfer-path-analysis

[3] T. Freeman, B. Thom, and S. Smith, "Noise and vibration development for adapting a conventional vehicle platform for an electric powertrain," *SAE International*, 2013.

[4] J. Scheuren and M. Lohrmann, "Transfer path analysis – experiences, expectations and perspectives," *SAE International*, no. 2014-36-0803, 2014.

[5] K. Janssens, F. Bianciardi, L. Britte, P. V. de Ponseele, and H. V. der Auweraer, "Pass-by noise engineering: a review of different transfer path analysis techniques," *Proceedings of ISMA*, 2014.

[6] S. Wang, J.-L. Jouvray, and T. Kalos, "NVH technologies and challenges on electric powertrain," *SAE Technical Paper*, no. 2018-01-1551, 2018.

[7] Siemens. What's an order? [Online]. Available: https://community.sw.siemens.com/s/article/what-s-an-order

[8] D. D. Klerk, M. Lohrmann, M. Quickert, and W. Foken, "Application of operational transfer path analysis on a classic car," *Conference Proceeding - NAG/DAGA - Rotterdam*, 2009.

[9] R. Ström, "Operational transfer path analysis of components of a high-speed train bogie," *Master Thesis*, 2014.

[10] Z. Zhang, D. Pan, W. Wu, and C. Huang, "Vibration source identification of a heavy commercial vehicle cab based on operational transfer path analysis," *Proc IMechE Part D: Journal of Automobile Engineering 2020*, vol. 234(2-3) 669–680, IMechE 2019, 2019.

[11] A. Sakamato and M. Ozaki, "Interior sound enhancement of vehicle acceleration for new model ACCORD," *Technical Paper*, vol. 19, no. 2, 2007.

[12] M. Toome, "Operational transfer path analysis: Practical considerations for selecting sensor positions," *Canadian Acoustics*, vol. 54, no. 3, 2017.

[13] C. R. Fernández, R. S. Millán-Castillo, D. D. Klerk, and E. Barten, "Qualitative brief introduction to OTPA and a tire noise application case," *XI Congreso Iberoamericano de Acústica; X Congreso Ibérico de Acústica; 49º Congreso Español de Acústica -TECNIACUSTICA'18-24 al 26 de octubre*, 2018.

[14] J. S. Bendat, “System identification from multiple input/output data,” *Journal of Sound and Vibration*, vol. 49(3), 293-308, 1976.

[15] D. deKlerk and A.Ossipov, “Operational transfer path analysis: Theory, guidelines and tire noise application,” *Mechanical Systems and Signal Processing*, vol. 24(2010)1950–1962, 2010.

[16] M. Toome, “Operational transfer path analysis: A study of source contribution predictions at low frequency,” *Master Thesis*, 2012.

[17] “Introduction to OTPA,” *White Paper*.

[18] P. Gajdatsy, K. Janssens, L. Gielen, P. Mas, and H. V. der Auweraer, “Critical assessment of operational path analysis: Effect of neglected paths,” *15th International Congress on Sound and Vibration*, 2008.

[19] G. Forsberg and T. Möller, “The noise and vibration transfer characteristics of the steering installation in a Volvo FH truck,” *Master Thesis*, 2015.

[20] S. Liu, N. Sun, Q. Yin, Y. Qi, D. Cao, and L. Zhang, “Study of new vibration suppression devices for application to EHV transmission line groundwires,” *Energy Procedia 12*, vol. ICSGCE 2011 313 – 319, 2011.

[21] Z. Zhang, S. Meng, J. Zhao, D. Yang, N. Shu, W. Rao, and R. Xia, “Measurement of vibration characteristics of power cable line under typical laying conditions,” *High Voltage Engineering*, vol. 41(4):1188-1193, 2015.

[22] I. Consulting. Omni-directional sound sources. [Online]. Available: https://www.isvr.co.uk/automotive/sound-sources.htm

[23] M.-B. V. Systeme. Pak mkii. [Online]. Available: https://www.mbbm-vas.com/en/products/data-acquisition/pak-mkii

[24] F. Nicastro, “Optimization of engine noise reduction measurement procedure,” *Master Thesis*, 2019.

[25] A. Schuhmacher, “Techniques for measuring the vibro-acoustic transfer function,” 2010.

[26] J. Putner, M. Lohrmann, and A. Kaltenhauser, “Operational transfer path analysis predicting contributions to the vehicle interior noise for different excitations from the same sound source,” *Inter.noise Conference, New York city, USA*, 2012.

[27] Siemens. Tone-to-noise ratio and prominence ratio. [Online]. Available: https://community.sw.siemens.com/s/article/tone-to-noise-ratio-and-prominence-ratio

[28] D.-I. D. Arsić and M. Pohl, “A framework for sensitivity analysis of transfer paths combining contribution analysis and response modification analysis,” *AUTOMOTIVE ACOUSTICS CONFERENCE, Zürich, Switzerland*, 2017.

[29] A. Grosso and M. Lohrmann, “Operational transfer path analysis: Interpretation and understanding of the measurement results using response modification analysis (RMA),” *AE Technical Paper*, vol. doi:10.4271/2016-01-1823, no. 2016-01-1823, 2016.

[30] Brüel and Kjær. Datasheet. [Online]. Available: https://www.bksv.com/-/media/literature/Product-Data/bp2210.ashx

[31] GRAS. Datasheet. [Online]. Available: https://www.ni.com/pdf/manuals/G.R.A.S._46AE.pdf

A
Appendix I

Sensor No.	Air-borne Transfer Path Details
1	FDU through firewall top_centre to cabin
2	FDU through firewall top_RH to cabin
3	FDU through front wheel fender_LH to cabin
4	FDU through front wheel fender_RH to cabin
5	FDU through tunnel to cabin
6	FDU through battery side panel_LH to cabin
7	FDU through battery side panel_RH to cabin
8	FDU through steering column-firewall interface to cabin
9	Reference microphone: EFAD
10	RDU through tunnel to cabin
11	RDU through rear side-rail_LH to cabin
12	RDU through rear side-rail_RH to cabin
13	RDU through battery side panel_LH to cabin
14	RDU through battery side panel_RH to cabin
15	Reference microphone: ERAD
16	Front road-dyno contact to cabin
17	Rear road-dyno contact to cabin

Table A.1: Table summarizing the instrumented air-borne leakages within the OTPA research.

Sensor No.	Response Microphone Details
18	Driver Ear Level_mic 1
19	Driver Ear Level_mic 2
20	Driver Ear Level_mic 3
21	Driver Ear Level_mic 4
22	Passenger Ear Level_mic 1
23	Passenger Ear Level_mic 2
24	Passenger Ear Level_mic 3
25	Passenger Ear Level_mic 4

Table A.2: Table summarizing the instrumented response microphone positions inside the test vehicle. Note: Passenger Ear Level (PEL) microphones were not analyzed within the scope of this Master Thesis work.

Sensor No.	Structure-borne Transfer Path Details
26	Rear subframe_front to BIW side-rail_LH
27	Rear subframe_front to BIW side-rail_RH
28	Rear subframe_rear to BIW side-rail_LH
29	Rear subframe_rear to BIW side-rail_RH
30	ERAD through rear driveshaft_LH to rear knuckle_LH
31	ERAD through rear driveshaft_RH to rear knuckle_RH
32	Rear knuckle_LH through longitudinal rod_LH to BIW
33	Rear knuckle_RH through longitudinal rod_RH to BIW
34	Rear knuckle_LH through rear strut_LH to wheel housing_LH
35	Rear knuckle_RH through rear strut_RH to wheel housing_RH
36	Reference accelerometer: ERAD
37	EFAD through cross-member to BIW side-rail_LH
38	EFAD through cross-member to BIW side-rail_RH
39	Front subframe through battery panel mount_LH to BIW
40	Front subframe through battery panel mount_RH to BIW
41	Front subframe through C-mount_LH to BIW
42	Front subframe through C-mount_RH to BIW
43	Front knuckle_LH through link arm to front subframe
44	Front knuckle_RH through link arm to front subframe
45	Front knuckle_LH through strut mount to wheel housing_LH
46	Front knuckle_RH through strut mount to wheel housing_RH
47	EFAD through front driveshaft_LH to front knuckle_LH
48	EFAD through front driveshaft_RH to front knuckle_RH
49	Reference accelerometer: EFAD
50	EFAD to front subframe through lower torque rod_LH
51	EFAD to front subframe through lower torque rod_RH
52	On firewall_centre behind IHFA
53	On firewall_RH besides cabin harness network
54	On tunnel opening_front
55	On tunnel opening_rear
56	DI_LH on passive side
57	DI_RH on passive side

Table A.3: Table summarizing the instrumented structure-borne transfer paths within the OTPA research.

Path Name	Category	AB/SB	Details
EFAD_141_AB	EFAD	AB	Front Fender_LH
EFAD_241_AB	EFAD	AB	Front Fender_RH
EFAD_154_AB	EFAD	AB	Tunnel Front
EFAD_121_AB	EFAD	AB	Battery Side Panel_LH
EFAD_221_AB	EFAD	AB	Battery Side Panel_RH
FWallCntr_AB	EFAD	AB	Firewall Centre-Top
FWallRH_AB	EFAD	AB	Firewall RH-Top
StrClm_AB	EFAD	AB	Steering Column-Firewall Interface
ERAD_351_AB	ERAD	AB	Tunnel Rear
ERAD_321_AB	ERAD	AB	Battery Side Panel_LH
ERAD_421_AB	ERAD	AB	Battery Side Panel_RH
ERAD_303_AB	ERAD	AB	Rear Siderail_LH
ERAD_403_AB	ERAD	AB	Rear Siderail_RH
Road_150_AB	EFAD	AB	Front Road Contact
Road_350_AB	ERAD	AB	Rear Road Contact
EFAD_921_SB	EFAD	SB	DI_LH Passive Side
EFAD_922_SB	EFAD	SB	DI_RH Passive Side
SubF_102_SB	EFAD	SB	Subframe via Battery Panel Mount_LH
SubF_202_SB	EFAD	SB	Subframe via Battery Panel Mount_RH
SubF_101_SB	EFAD	SB	Subframe via C-Mount_LH
SubF_201_SB	EFAD	SB	Subframe via C-Mount_RH
StrF_141_SB	EFAD	SB	Strut Mount_LH Front
StrF_241_SB	EFAD	SB	Strut Mount_RH Front
SubR_301_SB	ERAD	SB	Rear Subframe Mount_Front_LH
SubR_401_SB	ERAD	SB	Rear Subframe Mount_Front_RH
SubR_302_SB	ERAD	SB	Rear Subframe Mount_Rear_LH
SubR_402_SB	ERAD	SB	Rear Subframe Mount_Rear_RH
Knuc_321_SB	ERAD	SB	Longitudinal Rod_LH
Knuc_421_SB	ERAD	SB	Longitudinal Rod_RH
StrR_341_SB	ERAD	SB	Strut Mount_LH Rear
StrR_441_SB	ERAD	SB	Strut Mount_RH Rear
EFAD_154_SB	PARASITIC	SB	Tunnel Front
FWallCntr_SB	PARASITIC	SB	Firewall Centre-Top
FWallRH_SB	PARASITIC	SB	Firewall RH-Top
ERAD_351_SB	PARASITIC	SB	Tunnel Rear

Table A.4: Table summarizing the considered reference DOFs within the Path-Receiver Model B as studied in detail within the presented research work [AB = Air-borne, SB = Structure-borne].

B

Appendix II

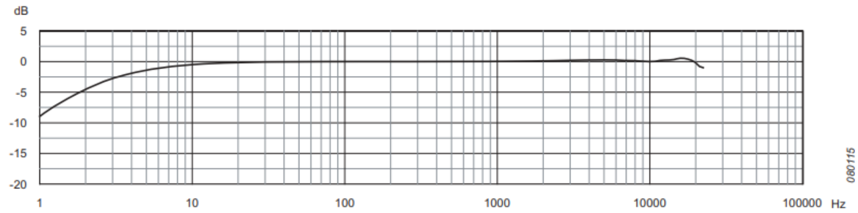

(a) B&K Type 4189 [30].

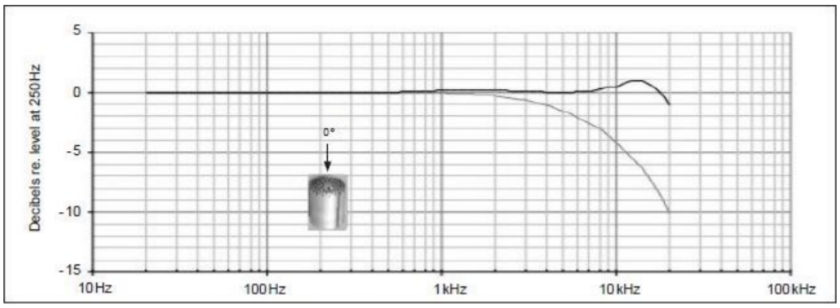

Typical frequency response. Upper curve shows free-field response for 0°, lower curve shows pressure response.

(b) GRAS TYPE 46AE [31].

Figure B.1: Frequency response function for the used microphones within the research.

DEPARTMENT OF ARCHITECTURE AND CIVIL ENGINEERING
CHALMERS UNIVERSITY OF TECHNOLOGY
Gothenburg, Sweden
www.chalmers.se

CHALMERS
UNIVERSITY OF TECHNOLOGY